

REINFORCED INTERPHASES IN PAI-MMT-NANOCOMPOSITES:

Synthesis and characterization of effects on thermal,
mechanical and dielectric properties

Dissertation zur Erlangung des akademischen Grades

Dr. rer. nat.

Eingereicht an der Fakultät für Naturwissenschaften der Universität Paderborn

von

Daniel Briesenick

Geboren am 15.06.1982 in Kempen (Niederrhein)

Erstgutachter: Prof. Dr. Wolfgang Bremser

Zweitgutachter: Prof. Dr. Hans-Joachim Warnecke

Acknowledgement

I would like to express some thoughts that come to mind when looking back at my time in Paderborn. The time I spent in the working group of Wolfgang Bremser was enriching in a variety of ways, both on a professional and a personal level. The professional and personal freedom to do whatever I felt was right was challenging but a great and unique experience. For granting this environment I would like to express my deepest gratitude to Wolfgang Bremser.

Over the years I have met many colleagues who have influenced both my personal and professional life. A very special thanks is due to Karl Hiltrop who in my view is one of the most critical thinking and honest people I have met. When I started my studies at the University of Paderborn, he was the one who believed in me. During my master thesis and the first time of my doctoral studies I was lucky to win him as mentor. I do and will miss the private and professional discussions with him.

I would like to thank all my colleagues from our working group Coating Materials and Polymers (CMP) who made up the working environment a great opportunity to develop personally and professionally. In particular, I would like to mention my former colleagues with whom I shared the office and the person who conducted a lot of the experiments. These are Alexander Kröger, Jörg Ressel, Andreas Wolk and the person who keeps the laboratory running, Gisela Jünemann-Held. Thank you so much for your critical discussions and your help which have made this thesis possible in the first place. Further, I would like to thank Anna Becker for conscientiously proof reading of this thesis.

I would like to thank my parents and my sister Melanie who unconditionally believed in me.

Finally, I want to express my deepest thanks to my girlfriend and colleague Kristina Kohlgrüber. I owe all successes at my time in Paderborn to her. Because of her, living and working in Paderborn was a joy.

I sincerely hope I did not forget anyone who would have deserved to be addressed in this chapter.

Abstract

In the present thesis, the effect of interphase modification at nanocomposites of polyamide-imide and montmorillonite on thermal, mechanical and dielectric properties was investigated. Nanocomposites describe a class of particle-filled polymer systems where at least one dimension of dispersed particles is in nanometer range. In nanocomposites of exfoliated layered silicate the sheets are present in the range of about one nanometer in thickness and several nanometers to microns in lateral dimension. This results in extraordinary large particle-polymer-surfaces. Derived from this, it can be anticipated that the dispersion of layered silicate with dimensions in the nanometer level having very large aspect ratio and stiffness in a polymer matrix can lead to a new level of performance. From basic micromechanical models it could be stated that the ratio of the composite modulus to the matrix modulus values tends to increase with the exfoliation of platelets. Accordingly, incomplete exfoliation has a very significant detrimental effect on the mechanical reinforcement efficiency.

Based on this effect the first part in this thesis dealt with the question how nanocomposites of polyamide-imide and montmorillonite with completely exfoliated states of particles can be achieved. In literature, several methods for a variety of polymer systems were widely investigated, except for polyamide-imide. With *in situ* polymerization, a novel approach towards exfoliated PAI-MMT-nanocomposites was developed and compared to the solvent casting method. The *in situ* polymerization was performed by swelling MMT intergalleries with PCP-blocked MDI and TMA monomers followed by polymerization to PAI within the intergalleries. Successful swelling due to the presence of monomers within the intergalleries and successful exfoliation was verified via XRD-measurements. Subsequent computational simulations of equilibrium geometry conducted for blocked MDI showed good correlation to enlargement of MMT's intergallery spacing which supported the thesis of successful swelling. With the novel approach of *in situ* polymerization, a new level of exfoliated particle concentration could be reached. But in comparison, the solvent casting method turned out to be simpler, faster and economically more feasible. Because of these results, subsequent preparation of nanocomposites was based on this method.

The second part of this study focused on the modification of MMT-surfaces with γ -Aminopropyltriethoxysilane (APTES) in order to provide a functional group which is able to graft MMT covalently to the polymer matrix. This group was chosen to be an amine. The target was to enable the grafting reaction via imide ring opening reaction under formation of an amide link. The success of covalent linking of interphase-modified

montmorillonite and the polymer matrix was evidenced via ^{29}Si -NMR, FTIR, XRD and DTGA-measurements.

The third part dealt with the question, how the performance of PAI is affected in terms of mechanical, thermomechanical and dielectrical properties via covalently bonded exfoliated PAI-MMT-nanocomposites. In summary it can be said that the interface-modified nanocomposite showed significant changes with a higher modulus, heat resistance, glass transition temperature and dielectric breakdown strength. Morphological investigations via FIB/SEM-analyses revealed that these effects originate from changes in the structure of the nanocomposite. By taking all results into account, a model of the resulting composite-morphology was suggested where single polymer chains are able to crosslink several montmorillonite particles.

The last part of this dissertation focused on the evaluation of the potential in applications as adhesive coating. Results showed that polyamide-imide in general exhibits properties which can be attributed to the class of high performance adhesives. Through the interface-modification and resulting reinforcement of the nanocomposite even higher performances were achieved.

1	Selected theoretical background	1
1.1	Introduction	1
1.2	Layered silicate	2
1.3	Nanocomposites of layered silicate	4
1.4	Mechanics of nanocomposites	9
1.5	Polyamide-imide	16
1.5.1	Acid chloride route	17
1.5.2	Diisocyanate route	18
1.6	Dielectrical breakdown in solid dielectrics	22
1.6.1	Intrinsic Breakdown	23
1.6.2	Electromechanical Breakdown	24
1.6.3	Breakdown due to Treeing and Tracking	25
1.6.4	Thermal Breakdown	27
1.6.5	Electrochemical Breakdown	31
1.6.6	Dielectrical breakdown of nanocomposites	31
1.7	Functional trialkoxysilanes	35
2	Concept of thesis.....	37
3	Synthesis of nanocomposites.....	41
3.1	Introduction	41
3.1.1	Exfoliation of MMT via solvent casting	43
3.1.2	Exfoliation of MMT via <i>in situ</i> polymerization	44
3.1.3	Characterization of exfoliation	44
3.2	Experimental	46
3.2.1	Reagents and materials	46
3.2.2	Synthesis of PAI	46
3.2.3	<i>In situ</i> polymerization	47
3.2.4	Synthesis of nanocomposites via solvent casting	50
3.2.5	Characterization	50
3.2.6	Visualization of MMT distribution via SEM/FIB	51
3.3	Results and discussion	53
3.3.1	Synthesis of PAI	53
3.3.2	<i>In situ</i> polymerization	56
3.3.3	Solvent Casting	60
3.4	Summary	63

4	Modification of interphases.....	65
4.1	Introduction	65
4.2	Experimental	67
4.2.1	Reagents and materials	67
4.2.2	Synthesis of PAI	67
4.2.3	Preparation of composites for determination of percolation threshold	67
4.2.4	Synthesis of silane modified MMT	68
4.2.5	Synthesis of nanocomposites	68
4.2.6	Film preparation	69
4.2.7	Characterization	69
4.3	Results and discussion	72
4.3.1	Determination of dielectric percolation threshold	72
4.3.2	Qualification of grafting	74
4.3.3	Quantification of grafting	76
4.4	Summary	80
5	Characterization of nanocomposites.....	81
5.1	Introduction	81
5.1.1	Flow induced particle alignment	81
5.1.2	Changes in properties due to nanoparticles and silane modification	84
5.2	Experimental	85
5.2.1	Film preparation	85
5.2.2	Characterization	85
5.3	Results and discussion	87
5.3.1	Dielectric breakdown strength	87
5.3.2	Thermal properties	91
5.3.3	Mechanical properties	96
5.4	Summary	99
6	Application as adhesive	100
6.1	Introduction	100
6.2	Experimental	101
6.2.1	Sample preparation	101
6.2.2	Characterization	101
6.3	Results and discussion	102
6.3.1	Method for sample preparation	102
6.3.2	Shear strength measurements	102

6.3.3	Morphology	103
6.4	Summary	106
7	Profile of key properties	107
8	Summary, conclusion and outlook.....	109
8.1	Summary	109
8.2	Conclusion and Outlook	113
9	List of publications	115
10	References	117

Chapter 1: Selected theoretical background

1.1 Introduction

Fillers play important roles in modifying the desirable properties of polymers reducing the cost of their composites. In conventional polymer composites, many inorganic fillers with dimensions in the range of microns have been used extensively to enhance the mechanical properties of polymers. Popular examples are calcium carbonate, glass beads and talc. The properties can be tailored by changing the volume fraction, shape, and size of the filler ^[1-3]. Further improvements of the mechanical properties can be achieved by using filler materials with a larger aspect ratio such as short glass fibers ^[4-6]. Derived from these results it can be anticipated that the dispersion of fillers with dimensions in the nanometer level having very large aspect ratio and stiffness in a polymer matrix could lead to even higher mechanical performances.

Nanocomposites describe a class of particle-filled polymer systems where at least one dimension of dispersed particles is in nanometer range. In nanocomposites of exfoliated layered silicate the sheets are present in range of about one nanometer in thickness and several nanometers to microns in lateral dimension. This results in extraordinary large particle-polymer-surfaces ^[7]. Two major findings have stimulated interest in nanocomposites of layered silicate. Firstly, the Toyota research group reported about a Nylon-6-montmorillonite nanocomposite ^[8]. Very small amounts of layered silicate loadings resulted in pronounced improvements of thermal and mechanical properties. Secondly,

Vaia *et al.* reported that it is possible to melt-mix polymers with layered silicates without the use of organic solvents [9].

In comparison to conventional micron-sized filled composites, nanocomposites of exfoliated layered silicate show extraordinary improvements. This includes a higher modulus [10–14], increased mechanical strength and heat resistance [15], decreased gas permeability [8,16–19] and flammability [20–22]. The main reason for improved properties in nanocomposites is related to a stronger interfacial interaction between the polymer matrix and layered silicate, compared to conventional filler-reinforced systems [23].

The behaviour of polymer–nanofiller composites is directly related to their hierarchical micro-structures. Mechanical properties of polymer–nanofiller composites are controlled by several microstructural parameters such as properties of the matrix, properties and distribution of the filler as well as interfacial bonding. Furthermore, synthesis and processing methods are important influencing factors. Interfaces are known to influence the effectiveness of load transfer from the polymer matrix to nanofillers. Thus, surface modification of nanofillers is needed to promote better dispersion of fillers and to enhance the interfacial adhesion between matrix and fillers. Fabrication of homogeneous polymer nanocomposites therefore remains a major scientific challenge for material scientists.

1.2 Layered silicate

Layered silicates belong to the class of clay minerals. They can be generally classified as phyllosilicates. The framework of layers is generated by combination of tetrahedral and octahedral sheets. A scheme is provided in Figure 1. Silica is the main component of tetrahedral sheets whilst octahedral sheet comprises elements such as Al, Mg, and Fe. Stacking of tetrahedral and octahedral layer occurs in specific ratios and modes, leading to the formation of the 2:1 layer silicates. Phyllosilicate clays with 2:1 layer structure include mica, smectite, vermiculite, and chlorite. Smectite group can be further divide into montmorillonite (MMT), nontronite, saponite and hectorite species [24,25].

Tetrahedral sheets of smectites are built of corner-linked tetrahedron with central ions of Si^{4+} or Al^{3+} and sometimes Fe^{3+} . Here, the basal oxygen of a tetrahedron is shared by neighbouring tetrahedrons, forming hexagonal patterns. Octahedral alumina sheets are located between two tetrahedral silica sheets resulting in a sandwich-like structure. The Crystal lattice of 2:1 phyllosilicate exhibits layers of about 1 nm in thickness. The stacking of the platelets leads to van der Waals gaps, also referred to as platelets intergallery. The layer charge can easily be generated by replacement of cations in the

alumina sheet with counter ions of different charges ^[26]. Replacement of Al^{3+} by Mg^{2+} or Fe^{2+} results in negatively charged layers. This negative charge is counter balanced by alkali cations (Na^+ , Li^+ or Ca^{2+}) positioned in the gallery between the aluminosilicate layers. The gallery height of pristine clay is determined by the type of cations positioned in the gallery and the degree of hydration. Generally, the Na-MMT clay is hydrophilic and expands its interlayer spaces readily when immersed in water.

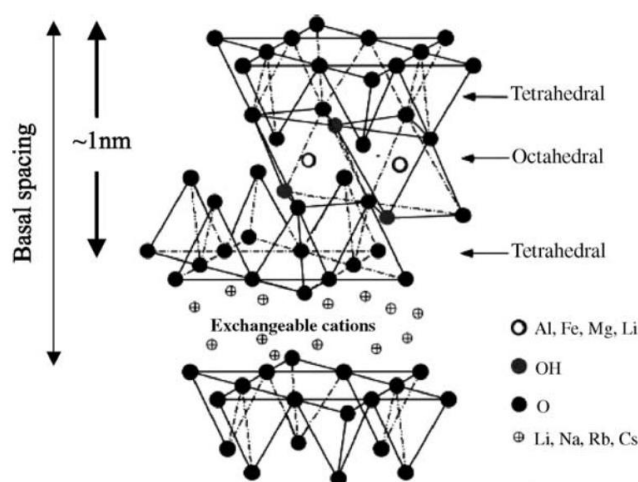


Figure 1: General crystal structure of 2:1 phyllosilicates containing sheets of tetrahedral and octahedral silicate units ^[7].

The dispersion of Na-MMT into most of polymers is rather poor due to their incompatibility with polymers and its large surface-to-volume ratio. Therefore, organic surfactant and compatibilizer additions are needed in order to improve the dispersion of these nanofillers in polymeric matrices. To convert the clay surface from hydrophilic to organophilic, cation exchange of Na^+ with e.g. alkylammonium ions has to be performed. These ions include primary, secondary, tertiary and quaternary alkylammonium cations ^[27]. The obtained product is known as “organoclay”. In this context, organoclays can be readily delaminated into nanoscale platelets by the polymer molecules, leading to the formation of polymer–clay nanocomposites. These nanocomposites belong to an emerging class of organic–inorganic hybrid materials. In comparison to conventional microcomposites they exhibit improved mechanical properties at very low loading levels ^[7,11,28–31]. When hydrated cations are ion-exchanged with organic cations such as bulky alkyl ammonium, it generally results in a larger interlayer spacing. In order to characterize the degree of isomorphous substitution, the cation exchange capacity (CEC), expressed as mequiv/100 g clay, is used. Typical CEC values of 2:1 phyllosilicates are listed in following Table 1.

Table 1: Chemical formula and cation exchange capacities of 2:1 phyllosilicates. M represents the exchangeable cation and x is the layer charge ^[32].

Silicate	Formula	CEC [mequiv/100 g]
Montmorillonite	$M_x(Al_{4-x}Mg_x)Si_8O_{20}(OH)_4$	92.6 - 120
Hectorite	$M_x(Mg_{6-x}Li_x)Si_8O_{20}(OH)_4$	120
Saponite	$M_xMg_6(Si_{8-x}Al_x)Si_8O_{20}(OH)_4$	86.6
Vermiculite	$(Mg, Fe, Al)_3 [(Al, Si)_4O_{10}] (OH)_2M_x.nH_2O$	150

In terms of reinforcement among these layered silicates, MMT is particularly attractive for polymer-clay-composites. It is environmentally friendly, readily available in large quantities at relatively low cost and its intercalation chemistry is well understood ^[33]. When a hydrophobic polymer matrix is involved, the conversion of hydrophilic inorganic clay to a hydrophobic organoclay also improves the interfacial adhesion properties between the organic and inorganic phases. The potential applications of organoclay as an effective reinforcement for polymers are under intensive research.

1.3 Nanocomposites of layered silicate

In general, layered silicates have layer thicknesses in the order of about 1 nm and a very high aspect ratio typically between 20 and 1000. In case of properly dispersed layered silicate throughout the polymer matrix, a few weight percent thus create much higher surface area for polymer-filler interaction in comparison to conventional composites.

Depending on the strength of interfacial interactions between the polymer matrix and layered silicate (modified or not), the composites can be classified in three different types of nanocomposites, which are thermodynamically achievable:

- a) aggregated (nano)composites
- b) intercalated nanocomposites
- c) exfoliated nanocomposites

Figure 2 provides a scheme of different composite structures. In aggregated composites, sheets of layered silicate are present in originally stacked structure. This can be caused by reassembly of intercalated or exfoliated structures due to hydroxylated edge-edge

interaction of the silicate layers or could be related to incompatibility between polymer matrix and clay.

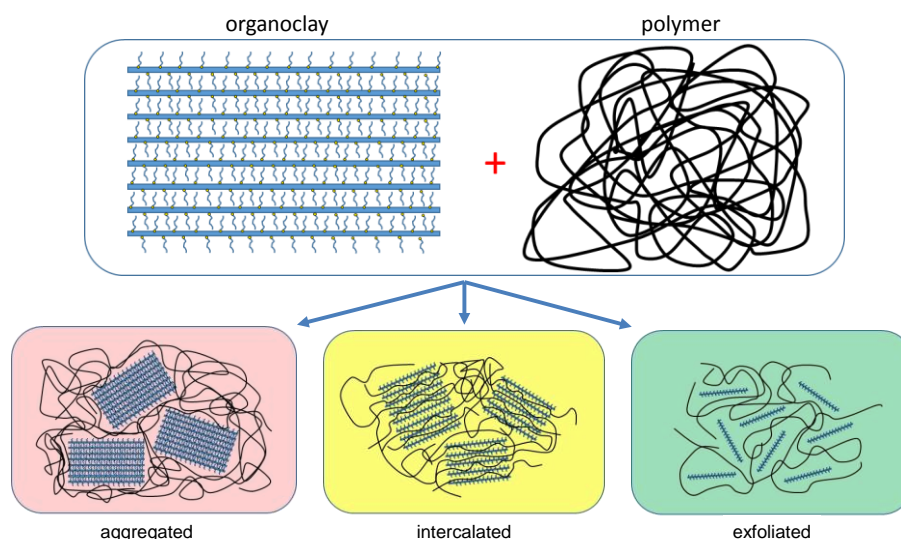


Figure 2: Scheme of three different types of thermodynamically achievable polymer/layered silicate nanocomposites.

Intercalated structures are self-assembled and well-ordered multi-layered structures in which extended polymer chains are inserted in a crystallographically regular fashion into the gallery space of the clays. This leads to an expansion of the interlayer spacing. Intercalated nanocomposites normally exhibit a few molecular layers of polymer. Properties of such composites typically resemble those of ceramic materials.

In an exfoliated structure, individual silicate sheets lose their layered geometry due to delamination. Individual clay layers are separated in a continuous polymer matrix by an average distance that depends on clay loading ^[23]. However, fully exfoliated structure is rarely seen in practice. An exfoliated structure as shown in Figure 2 is an idealized reference morphology that arises from only looking at local scale. Usually, the clay content of an exfoliated nanocomposite is much lower than that of an intercalated nanocomposite. In reality, the morphology is very often a mixed intercalated/exfoliated structure.

X-ray diffraction (XRD) is commonly used for the characterization of the structure of nanocomposites. As it is shown in Figure 3, indication for an intercalated structure is given when the peak of characteristic (001)-reflection shifts to lower angle regime due to the expansion of the basal spacing. Although the layer spacing increases, there still exists an attractive force between the silicate layers to stack them in an ordered structure.

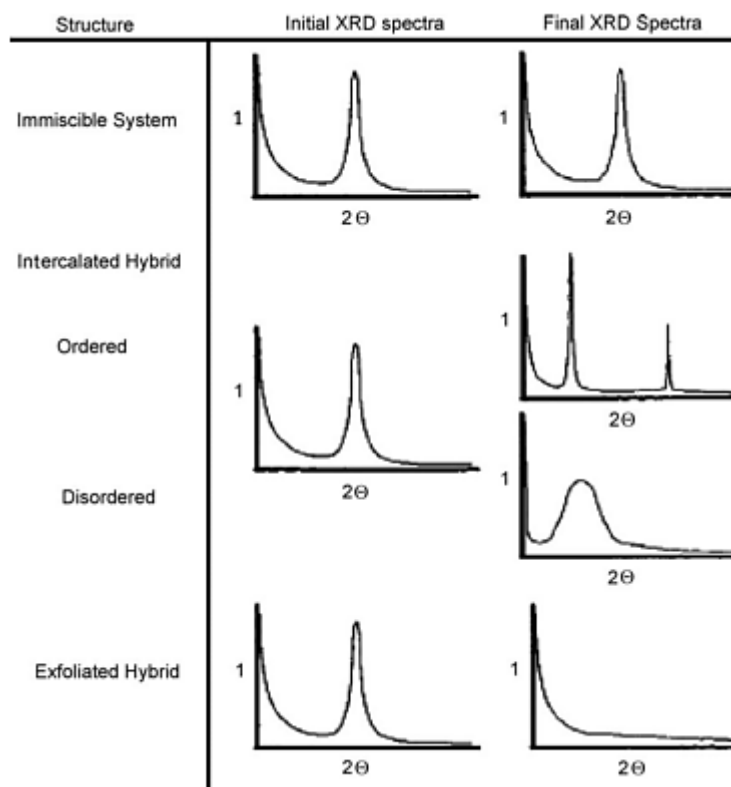


Figure 3: Schematic illustration of expected XRD patterns for immiscible, intercalated and exfoliated composites ^[34].

In contrast, no peaks are observed at XRD-pattern of exfoliated polymer nanocomposites which is due to loss of the structural registry of the layers. The absence of Bragg-diffraction peaks in the nanocomposites may indicate that the clay has been completely exfoliated or delaminated. But it should not be used as the sole evidence for the formation of an exfoliated structure ^[34]. *Morgan and Gilman* ^[35] and *Eckel et al.* ^[36] pointed out that XRD-analysis alone can lead to false interpretations of the extent of exfoliation. Several factors such as clay dilution, peak broadening and preferred orientation make XRD characterization of polymer nanocomposites susceptible to errors. Clay dilution and peak broadening can lead to the conclusion that exfoliation has occurred. Conversely, preferred orientation effects can result in the conclusion that exfoliation has not occurred. Further transmission electron microscopic observation (TEM) is needed to confirm formation of exfoliated nanocomposites ^[36].

XRD does not yield the information relating to the spatial distribution of the silicate in the polymer matrix because all its data are averaged over the whole regions of the specimen. On the other hand, TEM can provide useful information in a localized area on the morphology, structure and spatial distribution of the dispersed phase of nanocomposites. *Vaia et al.* indicated that the features of the local microstructures from

TEM give useful detail to the overall picture that can be drawn from the XRD results ^[37]. Thus, XRD and TEM techniques are regarded as complementary to each other for material characterization of the clay–polymer nanocomposites. As an example, Figure 4 shows a typical XRD pattern of a MMT-polymer-nanocomposite and corresponding TEM analyses.

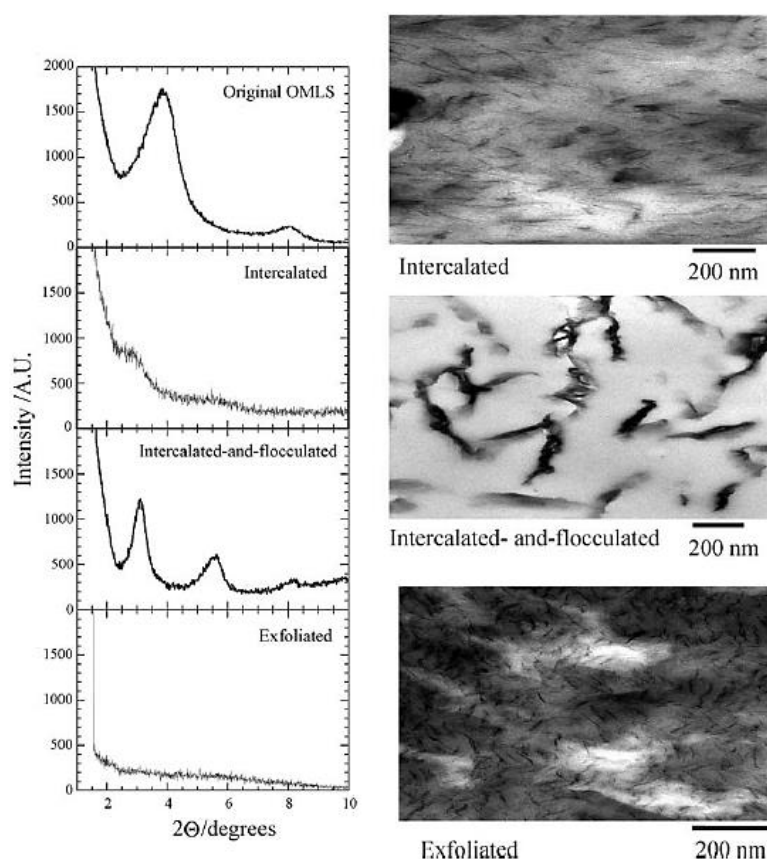


Figure 4: XRD patterns (a) and corresponding TEM images (b) of solely organoclay in comparison to different types of nanocomposites of same organoclay including intercalated and exfoliated states ^[23].

Table 2 summarizes the changes in material properties due to nanostructuration in polymer nanocomposites of exfoliated layered silicates. It provides key properties in the field of mechanical, thermal, functional and other properties and how they are affected through exfoliated layered silicate.

CHAPTER 1: Selected theoretical background

Table 2: *Changes in material properties due to nanostructuration via exfoliated layered silicate* ^[38].

Properties	Changes in properties due to nanostructuration
1 Mechanical Properties 1.1 Tensile Strength 1.2 Elongation 1.3 Bending Strength 1.4 Elastic Modulus 1.5 Impact Strength 1.6 Tribology 1.7 Creep & Fatigue	Improved (1.5 to 3 times) Much decreased (down to almost less than 10 % Improved (1.5 to 3 times) Improved (2 to 4 times) Not distinct (Slightly decreased in most castes 0.7 to 1.3 times) Improved Improved
2 Thermal Properties 2.1 Weight Deflection Temp. 2.2 Melting Point 2.3 Heat Decomposition Temp. 2.4 Expansion Coefficient	Improved (80 to 90 °C for crystalline polymers and 20 to 30 °C for amorphous polymers) Almost unchanged Improved Decreased (down to ½)
3 Functional Properties 3.1 Barrier Performance (Impermeability to vapour, oxygen gas and the like) 3.2 Flame Retardancy 3.3 Biodegradability 3.4 Foaming Property 3.5 Paint Performance 3.6 Other functional properties	Improved (2 to 10 times) Improved (Especially heat generation rate much decreased) Not distinct (Accelerated in some cases) Fine foam makes foamed materials strengthened Various reports on pigment colouring ability, ion exchange performance Electric and magnetic properties, touch sensors, heat cut performance
4 Other Properties 4.1 Weathering Resistance 4.2 Resistance to chemicals 4.3 Transparency 4.4 Water Absorption 4.5 Size Stability 4.6 Specific Gravity	Not distinct Unchanged Unchanged, Improved in some crystalline polymers Improved Improved Almost unchanged

1.4 Mechanics of nanocomposites

The use of rigid inorganic fillers, e.g. silica particles, as toughening agent is well recognized [2,39–44]. *Kim* and *Michler* studied the deformation behavior of the polymers filled with elastomers or rigid particles [39,40]. Based on the results of *Kim et al.*, *Gayman* and co-workers summarized the toughening process of rigid particles into three stages [41]:

- I) Stress concentration: Rigid particles act as stress concentrators because they have different elastic properties compared to the matrix polymer.
- II) Debonding: Stress concentration gives rise to build up of triaxial stress around the particles. This leads to debonding at particle–polymer interfaces.
- III) Shear yielding: The voids resulting from debonding alter the stress state of the polymer matrix surrounding the voids. This reduces the susceptibility towards further crazing and promotes shear yielding.

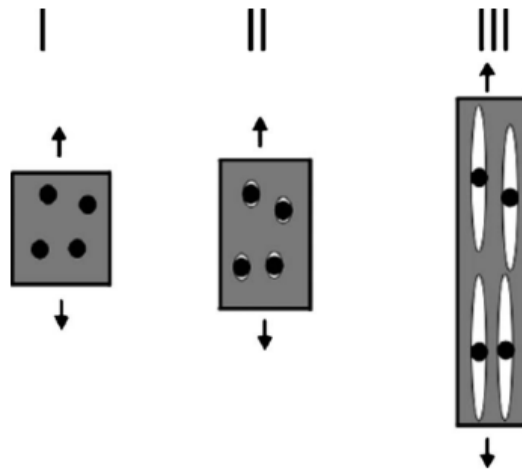


Figure 5: Scheme of toughening mechanism of a polymer matrix with rigid particles [41].

The toughening mechanism with rigid particles is schematically shown in Figure 5. In order for rigid particles to act as effective toughening agents, they must fulfil certain requirements [41]. These include particle sizes with less than 5 μm , otherwise the created voids would act as crack initiation sites. The aspect ratio of particles must be close to unity to avoid high stress concentrations. The particles should be dispersed well and homogeneously distributed in the polymer matrix. Particles must debond prior to the yield strain of the matrix polymer.

From volume strain measurements on PP–CaCO₃ composites, *Lazzeri et al.* indicated that debonding of rigid particles from the matrix prior to macroscopic yielding triggers dilatational process of the composites. This is similar to reports about rubber-toughened polymers ^[43].

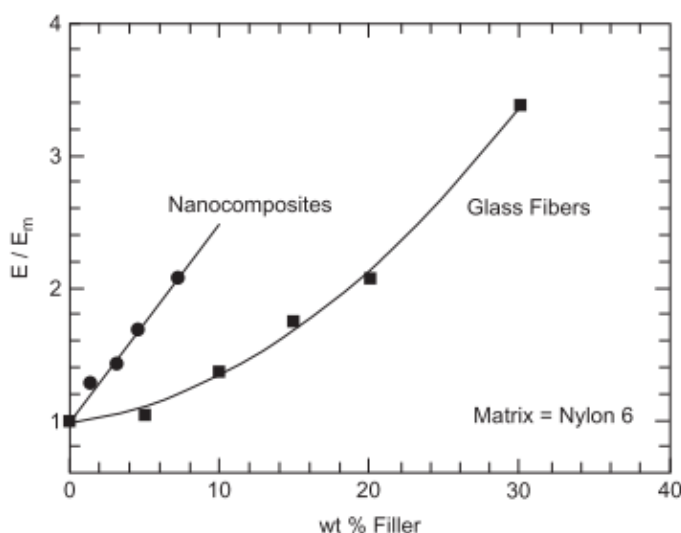


Figure 6: Comparison of reinforcement of nanocomposites based on Nylon 6 as polymer matrix and organically modified montmorillonite as nanofiller ^[45].

As opposed to conventional filled composites, nanocomposites made of a polymer and clay (modified or unmodified) frequently exhibit improved mechanical and material properties. It is supposed, that the interaction between clay and matrix at nanoscale level is the basis for obtaining new and novel properties of these nanocomposites. For example, the results provided in Figure 6 have shown that the modulus of Nylon-6 was increased much more rapidly by the addition of organically modified clay than through the addition of glass ^[45]. It further could be shown, that doubling the modulus requires approximately 6.5 wt-% of MMT whereas three times of this amount of glass fibers are required to achieve the same increase. This advantage has significant implications. Lower filler levels translate into lighter components, which is a desirable feature in many applications, e.g. in transportation where fuel efficiency is important. In addition, smaller sacrifices in matrix properties, such as ductility, impact strength, and surface finish, are often experienced with such nanocomposites.

Zeng et al. reported, that pristine or organically modified clay platelets incorporated to polymer matrix can change the mechanical properties in several ways ^[46]. First, a clay platelet itself can impart additional toughness and strength through its own mechanical properties. Second, a clay platelet can inhibit failure by blocking the propagation of cracks. Third, the structural changes of a macromolecular chain near the clay surface alter

the mechanical properties. In case of polymer nanocomposites of layered silicate, it is well accepted that the improvement in mechanical properties is directly related to the degree of dispersion of silicate layers in the nanocomposite and also the interfacial interaction between the clay surface and the polymer matrix. However, there has been considerable interest in theory and simulations addressing the preparation and properties of these materials [34,37,47–58].

To explain the mechanical properties of polymer nanocomposites like stiffness and strength, important issues arise that concern whether the classical composite mechanics theories of reinforcement can be applied or not. The most important micromechanical models are the Halpin-Tsai and Mori-Tanaka models. *Halpin* and *Tsai* developed a commonly used composite theory for predicting the stiffness of unidirectional composites as a function of the filler aspect ratio [59,60]. Their theory is based on the original micromechanical theories of *Hermans* [61] and *Hill* [62]. *Hermans* generalized the self-consistent theory of *Hill* by considering a single fiber encased in a cylindrical shell of the matrix embedded in an infinite medium that is assumed to possess the average properties of the composite [63]. *Halpin* and *Tsai* reduced the results of *Herman* into a simpler analytical form that is adapted for a variety of reinforcement geometries. This includes the reinforcement by usage of discontinuous filler. According to *Halpin* and *Tsai*, the overall elastic modulus of the composites E_c can be described as

$$\frac{E_c}{E_m} = \frac{1 + \xi \eta \phi_f}{1 - \eta \phi_f} \quad (1)$$

where E_m is the matrix tensile modulus and ϕ_f is the volume fraction of the fiber reinforcement. The constant ξ can be defined as

$$\xi = f \left(\frac{l}{d} \right) \quad (2)$$

where l/d (length/diameter) is the aspect ratio of the reinforcing fibers and η is

$$\eta = \frac{\frac{E_f}{E_m} - 1}{\frac{E_f}{E_m} + \xi} \quad (3)$$

where E_f represents the Young's modulus of the filler.

The Mori–Tanaka mean field theory is used to assess the overall properties such as the effective stiffness tensor C^* of the composites. It is based on the Eshelby method ^[64] for estimating stress state in composite reinforced with misfitting inclusions. The composite is assumed to be composed of a continuous matrix and discrete inclusions of different stiffness. The effective stiffness tensor C^* is given by the following relation ^[65,66]

$$C^* = C_I + V_2 \{ (C_2 - C_I) A \} \quad (4)$$

where C_I is the matrix phase stiffness tensor, C_2 the inclusion stiffness tensor, V_2 the inclusion volume ratio, and A is the concentration tensor. For a composite consisting of a single, arbitrarily shaped inclusion perfectly bonded inside the matrix, the dilute strain concentration tensor of the effective particle is given by

$$A^{(dil)} = [I + SC^{-1}(C_2 - C_I)]^{-1} \quad (5)$$

where I is the fourth order unit tensor and S the fourth order Eshelby tensor. As the inclusion volume fraction increases, interaction between the inclusions reduces the accuracy of the dilute approximation. In other words, interactions of the field from other inclusions are expected to influence the evolution of the average fields in the matrix and the reinforcement. The Mori–Tanaka approach includes the effect of particle interaction ^[65]. In this case, A can be expressed as

$$A = A^{(dil)} [V_1 I + V_2 \{ A^{(dil)} \}]^{-1} \quad (6)$$

where V_1 is the matrix volume ratio. The Mori–Tanaka model has better predictive capability for fillers with relatively high aspect ratios. The theory of *Tandon* and *Weng* is based on the Mori–Tanaka approach and derived the longitudinal modulus (E_{11}) of the composite reinforced with platelets ^[67]:

$$\frac{E_{11}}{E_m} = \frac{I}{1 + \phi_f \frac{-2\nu_m A_3 + (I - \nu_m) A_4 + (I + \nu_m) A_5 A}{2A}} \quad (7)$$

where ν_m is the Poisson's ratio of the matrix and ϕ_f the volume fraction of the filler. A_3 , A_4 and A_5 are calculated from the matrix and filler properties and the components of the Elshelby tensor.

For both approaches of Halpin–Tsai equations and Mori–Tanaka theory a number of assumptions are inherent: Filler and matrix are linearly elastic, isotropic, and firmly bonded. The filler is perfectly aligned, asymmetric, and uniform in shape and size. Particle–particle interactions are not explicitly considered. For all composite theories, the properties of the matrix and filler are considered to be identical to those of the pure components.

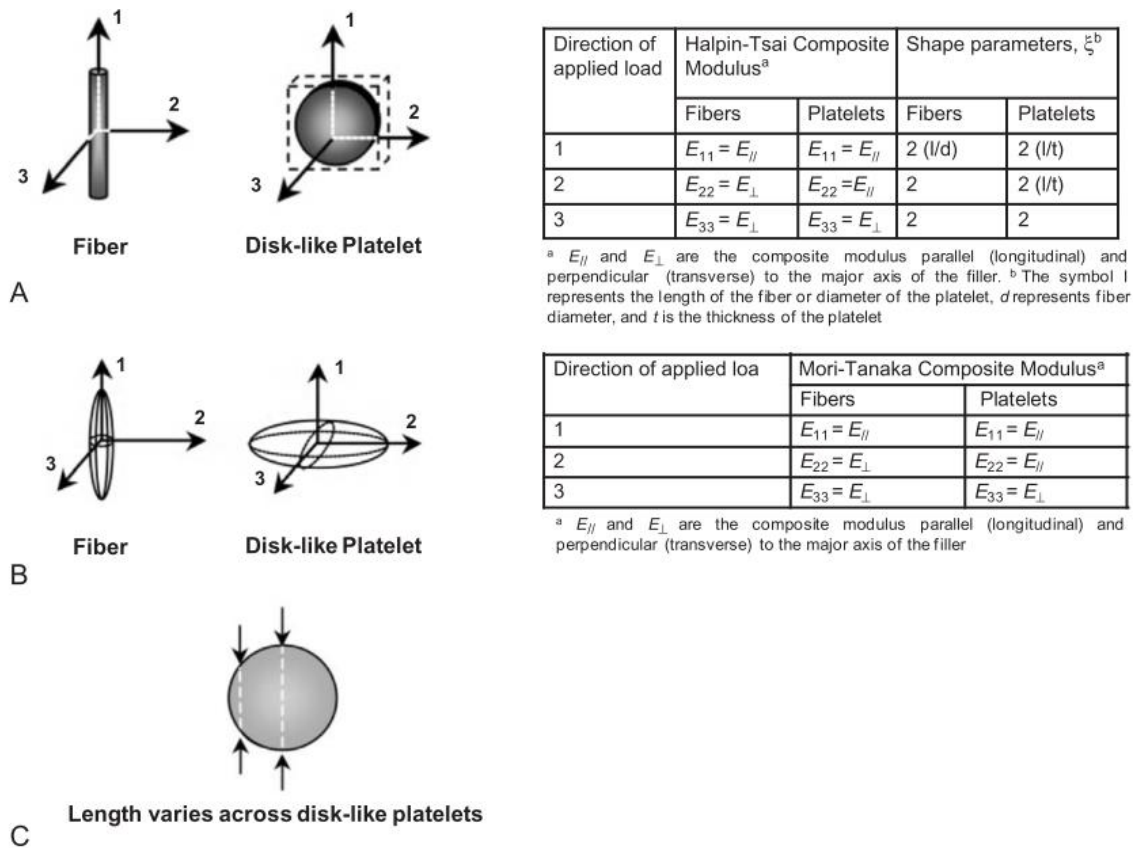


Figure 7: Physical representations of corresponding (a) Halpin-Tsai, (b) Mori-Tanaka equations used for calculation of composite's stiffness based on fiber and disk-like platelet reinforcement. (c) shows the inherent variation in length and subsequent aspect ratio across a disk-like platelet ^[45].

In addition to these assumptions, a number of differences between the two theories are worth noting. They are shown in Figure 7. First, the Mori–Tanaka theory treats fibers and disks as ellipsoidal particles. In contrast, the Halpin–Tsai equations treat a fiber as a fiber and disk as a rectangular platelet. Further, the latter disparity in the Halpin–Tsai equations is of some concern because the length and aspect ratio across a disk are not constant ^[45].

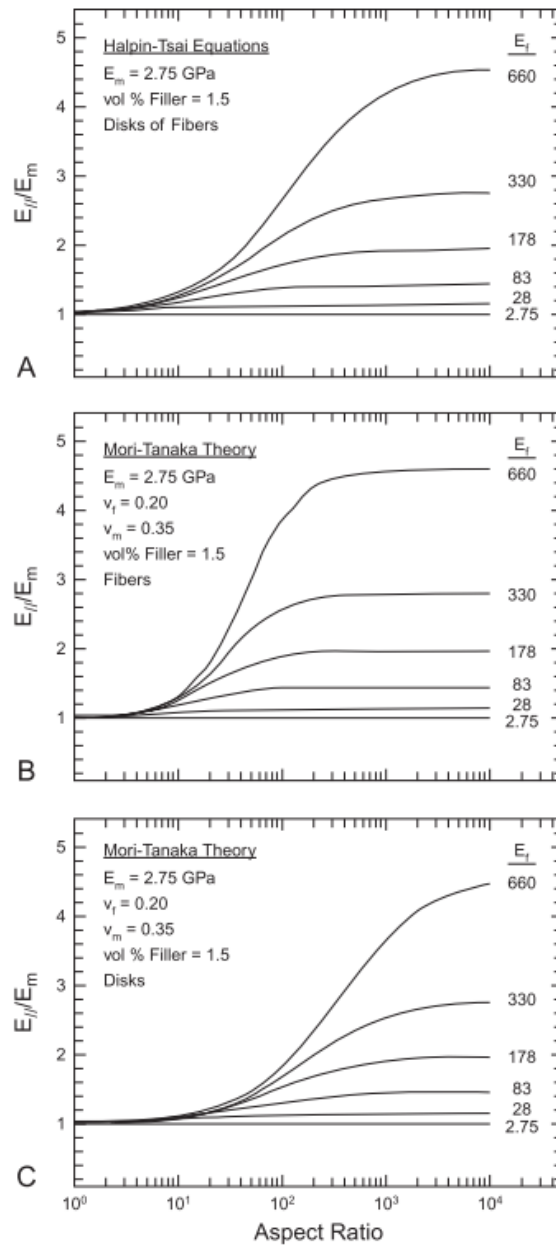


Figure 8: Effect of filler aspect ratio and modulus on the longitudinal reinforcement of composites based on fiber and disk-like fillers. The plots are determined by (a) Halpin-Tsai for fibers and disks and Mori-Tanaka theory for (b) fiber and (c) disk reinforcement [45].

Second, the Halpin–Tsai equations for E_{11} and E_{22} are independent of the Poisson’s ratio of the filler or the matrix. Third, the Halpin– Tsai equations for modulus, which is perpendicular to the filler’s major axis, are independent of the aspect ratio.

Figure 8 provides a more comprehensive examination on how the two theories respond to the filler geometry, aspect ratio, and modulus. On this occasion, it shows the modulus

predictions of Halpin–Tsai equations, which provides the same E_{11} for both, disk and fiber reinforcements. Increasing the aspect ratio results in higher reinforcement for a given filler modulus and concentration. Likewise, increasing the filler modulus also improves the reinforcement, especially for aspect ratios greater than 20–30. Molecular dynamics simulations by *Manevitch* and *Rutledge* ^[45,68] pointed out that the modulus of a single aluminosilicate sheet is significantly greater than the experimentally reported value of 178 for MMT. This would result in an even more pronounced effect on nanocomposite stiffness as demonstrated in Figure 8 (a). Analogous predictions of Mori–Tanaka theory for fibers and disks are given in Figure 8 (b) and (c). In comparison to Figure 8 (a), trends are qualitatively the same but differ quantitatively. The Mori–Tanaka theory predicts that the fiber reinforcement has a stronger dependence on the aspect ratio at a given filler modulus than by the Halpin–Tsai model. Here, lower reinforcement at low aspect ratios from disks than the Halpin–Tsai equations are observed. However, each theory does asymptote to the same values for very high filler aspect ratios. Overall, considerable potential for improvement in stiffness of nanocomposite by improvements in platelet exfoliation and synthesis of high aspect ratio clays can be assumed.

To describe micromechanics of layered particles in polymer–clay nanocomposites, parameters associated with hierarchical morphology of the clay should be incorporated. These include silicate interlayer spacing (d_{001}), gallery spacing and platelet thickness. Therefore, *Brune* and *Bicerano* ^[69] developed a micromechanical model for the prediction of the effects of incomplete exfoliation on the tensile modulus of polymer–clay nanocomposites. They treated the incomplete exfoliated system as composite consisting of a matrix and pseudo particles which are incompletely exfoliated. Thus, they modified the Halpin–Tsai equation for tensile modulus of intercalated (or incompletely exfoliated) nanocomposites. When there is only one platelet in a stack, indicating completely exfoliated nanocomposites, the model of *Brune* and *Bicerano* is reverting back to Halpin–Tsai equation.

Concluding, it can be stated that the ratio of the composite modulus to the matrix modulus values tends to increase with exfoliation of platelets. Less platelets are incorporated into the stack. Accordingly, incomplete exfoliation has a very significant detrimental effect on the reinforcement efficiency ^[67].

1.5 Polyamide-imide

The polymer matrix chosen for this study is polyamide-imide (PAI) which is known for its outstanding thermal performance, chemical and abrasion resistance and low coefficient of friction ^[70]. Figure 9 illustrates the repeating unit containing characteristic amide and imide groups of PAI.

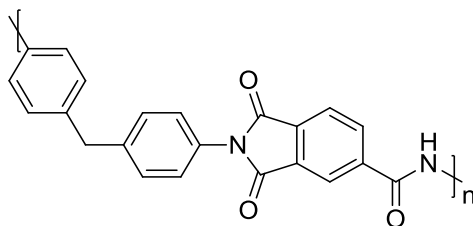


Figure 9: Repeating unit of Polyamide-imide.

PAI merges both, greater mechanical properties typically linked with polyamide and the high thermal stability and solvent resistance derived from polyimide. These properties enables PAI's general use as insulation coatings for e.g. magnet wires, foils and circuit boards. Previous work has shown that self-lubricating properties of PAI can further be improved by nanostructuring of coating surfaces with “tethered liquid” like domains ^[71]. It was realized by block-copolymer-synthesis of polyamide-imide and polydimethylsiloxane resulting in phase separations which led to specific covalently bonded PAI-PDMS-nanostructures.

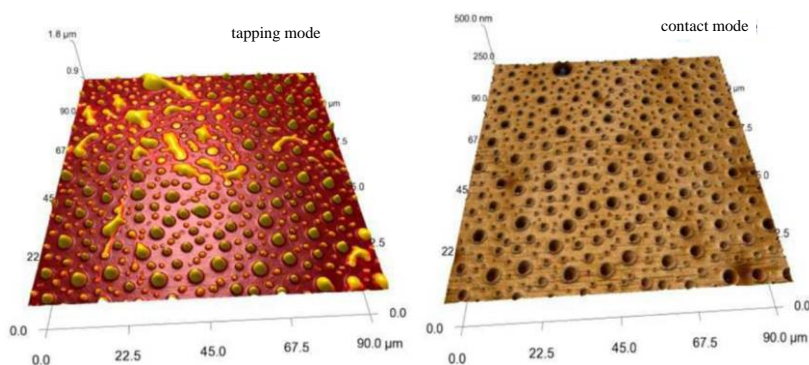


Figure 10: AFM images of micro structured PAI-PDMS coating. Left image was captured in tapping mode and right image in contact mode indicating liquid-like behaviour of phase micro patterns.

Figure 10 exemplary shows respective AFM-analyses. The image on the left side was captured in tapping mode and patterns of PDMS domains are visible. The image on the right side was captured via contact mode. In contrast to the left image, PDMS domains are visible due to higher applied force visible as crater indicating a liquid-like behaviour.

Depending on PDMS-segment length, resulting coatings exhibited significantly decreased coefficients of friction ^[71].

Polyamide-imide can be obtained from several strategies of synthesis. The commercial routes are the acid chloride and the diisocyanate route.

1.5.1 Acid chloride route

The stoichiometric reaction between trimellitic acid chloride and an aromatic diamine, e.g. methylene diphenylamine (MDA), yields poly(amideamic acid). A general scheme of reaction is provided in Figure 11.

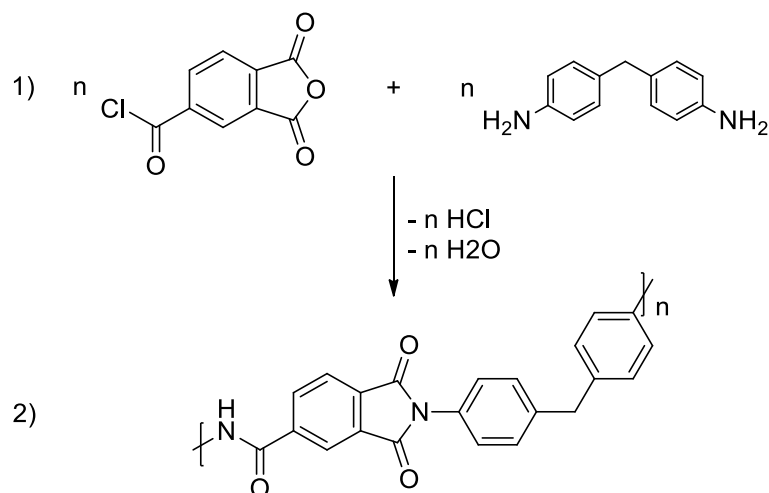


Figure 11: Simplified synthesis scheme of Polyamide-imide via acid chloride route.

Reactions are carried out at temperatures between 0-50 °C in an aprotic polar solvent such as N-methylpyrrolidone (NMP), dimethylacetamide (DMAc), or dimethylformamide (DMF). Low moisture levels are required to avoid early chain termination by hydrolysis and achieve sufficient molecular weight. These are typically in the range of 10,000-50,000 Dalton. Tertiary amines are commonly added to remove hydrogen chloride generated from the system ^[72]. The formation of imide structures is obtained either due to dehydration of the acid intermediate, addition of tertiary amines or anhydrides ^[73–75].

The acid chloride route also gives the opportunity to use this resin in an system of aqueous solvents ^[70]. Use of a base, such as dimethylethanolamine, allows water solubility without use of organic solvents such as NMP or DMF. A more detailed scheme of the synthesis is shown in following Figure 12.

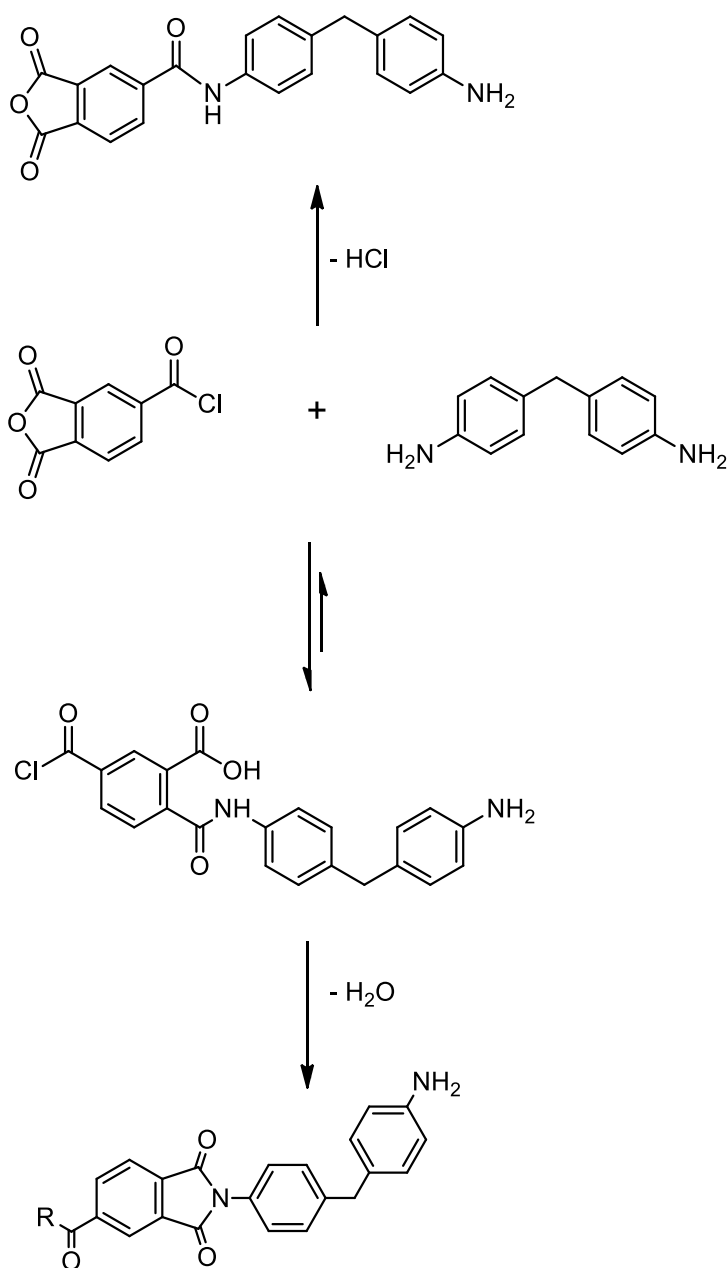


Figure 12: Reaction scheme of PAI synthesis from acid chloride route.

1.5.2 Diisocyanate route

The diisocyanate route used in this study based on the work of Hitachi Chemical Corp.^[76] and nowadays is the most common for preparation of PAI resins^[70,77,78]. On this occasion a polyisocyanate, preferably a diisocyanate, reacts under heat with 1,2,4-benzenetricarboxylic acid anhydride (TMA) in N-methyl pyrrolidone (NMP). The general reaction scheme is shown in Figure 13.

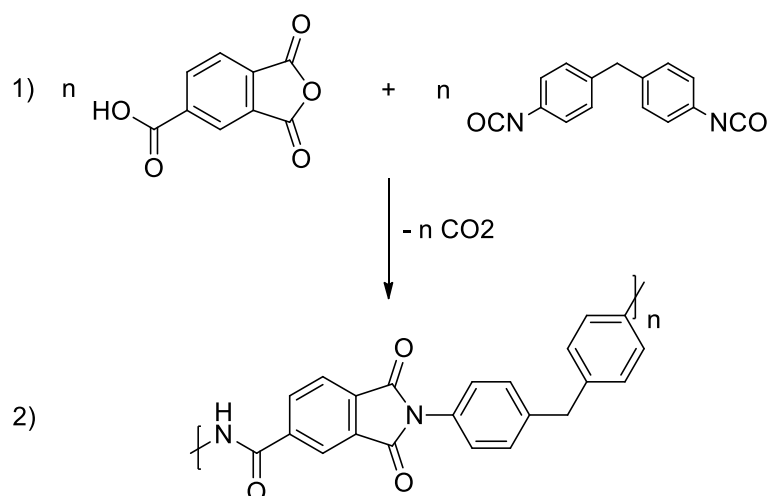


Figure 13: Synthesis scheme of Polyamide-imide via diisocyanate route.

While the mechanism for building of amide function is widely known ^[79,80], the mechanism of imide formation based on anhydrides and free isocyanates is not fully explained and understood. First suggested mechanisms assumed that reaction of anhydrides leads over a 7-membered transition state directly to imide formation ^[81,82]. Today, this is assumed to be unlikely ^[83]. Model experiments have shown that imide formation is decisively influenced by catalytic amounts of water, without whom the reaction would be slow and at low conversion rates ^[82].

A scheme of a possible mechanism is shown in Figure 14. Ring-opening of anhydrides can take place directly with water or with aromatic amines during reaction. In case of opening of anhydrides due to water, following reaction occurs with free isocyanate under formation of a mixed anhydride with adjacent carboxyl group. Decarboxylation of this mixed anhydride leads to stable amic acid. By reaction of the acid group with further isocyanate, activation of carbonyl carbon atom takes place which facilitates cyclization of neighbouring nitrogen of amide ^[76,78,84,85]. From following decarboxylation another amine can be released which can undergo further reaction with an anhydride directly to imide. Another possibility is a reaction with further isocyanate to imide under formation of an urea intermediate.

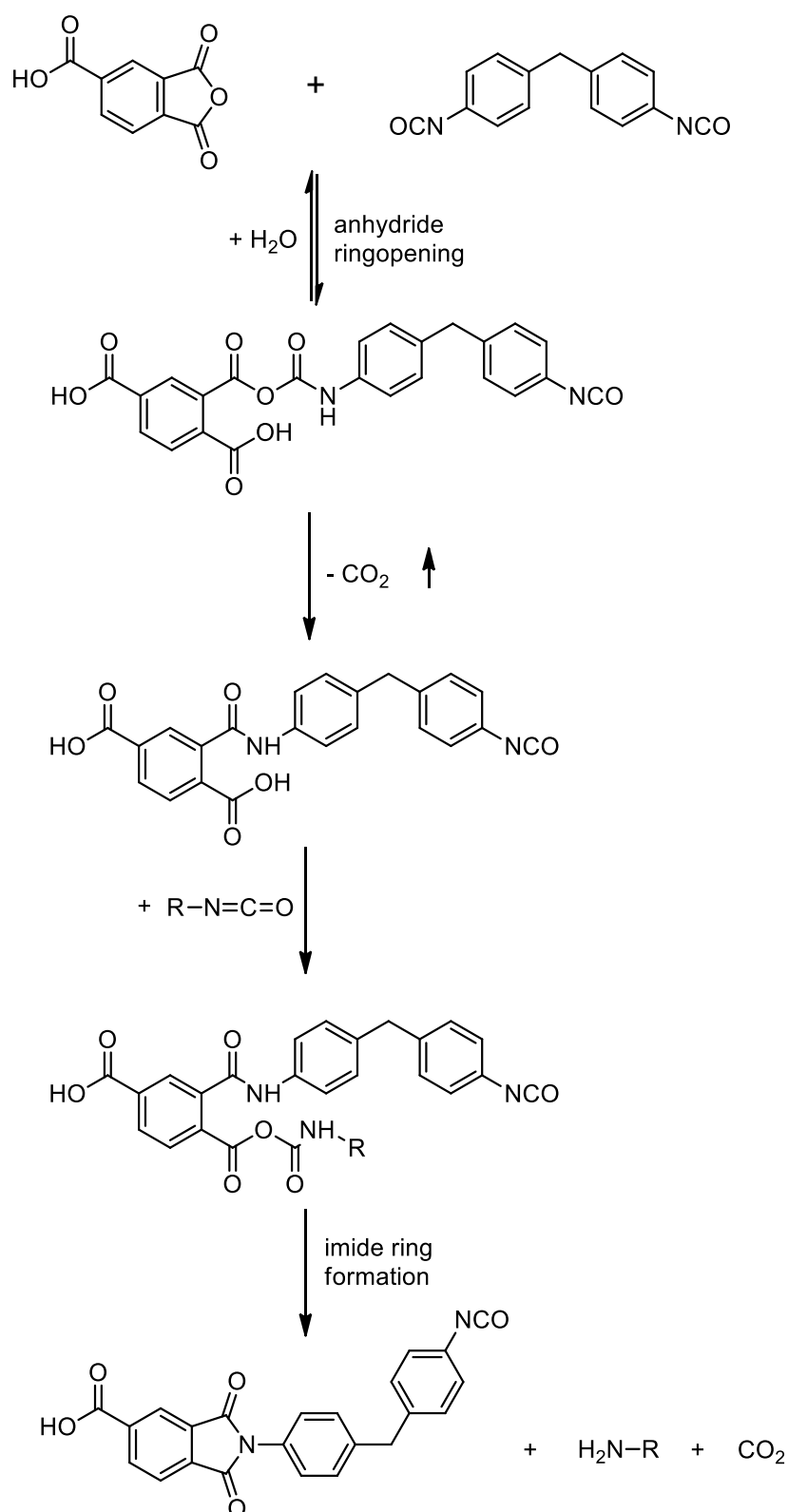


Figure 14: Reaction scheme of imide ring formation during isocyanate route of PAI synthesis.

The PAI structure obtained by diisocyanate route has been characterized extensively by NMR techniques^[86–88]. Statistical distributions of imide-imide, amide-imide, and amide-amide linkages were observed.

A reaction scheme of amide formation is shown in Figure 15. The amide structure arises from reaction of free carbon acid with respective isocyanate of diisocyanate (Figure 15.1). This leads to a N-carboxyanhydride intermediate (Figure 15.2). In the last step, carbon dioxide's characteristic amide group is formed by decarboxylation (Figure 15.3).

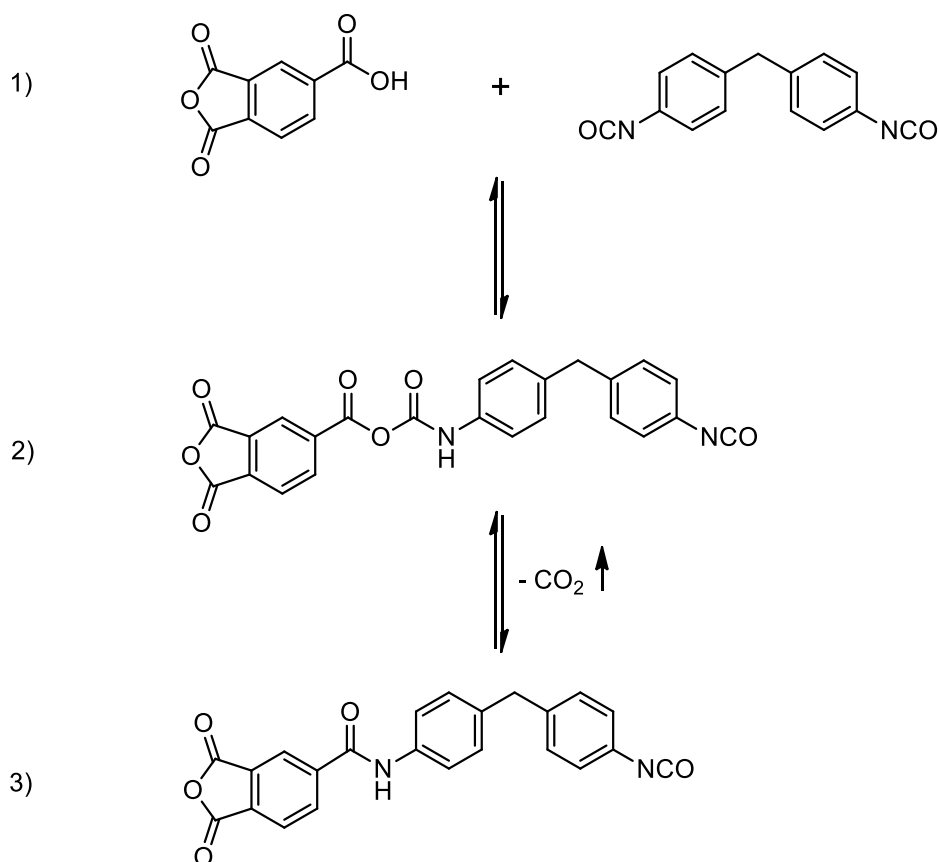


Figure 15: Formation of amide bonding via reaction of TMA and MDI in (1) over N-carboxyanhydride^[89] shown in (2) followed by decarboxylation to amide structure (3)^[89].

1.6 Dielectrical breakdown in solid dielectrics

Solid insulating materials are used almost in all electrical equipment, especially when the operating voltages are high. The solid insulation not only provides insulation to the live parts of the equipment from the grounded structures, it sometimes provides mechanical support to the equipment. The breakdown of solid dielectrics not only depends on the magnitude of voltage applied. It is a function of time for which the voltage is applied. In general, the product of the breakdown voltage and the natural logarithm of the time required for breakdown is assumed to be constant ^[90].

$$V_b = \ln t_b = \text{const.} \quad (8)$$

In case of solids, the mechanism of breakdown due to voltage is a complex phenomenon. It varies depending on the time of voltage application as shown in Figure 16.

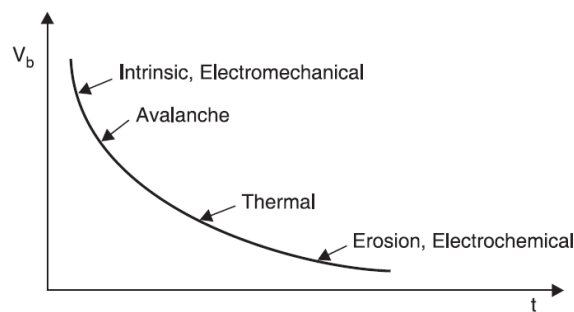


Figure 16: Function of breakdown strength versus time after application of voltage ^[90].

The dielectric strength of solid materials is affected by many factors, e.g. ambient temperature, humidity, duration of test, impurities or structural defects, the kind of applied voltage (a.c., d.c. or impulse voltages), pressure applied to these electrodes etc. The mechanism of breakdown in solids is less understood. However, the time of application plays an important role in breakdown processes. It is convenient to divide the time scale of voltage application into regions of different underlying mechanisms ^[90]:

- (a) Intrinsic Breakdown
- (b) Electromechanical Breakdown
- (c) Breakdown Due to Treeing and Tracking
- (d) Thermal Breakdown
- (e) Electrochemical Breakdown

The following chapters give a short introduction in the principles of dielectric breakdown divided by respective underlying mechanism.

1.6.1 Intrinsic Breakdown

If the dielectric material is pure and homogeneous, the temperature and environmental conditions suitably controlled and if the voltage is applied for a very short time of the order of 10^{-8} seconds, the dielectric strength of the specimen increases rapidly to an upper limit which is called intrinsic dielectric strength. The intrinsic strength therefore depends mainly upon the structural design of the material itself. Because the structure can change slightly by temperature condition it is affected by the ambient temperature. In order to obtain the intrinsic dielectric strength of a material, the samples are prepared in a way where there is high stress in the centre of the specimen and much lower stress at the corners. This is shown in Figure 17.



Figure 17: Design of specimen for intrinsic breakdown ^[90].

The intrinsic breakdown is obtained in times of the order of 10^{-8} seconds. Therefore it has been considered to be electronic in nature. The required stresses are of the order of one million volt/cm. The intrinsic strength is generally assumed to be reached when electrons in the valance band gain sufficient energy from the electric field to cross the forbidden energy gap to the conduction band. In pure and homogenous materials, the valence and the conduction bands are separated by a large energy gap at room temperature. Electrons are not able to jump from the valance band to the conduction band. Therefore, the conductivity of pure dielectrics at room temperature is zero. However, in practice no insulating material is pure. Some impurities and/or imperfections are mostly present in their structural designs. The impurity atoms can act as traps for free electrons in energy levels that lie just below the conduction band. An amorphous crystal will therefore always have some free electrons in the conduction band. As the energy gap between the trapping band and the conduction band is small, some of the trapped electrons will be excited thermally into the conduction band at room temperature. Therefore, an amorphous crystal will always have some free electrons in the conduction band. As an electric field is applied, the electrons gain energy and the energy is shared by all electrons due to collisions between them. In an amorphous dielectric the energy gained by electrons from the electric field is higher than can be transfered to the lattice. Therefore, the

temperature of electrons will exceed the lattice temperature resulting in an increase in number of trapped electrons reaching the conduction band. This finally leads to complete breakdown ^[90].

1.6.2 Electromechanical Breakdown

When a dielectric material is subjected to an electric field, charges of opposite nature are induced on the two opposite surfaces of the material. Hence, a force of attraction is developed resulting in an electrostatic compressive force. When this force exceeds the mechanical withstand strength of the material, the material collapses. If the initial thickness of the material is d_0 and is compressed under the applied voltage V to a thickness d , then the compressive stress developed due to electric field is

$$F = \frac{1}{2} \epsilon_0 \epsilon_r \frac{V^2}{d^2} \quad (9)$$

where ϵ_r is the relative permittivity of the specimen and ϵ_0 its initial length ^[90]. If γ is the Young's modulus, the mechanical compressive strength is

$$\gamma \ln \frac{d_0}{d} \quad (10)$$

Equating (9) and (10) results in

$$\frac{1}{2} \epsilon_0 \epsilon_r \frac{V^2}{d^2} = \gamma \ln \frac{d_0}{d} \quad (11)$$

or

$$V^2 = d^2 \frac{2\gamma}{\epsilon_0 \epsilon_r} \ln \frac{d_0}{d} = K d^2 \ln \frac{d_0}{d} \quad (12)$$

Differentiating with respect to d results in

$$2V \frac{dV}{dd} = K \left[2d \cdot \ln \frac{d_0}{d} - d^2 \cdot \frac{d}{d_0} \cdot \frac{d_0}{d^2} \right] = 0 \quad (13)$$

$$\text{or} \quad 2d \cdot \ln \frac{d_0}{d} = d \quad (14)$$

$$\text{or} \quad \ln \frac{d_0}{d} = \frac{1}{2} \quad (15)$$

$$\text{or} \quad \frac{d}{d_0} = 0.6 \quad (16)$$

For any real value of voltage V , the reduction in thickness of the specimen cannot be more than 40 %. If the ratio V/d at this value of V is less than the intrinsic strength of the specimen, a further increase in V shall make the thickness unstable and the specimen collapses. The highest apparent strength is therefore obtained by substituting of $d = 0.6d_0$ in the above expressions.

$$\frac{V}{d} = \sqrt{\frac{2\gamma}{\epsilon_0 \epsilon_r} \ln 1.67} \quad \text{or} \quad \frac{V}{d_0} = E_a = 0.6 \left[\frac{\gamma}{\epsilon_0 \epsilon_r} \right]^{1/2} \quad (17)$$

Above equation is only approximate as γ depends upon the mechanical stress. The possibility of instability occurring at lower average field is ignored. This means that an effect of e.g. stress concentration at irregularities is not taken into account.

1.6.3 Breakdown due to Treeing and Tracking

It is common that the strength of a chain is given by the strength of its weakest link. Similarly, whenever a solid material has some impurities in terms of some gas pockets or liquid pockets in it, dielectric strength of the solid will be more or less equal to the strength of the weakest impurities. If some gas pockets are trapped in a solid material during manufacture and the gas has a relative permittivity of unity and the solid material a permittivity of ϵ_r , the electric field in the gas will be ϵ_r times the field in the solid material. This results in breakdown of the gas at a lower voltage. The charge concentration in this void would make the field more non-uniform. The charge concentration in such voids is found to be quite large to given fields of the order of 10 MV/cm. This is even higher than the intrinsic breakdown. Charge concentrations at the voids within the dielectric lead to breakdown step by step. This finally leads to complete rupture of the dielectric material. The breakdown is not caused by a single discharge channel. Because it assumes a tree

like structure, it is known as breakdown due to treeing. A scheme of the tree-like structure is provided in following Figure 18.

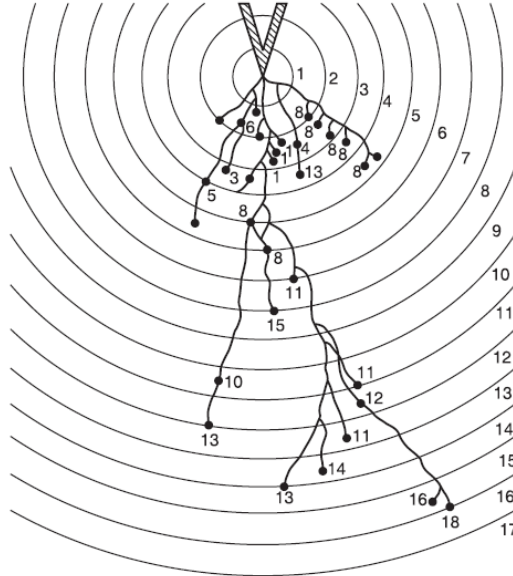


Figure 18: Scheme of local discharge channels forming a tree-like structure ^[90].

The treeing phenomenon can be readily demonstrated in a laboratory by applying an impulse voltage between point plane electrodes with the point embedded in a transparent solid dielectric like PMMA. An example is given in Figure 19.

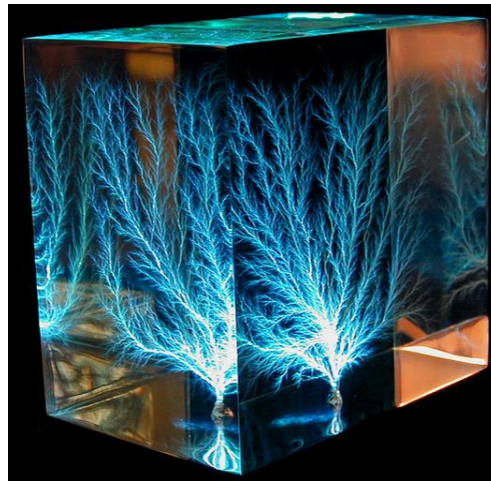


Figure 19: Lichtenberg figure built under high voltage in polymethyl methacrylate ^[91].

The treeing phenomenon can be observed in all dielectric wherever non-uniform fields prevail. If there are two electrodes separated by an insulating material and the assembly is placed in an outdoor environment, some contaminants in form of moisture or dust

particles deposit on the surface of insulation and leakage current starts between the electrodes through the contaminants. The current heats e.g. the moisture and causes breaks in the moisture films. These small films then act as electrodes and sparks are drawn between the films. The sparks cause carbonization and volatilization of the insulation material and lead to formation of permanent carbon tracks on the surface of insulations. Therefore, tracking is the formation of a permanent conducting path across the surface of insulation and is usually of carbon nature. For tracking to occur, the insulating material must contain organic substances. The rate of tracking can be slowed down by adding fillers to the polymer which inhibit carbonization ^[38,90].

1.6.4 Thermal Breakdown

When an insulating material is subjected to an electric field, the material gets heated up due to conduction current and polarization related dielectric losses. The conductivity of the material increases with increasing temperature. When the heat generated exceeds the heat dissipated by the material, a condition of instability is reached resulting in breakdown of the material. Figure 20 shows three heating curves corresponding to different electric stresses as a function of specimen temperature. Newton's law of cooling is represented by a straight dashed line, assuming that the temperature difference between the ambient and the specimen temperature is small.

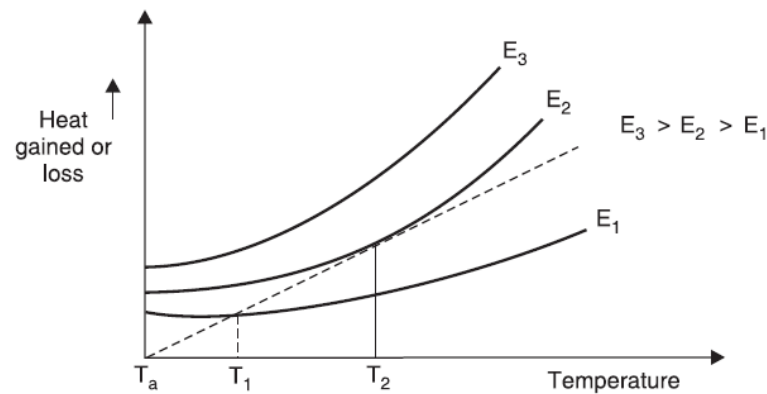


Figure 20: Heating curves of solid dielectrics depending on application of different electrical fields E_1 , E_2 and E_3 . The dashed straight line represents heat loss due to cooling and is derived from Newton's law of cooling ^[90].

At E_1 an equilibrium between heat loss and gain is reached at T_1 . With increasing specimen temperatures more heat is dissipated due to cooling than generated, resulting in thermal stability of the dielectric against the electrical field. The equilibrium for E_2 is reached at T_2 but with increasing specimen temperature the heat gain dominates. This

results in a thermal breakdown of the dielectric. For E_3 the state of equilibrium is never reached and hence the specimen will break down thermally.

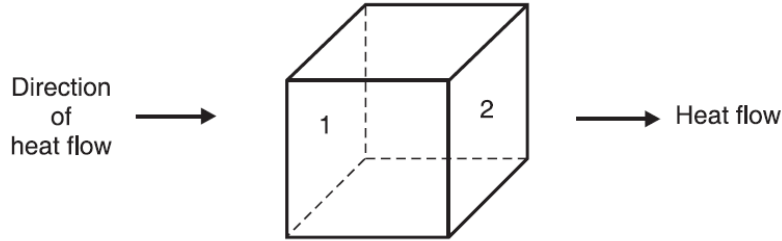


Figure 21: Heat flow through cubic volume element ^[90].

In order to obtain basic equation for studying thermal breakdown, an exemplary volume within the dielectric specimen element can be considered as small cube. This is shown in Figure 21. The side difference is Δx and temperature difference across its faces in the assumed direction of heat flow in x -direction is ΔT . Therefore, the temperature gradient can be defines as

$$\frac{\Delta T}{\Delta x} = \frac{dT}{dx} \quad (18)$$

With $\Delta x^2 = A$ the heat flow across face 1 is

$$KA \frac{dT}{dx} \text{ Joules} \quad (19)$$

and heat flow across face 2

$$KA \frac{dT}{dx} - KA \frac{d}{dx} \left(\frac{dT}{dx} \right) \Delta x \quad (20)$$

In this equation the second term indicates the heat input to the differential specimen. Therefore, the heat absorbed by the differential cube volume is

$$= \frac{KA \frac{d}{dx} \left(\frac{dT}{dx} \right) \Delta x}{\Delta V} = K \frac{d}{dx} \left(\frac{dT}{dx} \right) \quad (21)$$

It is assumed, that the heat input to the block will be partly dissipated into the surrounding and partly raise the temperature of the block. C_V is the thermal capacity of the dielectric, σ the electrical conductivity and E the electric field intensity. The heat which is generated

by the electric field is σE^2 watts, and the rise in temperature of the block is ΔT , in time dt , the power required to raise the temperature of the block by ΔT is

$$C_v \frac{dT}{dt} \text{ watts} \quad (22)$$

Therefore,

$$C_v \frac{dT}{dt} + K \frac{d}{dx} \left(\frac{dT}{dx} \right) = \sigma E^2 \quad (23)$$

The solution of the above equation will give the time required to reach the critical temperature T_c for which thermal instability will be reached and the dielectric loses its insulating properties. In order to obtain solution of the equation, certain practical assumptions can be made. This solution is done by consideration of an extreme situation because C_v , K and σ are all functions of temperature and in fact σ may also depend on the intensity of electrical field.

Under assumption, that the heat absorbed by the block is very fast and heat generated due to the electric field is utilized in raising the temperature of the block and no heat is dissipated into the surroundings. Therefore, an expression for what is known as impulse thermal breakdown is obtained. The main equation reduces to

$$C_v \frac{dT}{dt} = \sigma E^2 \quad (24)$$

The objective is to obtain critical field strength E_c which will generate sufficient heat very fast so that above requirement is met.

With
$$E = \left(\frac{E_c}{t_c} \right) t \quad (25)$$

and the assumption that the field being a ramp function

$$\sigma E^2 = C_v \frac{dT}{dt} = C_v \frac{dT}{dE} \cdot \frac{dE}{dt} \quad (26)$$

and

$$\sigma = \sigma_0 e^{-u/KT} \quad (27)$$

where K is Boltzmann's constant and σ_0 is the conductivity at ambient temperature T_0 . Substitution of these values in the simplified equation leads to

$$\sigma_0 e^{-u/KT} E^2 = C_V \frac{dT}{dt} = C_V \frac{dT}{dE} \cdot \frac{dE}{dt} \quad (28)$$

Substitution of (28) with

$$\frac{dE}{dt} = \frac{E_c}{t_c}$$

leads to

$$\sigma_0 e^{-u/KT} E^2 = C_V \frac{dT}{dt} \cdot \frac{E_c}{t_c} \quad (29)$$

or

$$\sigma_0 E^2 \frac{t_c}{E_c} dE = C_V e^{u/KT} dT \quad (30)$$

Integration of
left side

$$\frac{\sigma_0}{C_V} E^2 \frac{t_c}{E_c} \int_0^{E_c} E^2 dE = \frac{\sigma_0}{C_V} \frac{t_c}{E_c} \cdot \frac{1}{3} E_c^3 = \frac{1}{3} t_c \frac{\sigma_0}{C_V} E_c^2 \quad (31)$$

Integration of right
side

$$\int_{T_0}^{T_c} e^{u/KT} dT \rightarrow T_0^2 \frac{K}{u} e^{u/KT_0} \quad (32)$$

In case of $T_c \gg T_0$

$$E_c = \frac{3C_V}{\sigma_0 t_c} \cdot \frac{KT_0^2}{u} e^{u/KT_0} \quad (33)$$

The expression in (33) shows that the critical condition requires a combination of critical time and critical field. However, the critical field is independent of the critical temperature due to the fast rise in temperature.

1.6.5 Electrochemical Breakdown

Whenever cavities are formed in solid dielectrics, dielectric strength in these solid specimen decreases. When gas in the cavity breaks down, the surfaces of the specimen provide instantaneous anode and cathode. Some of the electrons with sufficient energy dashing against the anode can break the chemical bonds of insulation surface. Similarly, positive ions bombarding against the cathode can increase the surface temperature and therefore produces local thermal instability. Chemical degradation may also occur from the active discharge products *e.g.* O₃, NO₂ etc. formed in air. The net effect of all these processes is a slow erosion of the material and a consequent reduction in thickness of the specimen. Normally, it is desired that the dielectric strength of the specimen should not decrease with ageing. However, because of defects in manufacturing processes and/or design, the dielectric strength decreases with time of voltage application. The decrease in dielectric strength E_b with time follows the following empirical relation ^[90].

$$t \cdot E_b^n = \text{const.} \quad (34)$$

where the exponent n depends upon the dielectric material, the ambient temperature, humidity and the quality of manufacture.

1.6.6 Dielectrical breakdown of nanocomposites

The importance of polymer nanocomposites was recognized for the first time in 1994 by *Lewis* ^[92]. Since then, much work has been done. The first two papers with promising experimental data were published in 2002 by *Imai et al.* and *Nelson et al.* ^[93,94]. Polymers such as polyamide (PA), polyethylene (PE), polypropylene (PP), ethylene vinyl acetate (EVA), epoxy resins and silicone rubbers were combined with nano-fillers such as layered silicate (LS), silica (SiO₂), titania (TiO₂), and alumina (Al₂O₃). It was found that nano-filler addition has a distinct positive effect on electrical characteristics, resistance to high voltage environment and thermal endurance. Later, *Tanaka et al.* pointed out, that polymer nanocomposites are expected to emerge in the society of electrical insulation technology ^[95].

The positive effect of the presence of nanoparticles in a polymer matrix in terms of dielectrical properties are assumed to arise from several phenomena. First of all, Nanoparticles and their interfaces with the polymer matrix create changes in polymer structure. Near the surface of the nanofiller, a highly immobilized layer is developed. This

can be due to e.g. bondings between polymer and nanofiller. This bound layer influences the region surrounding the particle. The size of the bound layer affects properties of nanocomposites such as mobility of polymer chains, local charge distribution, chain conformation, molecular weight, chain entanglement density, free volume, crystallinity, crosslink density and trap site density and depth ^[96,97]. *Nelson et al.* pointed out in different publications, that although the evidence of these changes in properties, the extent influence on dielectric properties will depend on the kind of matrix polymer and nanofiller and the nature of the interaction zone ^[93,98,99].

Furthermore, local conductivity regions can be created around nanofillers. These regions can reduce the effect of space charge and therefore help in controlling electric field distribution and dielectric breakdown strength ^[100–102]. This local conductivity region allows charge dissipation and is formed around the nanoparticles that overlap partially. This is shown in following Figure 22.

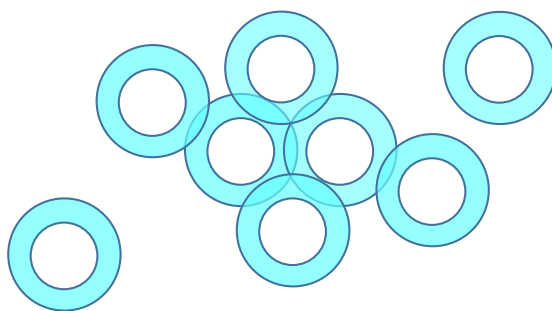


Figure 22: Formation of local conductivity region via overlapping of surrounding layers of nanoparticles embedded in a polymer matrix.

Li et al. reported, that as long as the percolation threshold has not been exceeded and dispersion is in nanoscale, the bulk conductivity remains unaffected ^[103].

Another effect is a change in crystallinity of the polymer matrix of composites induced by nanofillers ^[97]. In various publications, *Kozako et al.* conclude that layered silicates act as nucleating agent in a polyamide matrix. This results in formation of crystalline areas around the fillers leading to high crystallinity. Furthermore they reported, that the size of the crystals is also smaller than without nanofillers ^[104–107]. *Bamji et al.* reported, that charges could be trapped at interfaces of layered silicate and polypropylene and thus decrease the probability of a breakdown ^[108]. Traps are regions of lower potential energy in material volume. The density and depth of trap sites are assumed to be altered in nanocomposites. Charge carriers are more often and more easily trapped in trap sites than in reference matrix material. Due to this carriers, charges are accelerated over shorter distances and have reduced mobility and kinetic energy. This mechanism can be also

thought of as a scattering mechanism. The energy of charge carriers is distributed more evenly in the polymer and thus causes less damage in the material resulting in prolonging the lifetime of the composite.

In order to interpret the property changes due to addition of nanofillers, several theoretical models of the behaviour of nanocomposite have been developed ^[96,109]. As described earlier, understanding the interface phenomena is the key to changes in properties of composites. The multi-layered core model developed by *Tanaka et al.* concentrates on the interpretation of the role of interface phenomena ^[38,110,111].

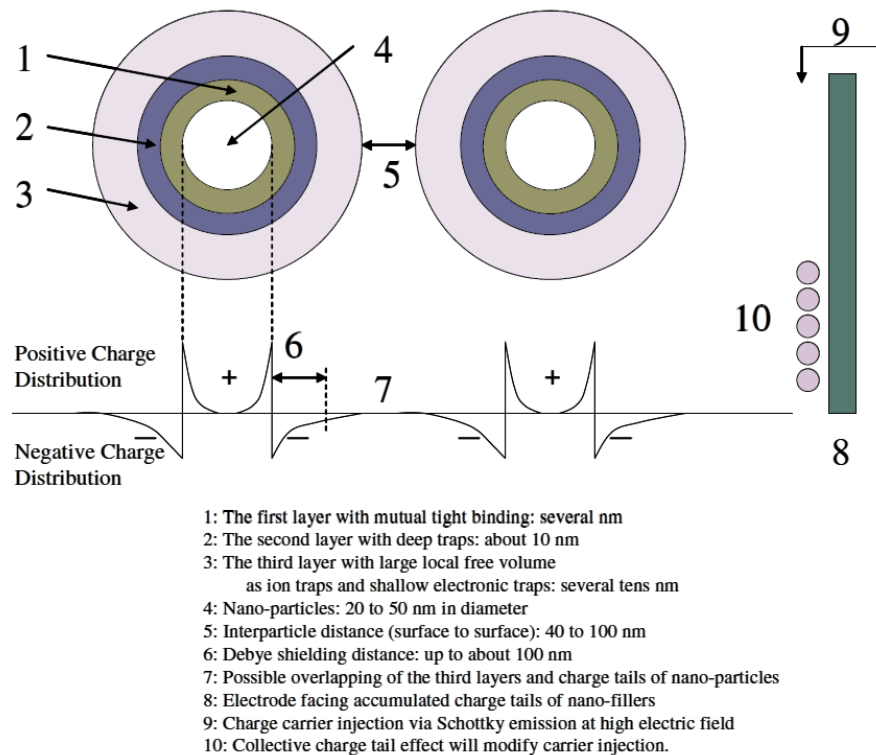


Figure 23: Multi-core Model of Tanaka to interpret several phenomena in dielectrical changes of polymer nanocomposites ^[111].

The multi-layered core model is a three-core model. It consists of a bonded layer, a bound layer and a loose layer. First layer thickness is in the order of 1 nm and is tightly bonded by coupling agents to both, nanofiller and matrix polymer. The second layer is about 10 nm in thickness. It consists of polymer chains bound or interacting to the first layer and the surface of the nanofiller. The third layer is several tens of nm in thickness and is characterized by chain conformations, chain mobility and free volume or crystallinity from the polymer matrix. The thickness of the layers depends on the strength of the polymer-nanofiller interaction. In analogy to colloidal chemistry, a Gouy-Chapman diffuse layer overlaps the three layers of the multi-layered core model. Nanoparticles are

charged positively or negatively when the polymer has mobile charge carriers. The charge is distributed over the interface. In the Gouy-Chapman diffuse layer the charge declines exponentially with distance. The Debye shielding length is approximately 30 nm. *Tanaka et al.* conclude that the model can be applied to explain e.g. characteristics of nanocomposites of layered silicate and polyamide. But they further pointed out that continuing studies are needed to establish a more precise model.

1.7 Functional trialkoxysilanes

Functional trialkoxysilanes have a general structure of $R'Si(OR)_3$. They are widely used in academic research and numerous industrial applications as coupling agents. The target is to enhance interphase adhesion of polymeric matrices and inorganic solids ^[112–114]. The mechanisms of these coupling reactions are related to the presence of two types of reactive moieties within their structure. They respond in different ways, according to substrates they approach. On one hand, the alkoxy groups OR enable the silane to be anchored to surface hydroxyl groups ^[115–117]. On the other hand, organic functionality R_2 , e.g. epoxy, vinylic, amine etc., improves their compatibility or can be used for copolymerization or grafting with polymer matrices. This leads to enhancement of the interfacial adhesion between both phases ^[112,118]. The general structure and typical functionalities for substituents R and R' are summarized in Figure 24.

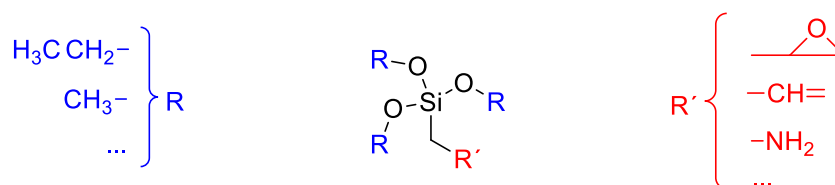


Figure 24: Scheme of trialkoxysilane with typical substituents e.g. methyl and ethyl for R and epoxy, vinyl and amino functionalities for R'.

Usually, the surface treatment is carried out with silane in a water–alcohol solution. The water induces stepwise hydrolysis of the silane ^[119] building the corresponding silanol derivative $R'-Si(OH)_3$. It promotes the silane adsorption onto OH-rich substrates through hydrogen bonding. The actual chemical bonding leads to siloxane bridges ^[120,121]. A reaction scheme is provided in Figure 25.

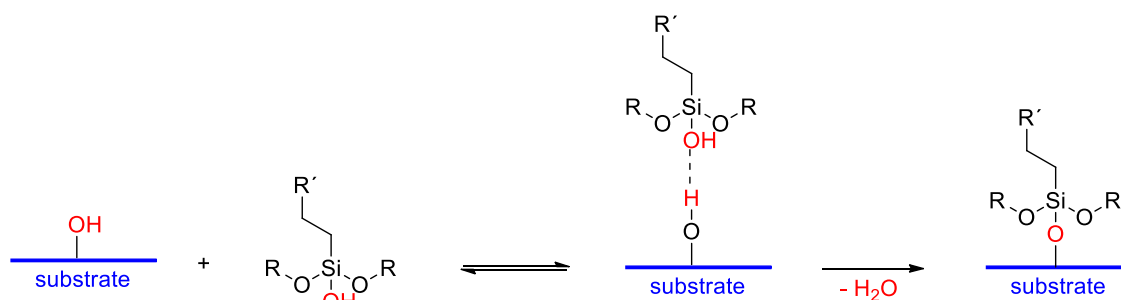


Figure 25: Reaction scheme of condensation of hydrolysed alkoxy silane onto OH-rich substrate.

Subsequently after solvent evaporation, residual silanol groups are able to undergo further condensation reaction with substrate hydroxyl groups. But also self-condensation resulting in formation of a polysiloxane network on the surface is possible ^[120–122]. As a result of the condensation of the silanol groups with each other and with respective alkoxy groups, dimeric and oligomeric structures are formed ^[123–125].

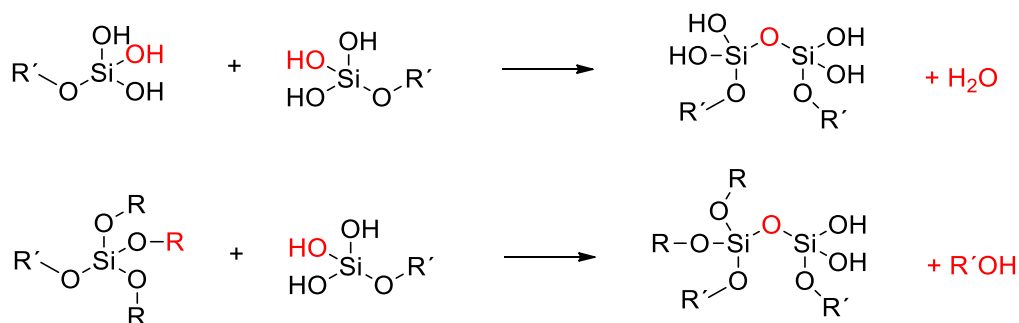


Figure 26: Examples of dimerization of trialkoxysilanes via condensation-reaction of silanol groups or reaction of alkoxy and silanol groups.

Further condensation reactions lead to gel-like networks, which precipitate in form of colloidal particles. Both, the hydrolysis and the condensation reactions of the silanol groups are affected by the structure of silane's organic part and by the medium composition. Influencing parameters are temperature, pH, concentration, amounts of water and the usage of catalysts ^[126,127]. The degree of oligomerization and extent of silane hydrolysis are known to exert a great influence on the silane adsorption and on its configuration at the substrate surface ^[120,128]. Therefore, these two parameters must be controlled in order to optimize the surface modification with silane coupling agents.

Chapter 2: Concept of thesis

In this study, the effects of internal interphase modification in nanocomposites of montmorillonite and polyamide-imide on thermal, mechanical and dielectrical properties are investigated. At the theoretical section of this thesis it could be shown that in comparison to conventional micron-sized filled composites, nanocomposites of exfoliated layered silicate show extraordinary improvements in a variety of properties. The main reason for improved properties in nanocomposites is related to a stronger interfacial interaction between the polymer matrix and layered silicate. From basic micromechanical models it could be stated that the ratio of the composite modulus to the matrix modulus values tends to increase with the exfoliation of platelets. Derived from this, one main part of this thesis focuses on new methods of synthesis of completely exfoliated nanocomposites from MMT. In terms of mechanical properties, the behaviour of polymer–nanofiller composites is directly related to their hierarchical micro-structures. Mechanical properties of polymer–nanofiller composites are controlled by several microstructural parameters such as properties of the matrix, properties and distribution of the filler as well as interfacial bonding. Furthermore, synthesis and processing methods are important influencing factors. Interfaces are known to influence the effectiveness of load transfer from the polymer matrix to nanofillers. Thus, surface modification of nanofillers is needed to promote better dispersion of fillers and to enhance the interfacial adhesion between matrix and fillers. In this thesis the silane APTES was chosen to provide covalent bonding between matrix and filler.

PAI merges both, greater mechanical properties typically linked with polyamide and the high thermal stability and solvent resistance derived from polyimide. Because these

properties enable PAI's general use as insulation coatings for e.g. magnet wires, foils and circuit boards, another focus was set on dielectrical properties.

The basic principle of synthesis for the characterization of nanocomposite-properties base on polyamide-imide filled with exfoliated montmorillonite in form of organically-modified Cloisite 30B (C30B). To investigate the influence of the implementation of these and how interphase modification through covalent bonding effects the overall properties, three general types of samples are designed. The process is illustrated in following Figure 27.

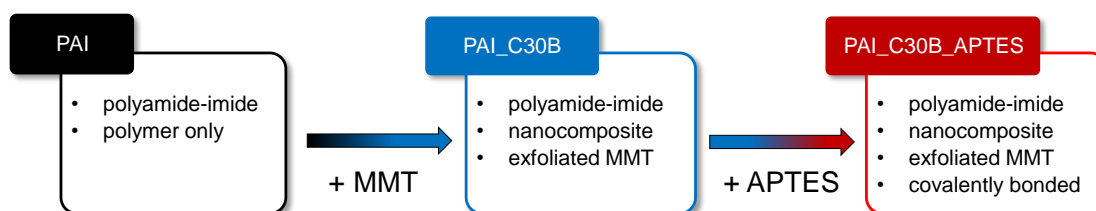


Figure 27: Concept of sample synthesis of pure PAI (black), PAI_C30B (blue) and PAI_C30B_APTES (red).

The first one is PAI which consists of polymer only. In a next step PAI_C30B nanocomposites are formed through addition of MMT. Silane modification at the surface of MMT-particles via γ -Aminopropyltriethoxysilane (APTES) will introduce covalent bonding at polymer/particle-interphases. PAI_C30B as well as PAI_C30B_APTES are builded up from the same polymer sample in order to provide optimal conditions of comparability.

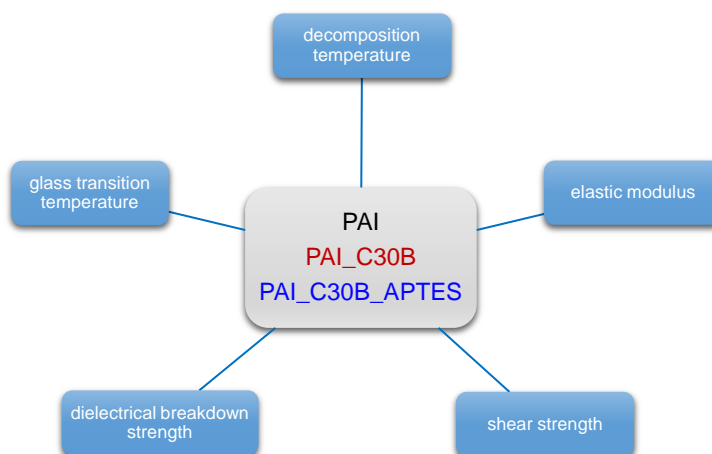


Figure 28: Matrix of key points in the fields of thermal, mechanical and dielectrical properties of nanocomposites.

The target of this thesis is to determine the effect of modified interphases on the resulting key properties in the field of thermal, mechanical and dielectric properties. This is shown schematically in Figure 28.

As shown in chapter 1.4, the ratio of the composite modulus to the matrix modulus values tends to decrease as more platelets are incorporated into the stack. Accordingly, incomplete exfoliation has a very significant detrimental effect on the mechanical reinforcement efficiency.

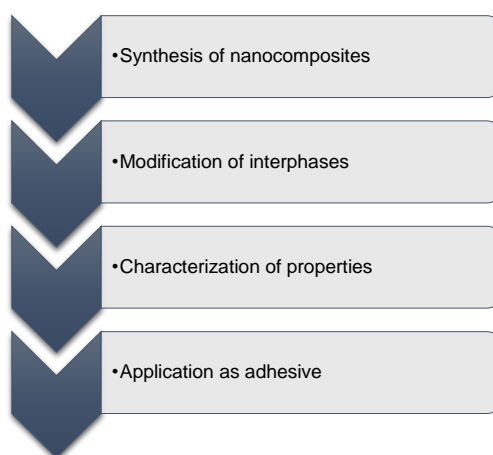


Figure 29: Scheme of key parts of dissertation.

Because of that, the first step focuses on the synthesis of exfoliated PAI-MMT-nanocomposites which is shown in Figure 30. Here, different approaches of synthesis are investigated and compared. The next part deals with quantitative and qualitative investigations on the modification of interphases and the covalent bonding of MMT to PAI. After this part the above described types of samples are characterized in terms of their properties. In the last part, basic studies of the application as adhesive will be conducted in order to investigate the fractural behavior of samples and allows insights in the mechanics of materials.

Chapter 3: Synthesis of nanocomposites

3.1 Introduction

Proper selection of organoclays depends mainly on the type of polymer matrix used and represents the key to dispersibility. *Fornes et al.* investigated the effect of the structure of alkylammonium compounds on the dispersion of MMT in polyamide-6 during melt compounding [71]. They reported that alkylammonium-compounds consisting of one alkyl tail is more effective than the quaternary cation having two alkyl tails in forming exfoliated nanocomposites. They explained this in terms of competition between the effects of platelet–platelet interactions and the interaction of the polymer with the organoclay platelet. The montmorillonite used in this study is organophilic modified by ion exchange with cationic quaternary alkyl ammonium ions in order to process these particles in the organic PAI-matrix. This chemical treatment lowers MMT's surface energy and improves its wetting characteristics to the polymer matrix ^[23].

Two different types of modified MMT were chosen. The first one is a polar organoclay with the organic modifier methyl tallow bis-2-hydroxyethyl ammonium (product name Cloisite 30B, C30B). The simplified chemical structure is illustrated in the following figure.

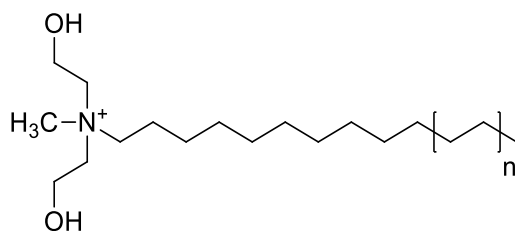


Figure 30: Simplified chemical structure of Cloisite 30B.

As alternative clay, a modification with dimethyl-benzylhydrogenated tallow quaternary ammonium as counter ion was chosen (product name Nanofil 9, NF9) having the simplified structure shown in the following Figure 31.

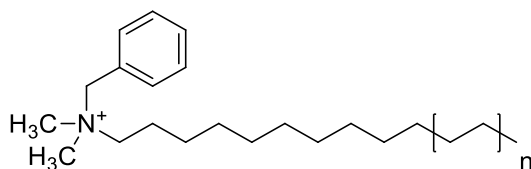


Figure 31: Simplified chemical structure of Nanofil 9.

The polymer matrix consists of polyamide-imide. As described in chapter 1.5, the most common approach for preparation of PAI resins is the diisocyanate route. It bases on the work of Hitachi Chemical Corp. [70]. Thereby, a diisocyanate reacts under heat with trimellitic anhydride in N-methyl pyrrolidone. The synthesis is performed stepwise. At the initial reaction temperature of 80 °C 4,4'-methylene diphenyl diisocyanate (MDI) and the anhydride group of TMA form a carboxylic acid ended polyimide oligomer [129]. At the second stage around 120 °C, amide groups are formed from the condensation of acid groups with the rest of MDI which combines the polyimide oligomers through the formation of amide and increases the overall molecular weight [129].

The physical mixture of PAI and layered silicate may not form a nanocomposite. In general, not ideal miscible systems show poor mechanical and thermal properties which derives from the poor physical interaction between organic and the inorganic components. In contrast, strong interactions between the polymer and the layered silicate lead to exfoliation of the inorganic phases resulting in dispersions at nanometer level. As a result, nanocomposites of layered silicate exhibit unique properties not shared by conventionally filled polymers [10–14]. Figure 32 exemplary shows the striven internal structure of polyamide-imide and organoclays.

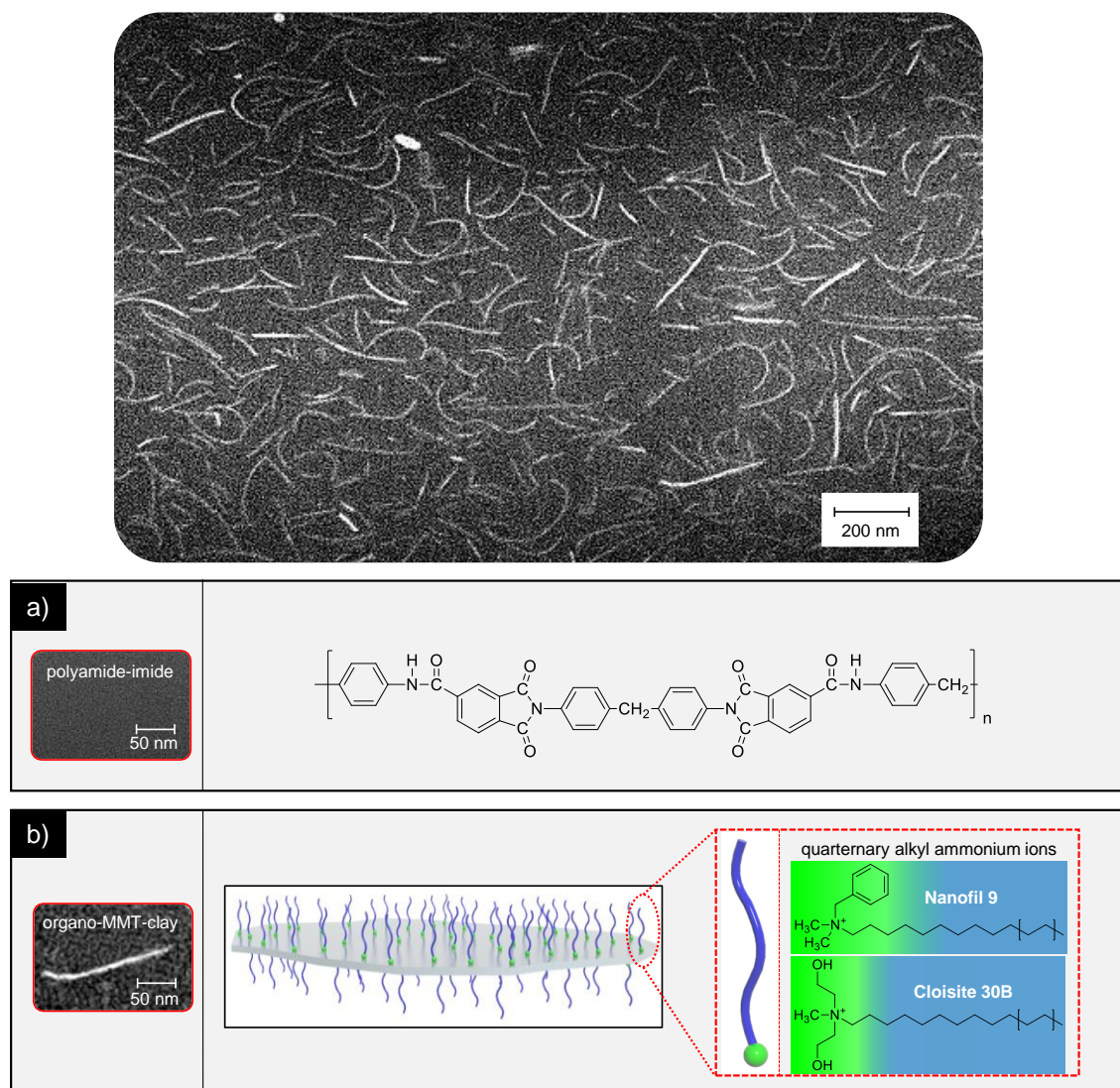


Figure 32: SEM image of FIB prepared cross section of the PAI matrix (dark, a) containing exfoliated MMT sheets (white, b) which are ion-exchanged with two types of quaternary alkyl ammonium ions.

In order to obtain exfoliated states of particles, different strategies were investigated. These are the solvent casting method and a new approach of synthesis via *in situ* polymerization.

3.1.1 Exfoliation of MMT via solvent casting

The solvent casting method is based on swelling MMT intergalleries with solvent where the polymer is soluble. It was first investigated by Aranda and Ruiz-Hitzky^[130]. Mixing of polymer and layered silicate solutions results in intercalation of polymer chains and displace the solvent within the interlayers of silicates. It is described as an entropy driven

process where the loss of entropy due to polymer intercalation is overcompensated by desorption of solvent. As it was shown by *Ranade et al.* exfoliated PAI-MMT-composites can be obtained via solvent casting method by premixing MMT with xylene followed by adding to a PAI solution. Exfoliated composites were obtained until a limiting MMT concentration of about 1.0 wt-%^[131]. The strategy of solvent casting in this study bases on the solely usage of NMP for the swelling process which is also solvent of the PAI solution.

3.1.2 Exfoliation of MMT via *in situ* polymerization

At *in situ* polymerization the layered silicate is swollen within either a liquid monomer or a monomer solution followed by polymerization within interlayer galleries of MMT. This approach is common and has been conducted for several polymer systems, except for PAI. For the diisocyanate route of PAI-polymerization there is the problem of high reactivity of the isocyanate monomer. During swelling process, it would undergo a reaction with the acid anhydride even at low temperatures. The strategy of the present work was to solve this problem by protection of the -NCO groups. Common protection agents (e.g. ϵ -caprolactam, MEKO, DIPA, DMP) exhibit deblocking temperatures of 100-190 °C^[132]. In order to enable the first reaction step of imide oligomer formation at PAI-synthesis around 80 °C the challenge for the protection agent in this study is the requirement of a very low deblocking temperature.

The concept in this work was to realize *in situ* polymerization via protection of MDI. It was inspired by works of *Chen and Ho*^[129,133]. They investigated a PAI synthesis derived from MDI which was blocked by *p*-chlorophenole (PCP). This method was adapted in the present work for a new approach of *in situ* polymerization. The target was to enable swelling MMT with the PAI monomers MDI and TMA simultaneously under absence of reaction. Subsequent addition of Tri-*n*-butyl amine (TBA) catalyses in a first step the deblocking reaction of PCP which enables polymerization within intergalleries of MMT. As result, exfoliation of the stacked MMT structure should be achieved.

3.1.3 Characterization of exfoliation

By monitoring the position, shape, and intensity of the basal reflections from distributed silicate layers, the structure of nanocomposite (intercalated or exfoliated) were identified. At exfoliated nanocomposite, the extensive layer separation associated with the delamination of original silicate layers in a polymer matrix results in the disappearance of coherent X-ray diffraction from the distributed silicate layers. However, for

intercalated nanocomposites, the finite layer expansion associated with the polymer intercalation results in the appearance of a new basal reflection. These correspond to the larger gallery height. Although XRD offers a convenient method to determine the interlayer spacing in the original layered silicates and in intercalated nanocomposites, little can be said about its spatial distribution. Likewise, some layered silicates initially do not exhibit well-defined basal reflections. This results in peak broadening and intensity decreases. Therefore, conclusions concerning the mechanism of nanocomposite formation and their structure had to be supplemented with visual methods like FIB-SEM or TEM. This allows a qualitative understanding of the internal structure, spatial distribution of the various phases, and views of the defect structure through direct visualization.

3.2 Experimental

3.2.1 Reagents and materials

Polyamide-imide was synthesized via diisocyanate route with 1,2,4-benzenetricarboxylic acid anhydride (TMA, 97 %, obtained from Sigma-Aldrich) and 4,4'-methylene diphenyl diisocyanate (MDI, 98 %, obtained from Sigma-Aldrich) in N-methyl pyrrolidone (NMP) as solvent. For *in situ* polymerization MDI was blocked with *p*-chlorophenole (PCP, 98 %, obtained from Merck) in toluene. Tri-*n*-butyl amine (TBA, 98.5 %, obtained from Sigma-Aldrich) was used as catalyst for blocking and deblocking reaction.

Two different MMT's were chosen for synthesis of nanocomposites. These are methyl tallow bis-2-hydroxyethyl ammonium (Cloisite 30B, C30B, Byk Chemie, obtained from Nordmann, Rassmann GmbH) and dimethyl-benzylhydrogenated tallow quaternary ammonium (Nanofil 9, NF9, Byk Chemie, obtained from Nordmann, Rassman GmbH). HDG zinc-coated steel was obtained from Voestalpine. The reagents and materials used in this study were applied without further purification.

3.2.2 Synthesis of PAI

TMA (327.98 g, 1.71 mol) and NMP (741.50 g) were added to a 2 L four-necked glass reactor under purging nitrogen gas and heated to 60 °C. The mixture was stirred until TMA was completely dissolved. Then the mixture was cooled down to 40 °C followed by addition of excess MDI (430.08 g, 1.72 mol).

Table 3: Variation of isothermal time per step during synthesis of PAI.

sample	t/step
	[min]
1	0
2	15
3	30
4	60

The reaction temperature was increased stepwise from 40 to 65, 75, 95 and finally to 130 °C. Isothermal time per temperature step was varied according to Table 3. The goal was to investigate the influence on the resulting polymer in terms of molecular weight distribution and dispersity. The reaction scheme for this synthesis is provided in Figure 33.

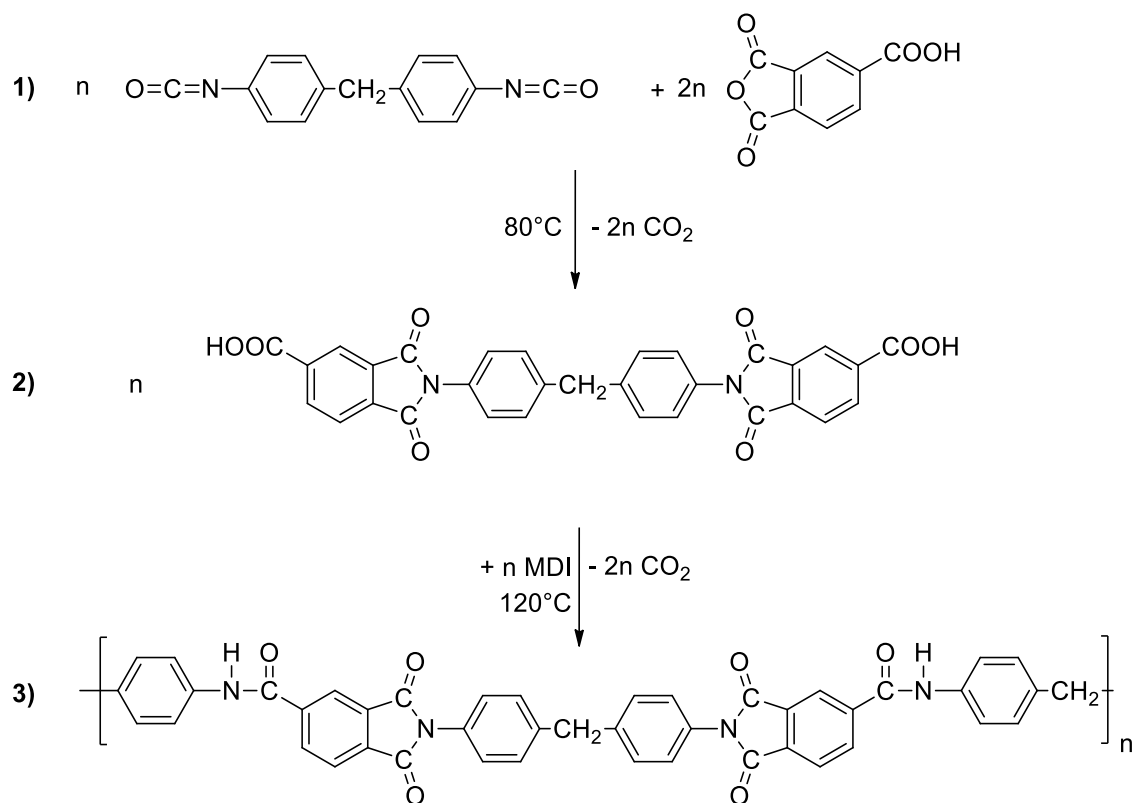


Figure 33: Synthesis of PAI via diisocyanate route. (1) Reaction of MDI and TMA to (2) diimide oligomere. (3) Further MDI reacts with oligomers under 120°C to polyamide-imide.

3.2.3 *In situ* polymerization

3.2.3.1 Blocking of MDI

The blocking reaction of MDI with PCP was performed according to *Ho* and *Chen* ^[133]. The reaction scheme is shown in Figure 34. MDI (60 g, 0.24 mol) was dissolved in 500 mL toluene at room temperature. Excess PCP (46.23 g, $n(\text{PCP}) / n(\text{MDI}) = 1.5$) was added and stirred until it was completely dissolved. After addition of 10 drops of TBA,

the formed b-MDI started to precipitate. Subsequently the temperature was increased to 40 °C and kept for 24 h.

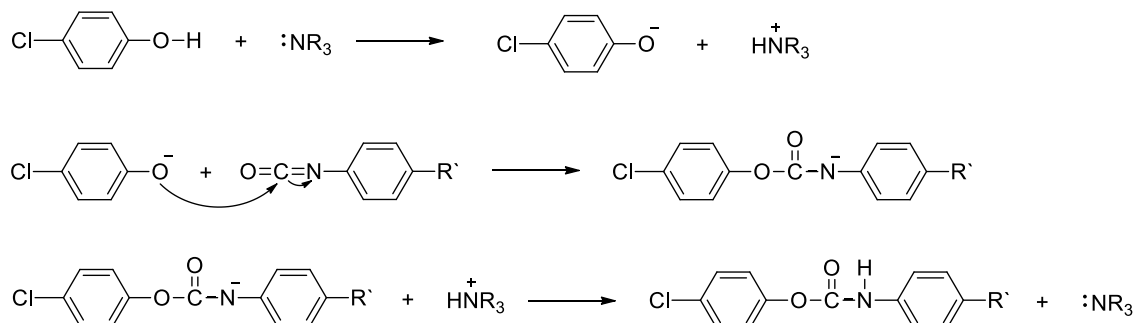


Figure 34: General blocking reaction of aromatic isocyanate with *p*-chlorphenole.

The product was filtered and washed several times with toluene followed by drying at 120 °C for 12 h. The dry *b*-MDI was processed via mortar in order to obtain a powder. Figure 35 shows the final *pcp*-blocked monomer of MDI.

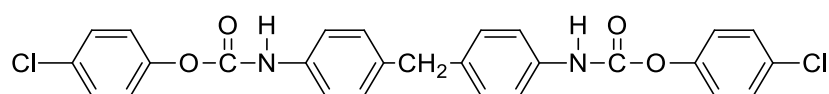


Figure 35: MDI monomer blocked by *p*-chlorphenole.

3.2.3.2 Synthesis of nanocomposites via *in situ* polymerization

For preparation of nanocomposites via *in situ* polymerization TMA (5.00 g, 0.03 mol), NMP (35.00 g) and MMT with varying concentration ($c_{\text{MMT}} = 1.0, 1.5, 2.0$ and 3.0 wt-% in dry composite film) were added to a three-necked glass reactor in nitrogen atmosphere and heated to 60 °C. The mixture was stirred until TMA was completely dissolved and cooled afterwards to 40 °C. Subsequently b-MDI (19.82 g, 0.04 mol) and in order to catalyse the reaction TBA (1.00 g) were added. The following polymerization was performed by increasing temperature profile analogous to the conventional synthesis of PAI (stepwise from 40 to 65, 75, 95 and finally to 130 °C; 30 min per step). A reaction scheme is provided in Figure 36.

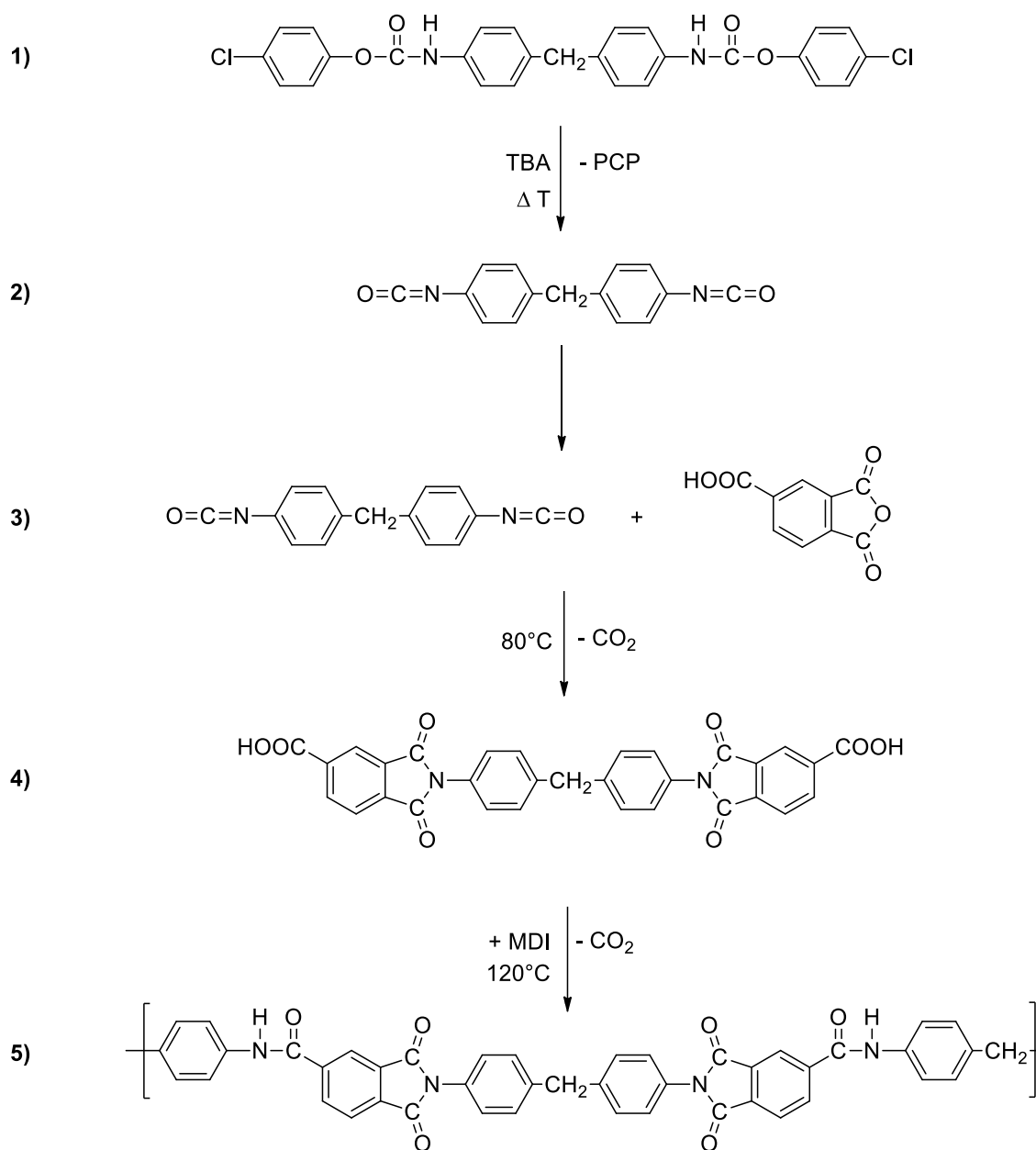


Figure 36: Reaction scheme for synthesis of PAI via diisocyanate route starting from PCP-blocked MDI. (1) PCP-blocked MDI monomer. (2) Deblocking reaction catalysed by TBA. (3) Reaction of MDI and TMA to (4) diimide oligomere. (5) Further MDI reacts with oligomers under 120°C to polyamide-imide.

3.2.4 Synthesis of nanocomposites via solvent casting

For preparation of nanocomposites via solvent casting method, different clay concentrations of C30B and NF9, respectively, were mixed with 20.00 g NMP in a vessel and stirred via magnetic stirrer for about 1 h. The different concentrations are summarized in Table 4:

Table 4: Concentrations of PAI-MMT-nanocomposites via solvent casting method.

m MMT (s)	m PAI (sol.)	C PAI (sol.)	C MMT/PAI (s)
[g]	[g]	[wt-%]	[wt-%]
0.1040	50.00	52.02	0.4
0.1561	50.00	52.02	0.6
0.2081	50.00	52.02	0.8
0.3121	50.00	52.02	1.2
0.5202	50.00	52.02	2.0
0.7803	50.00	52.02	3.0

Subsequently the mixture was placed under a disperser followed by dropwise addition of a solution of 52.00 g polyamide-imide at rotational speed of 400-600 rpm. After complete addition the composite was dispersed at 1200 rpm for 1 h. Afterwards XRD analyses were carried out in liquid state. In order to analyse particle distribution and exfoliation behaviour via SEM thin films were prepared on zinc-coated steel (HDG) and dried in an oven at 200 °C for 10 min. SEM images were taken at cross sections which were prepared via focused ion beam milling.

3.2.5 Characterization

In order to investigate swelling, intercalation and exfoliation of MMT sheets X-ray diffraction measurements were performed with Bruker D5005 (Cu-K α 0.154 nm). XRD measurements were conducted in transmission geometry using self-crafted fluid cells at angles between 2.5 and 6.0 °2 θ . FTIR spectra measured with Bruker Alpha-P (λ = 633 nm) allowed to draw conclusions regarding formation PAI during the *in situ*

polymerization. Computational simulations were performed to provide information about the equilibrium geometry of PCP-blocked MDI. They were conducted ab initio via Hartree–Fock and density functional theory using Becke's three-parameter hybrid method with the Lee, Yang and Parr correlation functional (B3LYP) and a basis set of 6-311+G^{**}.

3.2.6 Visualization of MMT distribution via SEM/FIB

Figure 37 shows an example for the Preparation of cross sections and imaging of particle distribution of MMT in PAI. They were conducted via Zeiss Neon 40 Crossbeam and crossbeam-preparation using a Canion Ga-FIB.

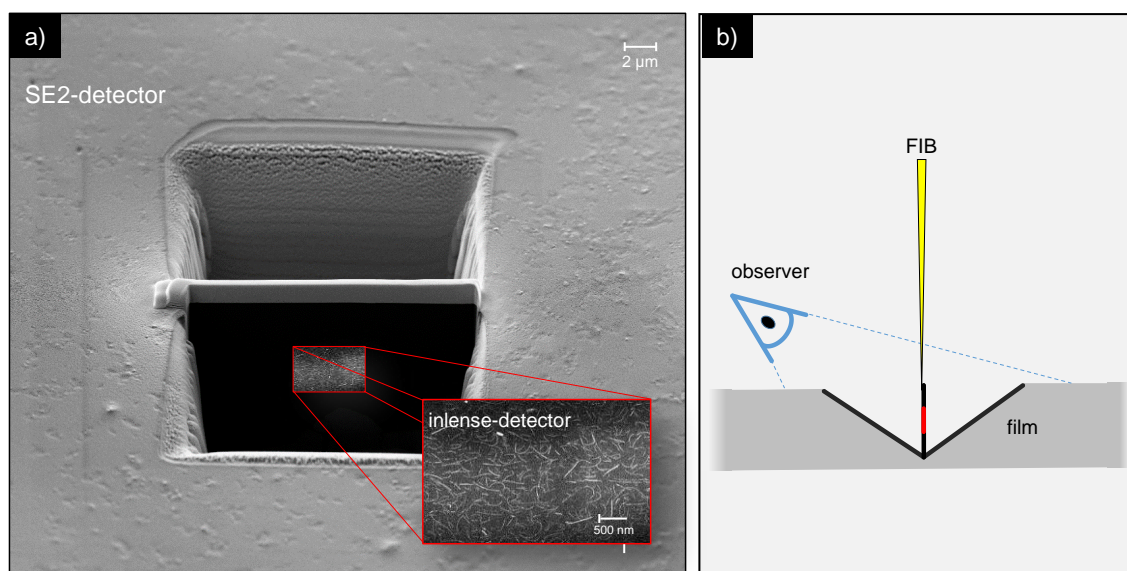


Figure 37: a) Preparation of cross-sections via focused ion beam milling. The overview image was taken via SE2-detector and the detail image (red rectangle) via inlense-detector. Dark parts derive from polyamide-imide and the white objects from MMT. b) illustrates the perspective from the observer's point of view.

Cross-sections of samples were prepared by focused ion beam milling. An image of a resulting cross-section is exemplary shown in Figure 37 (a). A focused beam of gallium ions was used to cut through specimen's volume slice by slice. This was performed twice until only a narrow bar remained. The overview image was taken via SE2-detector and the detail image (red rectangle) via inlense-detector. Dark parts derive from polyamide-imide and the white objects from MMT. Figure 37 (b) illustrates the perspective from observer's point of view.

Bar thicknesses were typically in the order of $d < 100$ nm which is shown in Figure 38. This technique enabled very high levels of magnification resulting pixel sizes below 1 nm.

A further advantage was the elimination of blurring effects of particles. This means, that without this technique, normally particles are strongly blurred due to emission of electrons originated several nanometers inside the surface of the specimen. Furthermore, different particles which are below the surface can strongly superimpose. Due to bar preparation of specimen this interfering volume was eliminated.

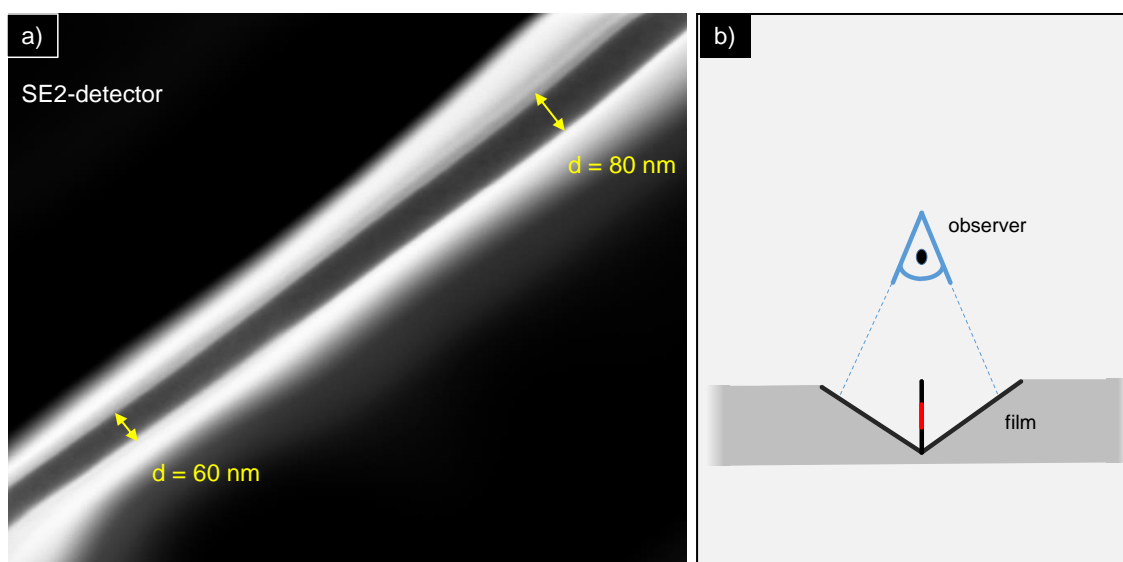


Figure 38: Top view of bar prepared from focused ion beam milling (a) and corresponding scheme of perspective (b).

3.3 Results and discussion

3.3.1 Synthesis of PAI

Synthesis of polyamide-imide was performed via reaction of MDI and TMA, as described in 3.2.2. Following scheme provides the two important stages of PAI-synthesis.

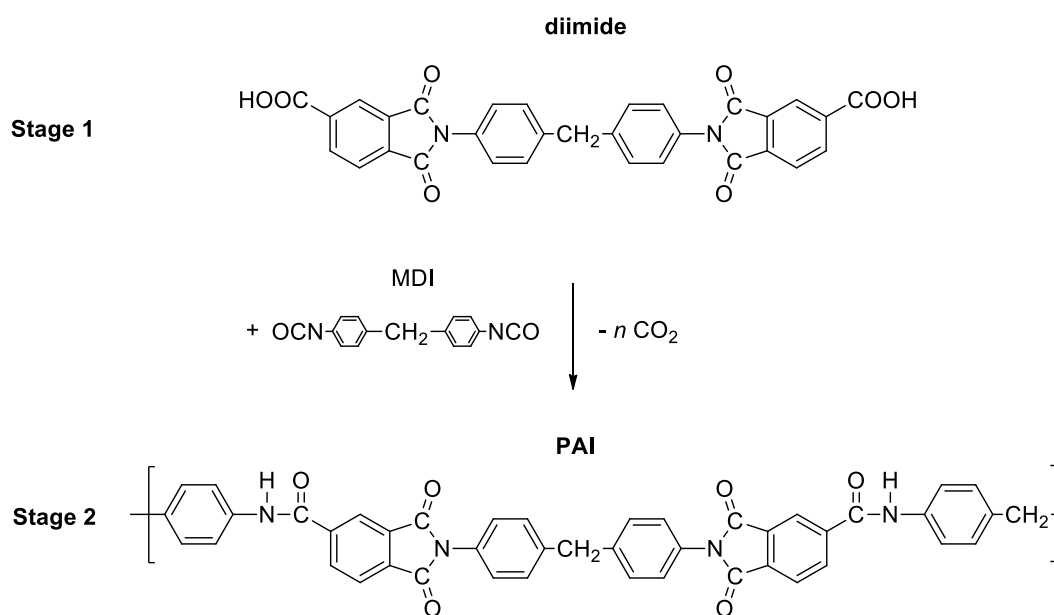


Figure 39: Key stages of PAI synthesis. Stage shows a diimide which is linked in stage 2 through amide reaction to the final polymer chain.

Because heating rate and isothermal time per step turned out to be crucial at preliminary tests, four different syntheses with varying time per step were performed. Chosen time steps were 0 min, 15 min, 30 min and 60 min.

Gel permeation chromatography was conducted afterwards, to determine resulting molecular weight distributions and dispersity. Figure 40 shows the measured molecular mass distributions of respective PAI solution in relation to isothermal time at each temperature step during synthesis.

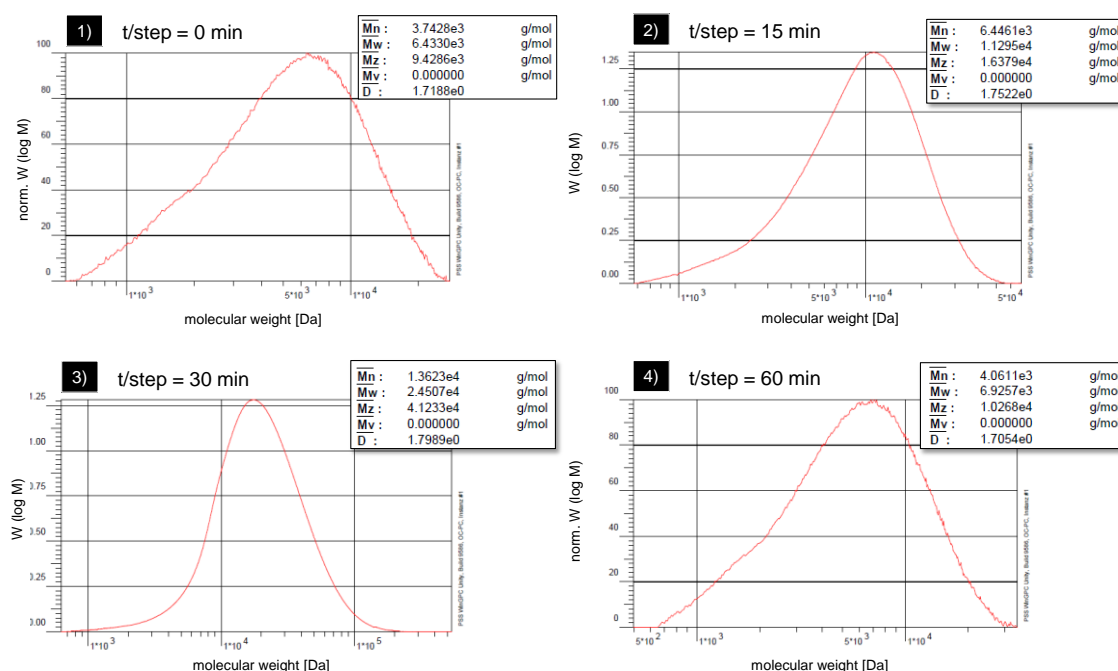


Figure 40: Molecular mass distribution of polyamide-imide via GPC in relation to isothermal time per step during synthesis. Determination of M_n , M_w , M_z and the dispersity index D .

For better comparability, number weighted molecular mass (blue bars) and indices of dispersity (red bars) in relation to reaction time per step are summarized in Figure 41.

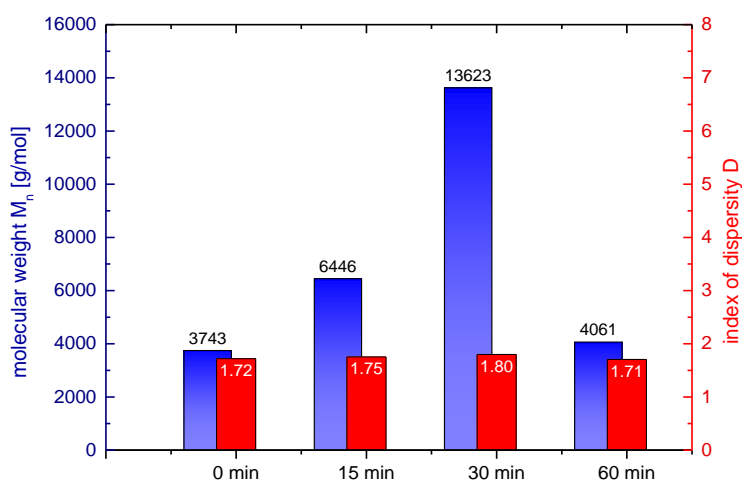


Figure 41: Summary of molecular weight M_n (blue bars) and indices of dispersity (red bars) of GPC-measurements on PAI in relation to isothermal reaction time per step during synthesis.

Results showed a distinct influence of reaction time per step on the molecular weight. Low weights are observed for continuous heating (0 min per step). It can be assumed, that

here the conversion to diimide oligomers was low due to insufficient reaction time. This would result in low amounts of pre-polymer which would form final polymer chains through amide reactions at high temperatures. By increasing time over 15 min to 30 min the maximum was observed. Further increasing of time resulted in an opposing effect. The average molecular weight dropped to initial level of 0 min. A possible explanation would be, that at the first stage of diimide oligomer formation the conversion was too high. Most of free isocyanate would have reacted so that they were not available for the second stage of reaction at higher temperatures where chain formation due to amide formation occurs. In terms of dispersity no significant differences were observed. The dispersity was around 1.7 to 1.8.

To conclude, the highest molecular weights were observed at 30 min reaction time per step. M_n was determined to 1.36×10^4 g/mol, the weight average molecular weight M_w to 2.45×10^4 g/mol and the size average molecular weight M_z was found to be 4.12×10^4 g/mol. The resulting dispersity was 1.7989. During the reaction from 80 °C to 130 °C large amounts of CO₂ development were observed. A highly viscous dark red to brown solution of PAI was obtained.

The reaction time of 30 min per step was chosen for all following PAI-syntheses in this work. In order to verify success of synthesis, a sample was taken and infrared spectroscopy was conducted. The resulting spectrum is provided in Figure 42.

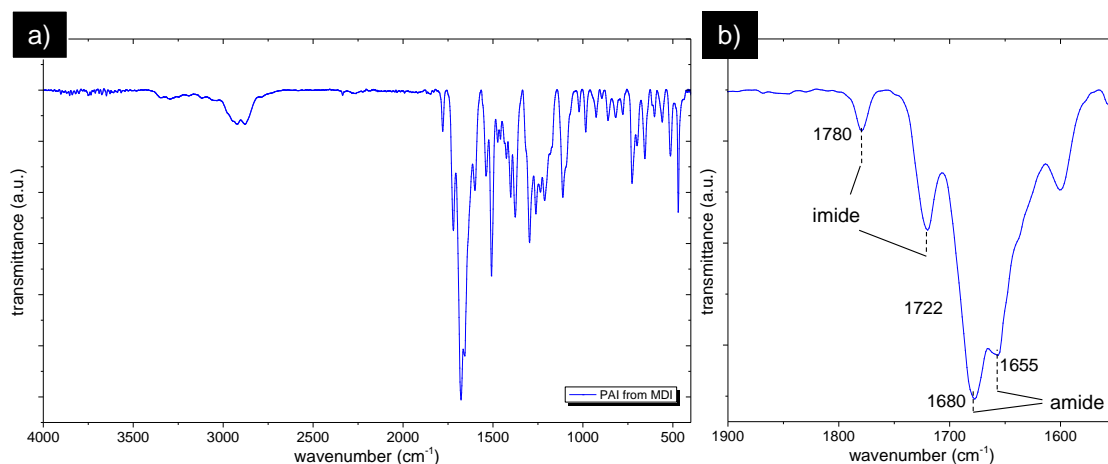


Figure 42: Overview FTIR spectra from 400 to 4000 cm⁻¹ of PAI obtained from diisocyanate route is shown on left side. Focus on PAI's characteristic vibrations of imide and amide between 1500 and 1900 cm⁻¹ on right side.

An overview from 400 to 4000 cm⁻¹ is provided on the left side in Figure 42 (a). The right side, Figure 42 (b), focuses on characteristic peaks of PAI. As can be seen, imide vibrations at 1780 and 1722 cm⁻¹ as well as amide vibrations located at 1680 and 1655 cm⁻¹ were present. Taking the absence of –NCO stretching vibration at 2265 cm⁻¹

into account, conversion of isocyanate was complete. Derived from these results evidence of successful PAI synthesis is provided.

3.3.2 *In situ* polymerization

The target of *in situ* polymerization (ISP) was to polymerize PAI within the intergalleries of MMT-layers. A scheme of this strategy is shown in Figure 43.

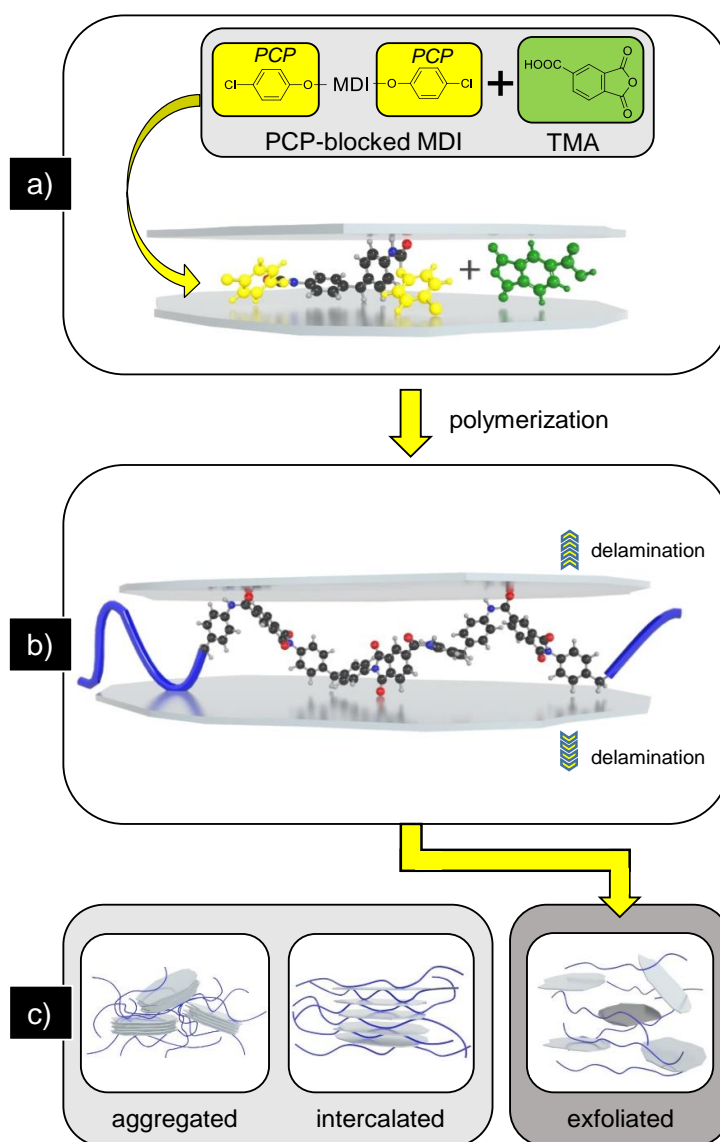


Figure 43: Reaction scheme of delamination/exfoliation process during *in situ* polymerization with PCP-blocked MDI.

At the first step (a), C30B and NF9 were swollen with the monomers b-MDI and TMA. In order to enable swelling, the instant reaction of monomers was avoided by blocking of

MDI with *p*-chlorophenole. Following polymerization to PAI within the intergalleries of respective MMT was initialized by addition of TBA as catalyst. The volume requirement of growing PAI segments within intergalleries of MMT was estimated to lead to drifting apart of sheets (b) until the attractive interactions are attenuated in a way that exfoliation into individual layers is caused (c).

Results indicate successful *in situ* polymerization of PAI-MMT nanocomposites. XRD measurements were carried out for initial powder of NF9 and C30B, MMT swollen with *b*-MDI and TMA and PAI-MMT composite after *in situ* polymerization. The observed peaks are assigned to d_{001} -intergallery spacing.

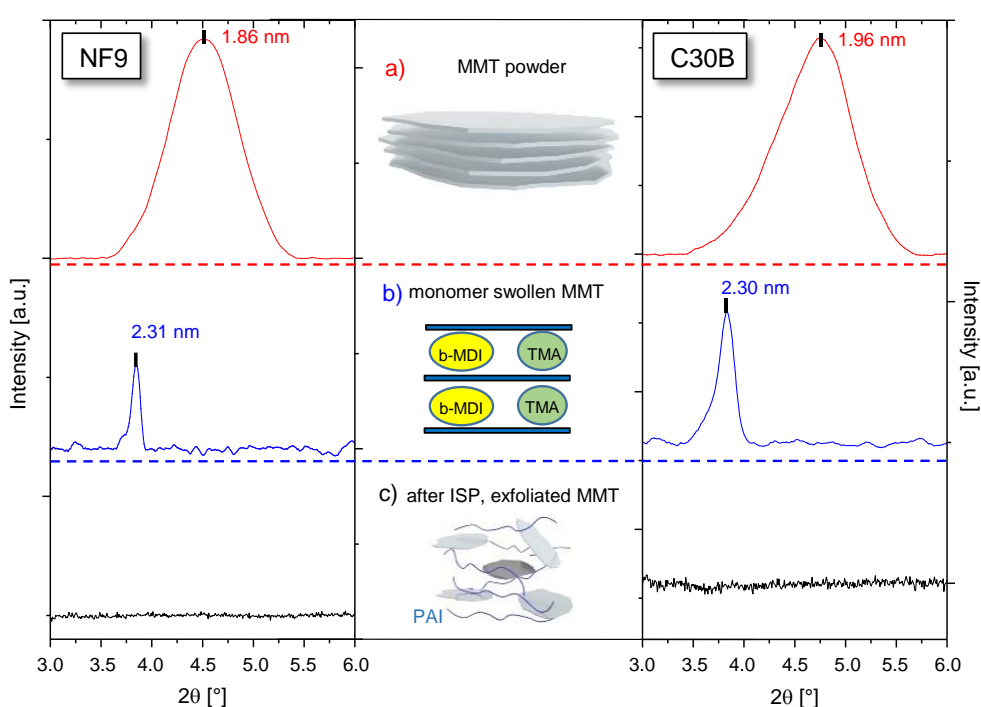


Figure 44: XRD-measurements during ISP: (a) NF9/C30B powder, (b) monomer swollen NF9/C30B and (c) exfoliated PAI-NF9/C30B-nanocomposite after *in situ* polymerization.

Initial measurements of NF9/C30B-powder showed peaks at $4.76^\circ 2\theta$ ($d = 1.86$ nm) for NF9 and $4.51^\circ 2\theta$ ($d = 1.96$ nm) for C30B (Figure 44.a). After swelling of MMT with *b*-MDI and TMA expansion of interlayer to $3.82^\circ 2\theta$ ($d = 2.31$ nm) for NF9 and $3.85^\circ 2\theta$ ($d = 2.30$ nm) for C30B was observed (Figure 44.b). Following *in situ* polymerization, intergallery peaks disappeared which indicated complete exfoliation of montmorillonite due to loss of d -spacing (Figure 44.c).

Computational simulations of PCP-blocked MDI were conducted to achieve information about its three-dimensional conformation and size (Figure 45).

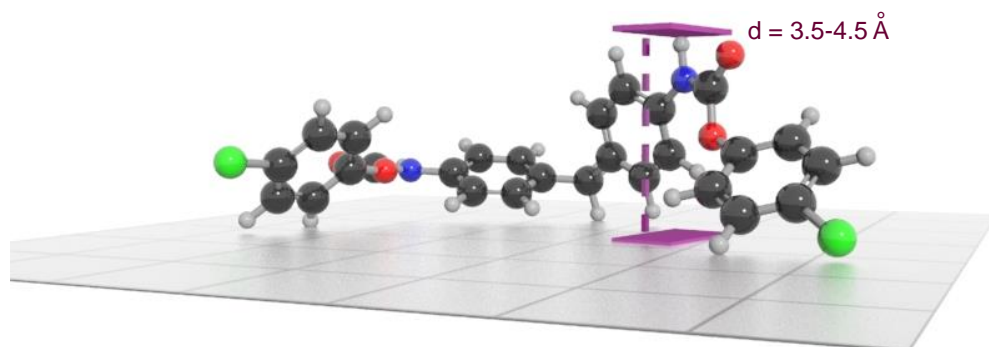


Figure 45: Computational simulation to provide equilibrium geometry of PCP-blocked MDI.

The measured dimensions of resulted geometry correlated to intergallery enlargement during the swelling process of MMT with b-MDI monomers. With $\Delta d_{001} = 0.35$ nm for C30B and $\Delta d_{001} = 0.45$ nm for NF9 the values correspond to the computational calculated dimensions $d = 3.5 - 4.5$ Å of b-MDI. These values were measured in consideration of MDI molecule's maximum space requirements depending on different orientations in intergalleries of MMT.

In order to determine a distinct limiting concentration at which stacked MMT particles could not be further exfoliated, experiments with increasing clay concentration (1.0, 1.5, 2.0 and 3.0 wt-%) were conducted. XRD-measurements were carried out determining the characteristic concentration at which appearance of d_{001} peaks occurred.

The results are shown in Figure 46. It can be seen in Figure 46 (a) for both C30B and NF9, that at concentrations below 2.0 wt-% of MMT the swelling peak around $3.8^\circ 2\theta$ disappeared while no further peak in the range of 2.5 to $6.0^\circ 2\theta$ was present. This indicates complete exfoliated states of particles. Above 2.0 wt-% peak formation around $4.0^\circ 2\theta$ showed an increasing amount of remaining polymer-intercalated MMT particles.

Furthermore, FIB-SEM analysis verified an exfoliated state of particles. Images which were taken directly after polymerization exhibited an inhomogeneous particle distribution. This changed after consecutive redispersing to a well spatial distribution of exfoliated particles. The limiting concentration for *in situ* polymerization with blocked MDI was therefore assumed to be at 2.0 wt-%. A distinct influence of MMT's organo-modification was not observed.

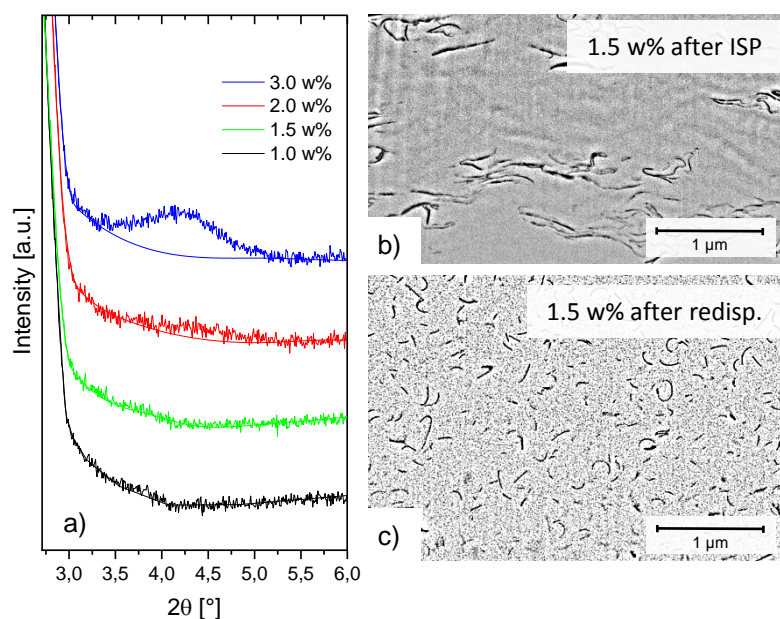


Figure 46: (a) XRD-measurements of ISP at different MMT-concentrations (1.0, 1.5, 2.0 and 3.0 wt-%). SEM- analyses indicate (b) inhomogeneous particle distribution right after in situ polymerization ISP and (c) homogeneous distribution after redispersing of (b).

To verify the success of PAI synthesis via *in situ* polymerization FTIR analyses were performed in liquid state of resulting PAI-MMT-nanocomposites (Figure 47). Apart from the decrease of --NCO stretching vibrations at 2270 cm^{-1} the focus was on the formation of characteristic imide and amide vibrations and compared to conventional synthesized polyamide-imide.

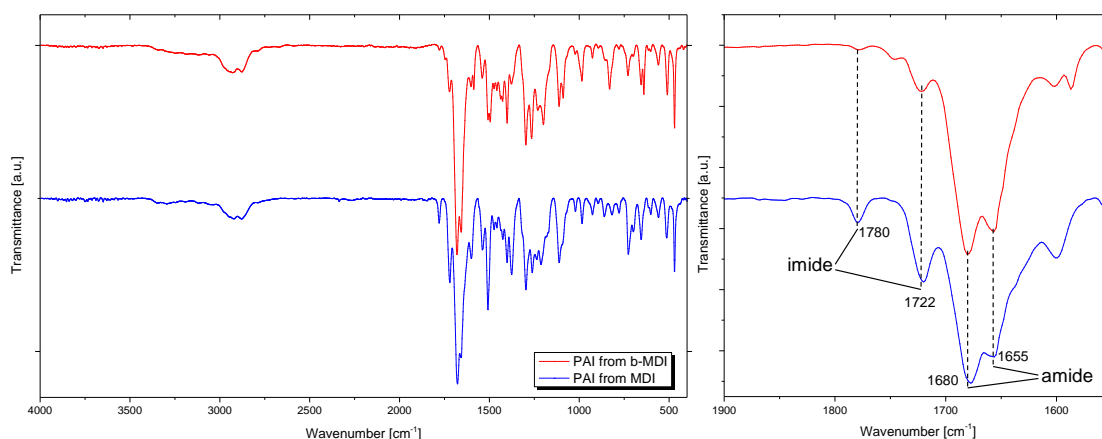


Figure 47: FTIR spectra of PAI from conventional PAI (blue) in comparison with PAI derived from in situ polymerization (red) with focus on PAI's characteristic vibrations of imide and amide.

These vibrations can be found for imide at 1780 cm^{-1} and 1722 cm^{-1} who are assigned to symmetric and antisymmetric C=O ring vibrations. Amide peaks were assigned to 1680 cm^{-1} and 1655 cm^{-1} . Resulting FTIR spectra showed that during *in situ* polymerization the same characteristic amide and imide structures were formed.

3.3.3 Solvent Casting

Another strategy to synthesize PAI-MMT-nanocomposites was performed by treatment of stacked MMT particles via solvent casting method. A scheme is shown in Figure 48. The basic idea of solvent casting to swell MMT with solvent followed by the intercalation of MMT's intergallery with polyamide-imide molecules to cause exfoliation due to enlargement of intergallery distances beyond limits of interlayer attractive forces.

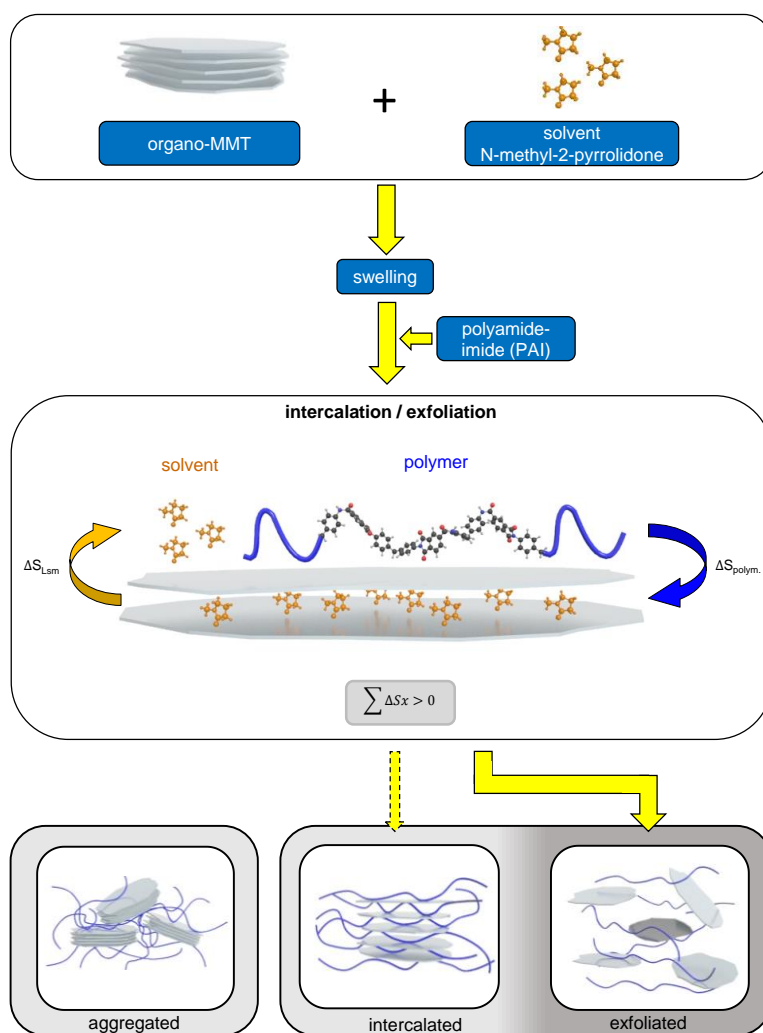


Figure 48: Reaction scheme of delamination/exfoliation process during solvent casting.

At the first stage, montmorillonite (C30B and NF9) were swollen in NMP which is also the solvent of PAI. After swelling, PAI was added dropwise. At this stage desorption of solvent molecules within the intergalleries of MMT is assumed to take place, while PAI chains interpenetrate the intergalleries. This results in enlargement of intergallery space until attractive forces are overcome and single layer drift apart. Intercalated and, more likely, exfoliated states of particle result.

In order to investigate particle distribution and success of exfoliation XRD measurements were conducted in liquid state. Afterwards PAI-MMT-nanocomposites with various concentrations were applied as ultra-thin layer of about 10 μm film thickness, dried in an oven at 200 $^{\circ}\text{C}$ and cross-sections were prepared via focused ion beam. These cross-sections were analyzed via SEM and compared to the measurements of X-ray diffraction. An overview of results is shown in Figure 49. An identical exfoliation behaviour of C30B and NF9 was observed, wherefore following detailed results solely focuses on C30B.

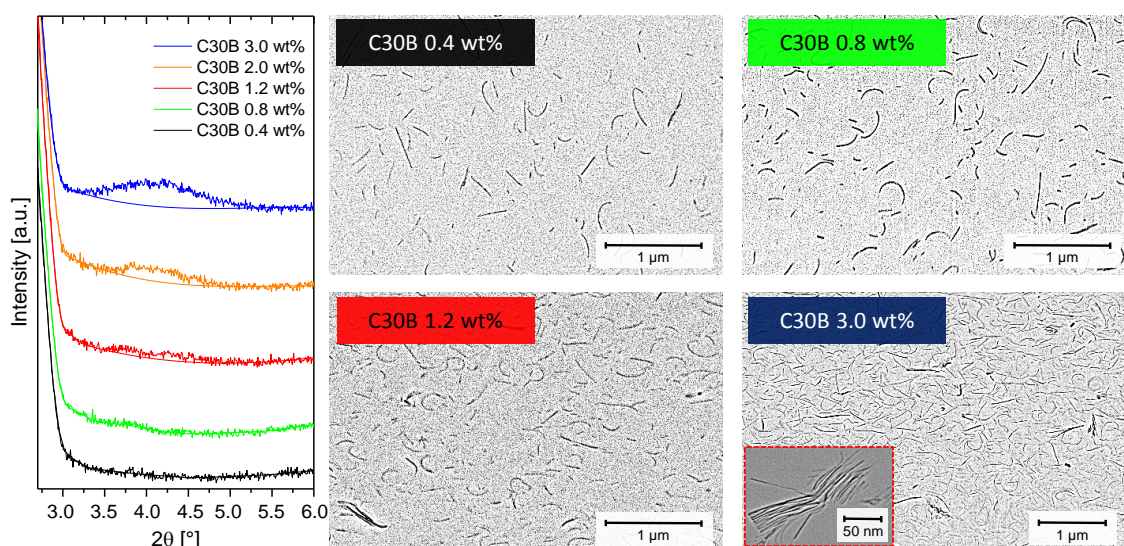


Figure 49: XRD-measurements and SEM analysis of Cloisite 30B with increasing clay content from 0.4 wt-% (black) to 3.0 wt-% (blue). Corresponding SEM images of cross-sections indicate exfoliated sheets for 0.4 and 0.8 wt-% (green) while remaining intercalated particle stacks occurred at concentrations above 1.2 wt-% (red). Red highlighted box at 3.0 wt-% shows details of intercalated MMT stacks.

Results showed a high degree of exfoliation and layer distribution at low clay loads. A distinct limiting concentration of about 1.2 % clay load was observed at which particles started to remain in intercalated state. This effect can be explained by reaching a percolation threshold. Samples with higher clay concentrations showed an increasing amount of intercalated instead of exfoliated particles. These results correlate with X-ray diffraction experiments. While samples below 1.2 % did not show the d_{001} peak

around $4.1^\circ 2\theta$ ($d = 2.15$ nm) a distinct peak formation occurred at higher concentrations. A typical critical point of solvent casting is the high requirement of solvent. By use of higher concentrated PAI solutions this demand could be compensated. Thus, the overall amount of solvent remained equal.

3.4 Summary

In this chapter a critical evaluation of PAI-MMT-nanocomposite synthesis via novel approaches of *in situ* polymerization and solvent casting method with two different organo-modified MMT's was provided.

The first part focused on a new strategy of MMT-exfoliation via *in situ* polymerization. It was performed by swelling MMT intergalleries with PCP-blocked MDI and TMA monomers followed by polymerization to PAI within the intergalleries. Successful swelling due to the presence of monomers within the intergalleries and successful exfoliation was verified via XRD-measurements. Experiments with increasing MMT concentration showed a limit for complete exfoliation at 2.0 wt-%. Subsequent computational simulations of equilibrium geometry conducted for blocked MDI showed good correlation to enlargement of MMT's intergallery spacing which supported the thesis of successful swelling. Following SEM analysis of cross-sections indicated in the first instance poor particle distribution but high degree of exfoliation. Subsequent dispersing the sample enabled homogenous distribution of particles within the polymer matrix. FTIR measurements proved successful formation of characteristic amide and imide structures during *in situ* polymerization.

In the second part, preparation of PAI-MMT-nanocomposites via solvent casting method was investigated. It was performed by swelling MMT particles in NMP followed by dropwise addition of PAI solution and dispersing. XRD and SEM analysis showed exfoliated states until clay concentrations of 1.2 wt-% which is assumed to be the percolation threshold of this system. With further increased concentrations, increasing amounts of intercalated MMT particles were observed.

A comparison of both methods to conventional mechanical stirring is shown in Figure 50.

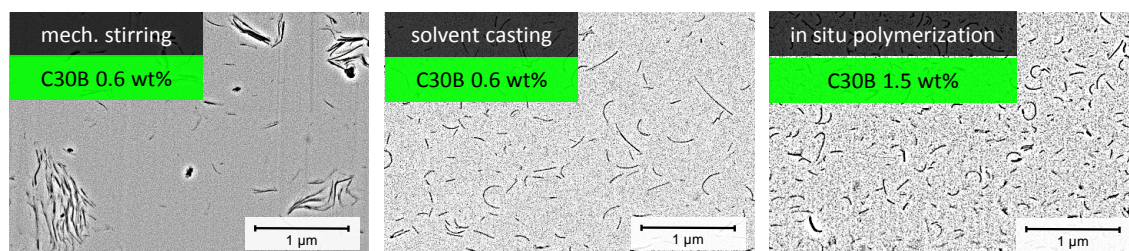


Figure 50: Comparison of PAI-MMT-nanocomposites synthesized via conventional stirring, solvent casting method and *in situ* polymerization.

In comparison to *in situ* polymerization the solvent casting method turned out to be simpler, faster and economically more feasible. A distinct influence of the different organo-modified particles used in this work on the processes of *in situ* polymerization

was not found, but in case of solvent casting slightly higher MMT concentrations than in previous work of *Ranade et al.* ^[131] were obtained. Because of these results, subsequent preparation of nanocomposites will base on PAI-MMT-nanocomposite derived from C30B which are synthesized via the solvent casting method.

Chapter 4: Modification of interphases

4.1 Introduction

The target of modification of interphases is to increase the compatibility of the polymer matrix and nanofillers to avoid agglomerates. In composites, nanoparticles induce changes in polymer structure due to their interfaces. Highly immobilized layers near the particle surface can be introduced via bondings between polymer and nanofiller. In terms of dielectrical properties it is known, that the bound layer affects numerous properties of nanocomposites such as local charge distribution, mobility of polymer chains, chain conformation, molecular weight, chain entanglement density, free volume, crystallinity, crosslink density and trap site density and depth ^[96,97].

These mechanisms are all strongly related to the interaction zone between the polymer matrix and the particle interphase. Based on this fact, the present chapter focuses on changes in properties of chemically bonded exfoliated PAI-MMT nanocomposites.

As introduced in chapter 1.7, trialkoxysilanes are widely used in research and numerous industrial applications as coupling agents. In this connection, ²⁹Si-NMR-spectroscopy is of great interest to acquire further information about the structure of the oligomeric species and products of grafting reactions. The chemical shift of silicon is determined by the chemical nature of their neighbours. These are the number of siloxane bridges attached to a silicon atom. The commonly used notation for these structures are M, D, T, and Q corresponding to one, two, three, and four Si-O bridges, respectively. *Glaser* and *Wilkes* introduced the nomenclature M_i, D_i, T_i, and Q_i. In this context, the index *i* refers

to the number of -O-Si groups bound to the silicon atom of interest^[134]. ^{29}Si -NMR also provides a way to follow the hydrolysis and the condensation reaction of silicon alkoxides. The silane used in this work belongs to the class of trialkoxysilanes and therefore is covered with the nomenclature of T. Following scheme illustrates examples of T_n -structures.

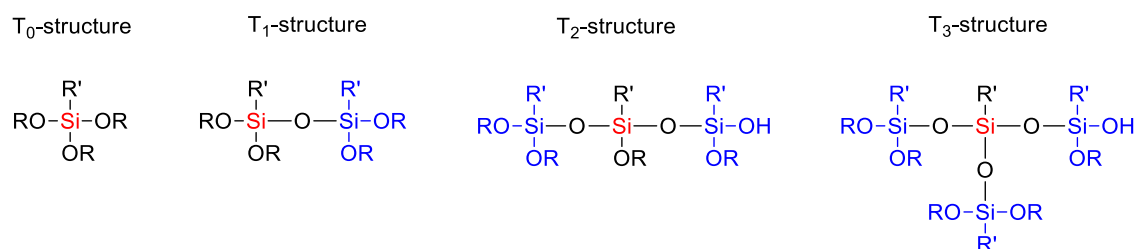


Figure 51: Scheme of possible T-structures of trialkoxysilanes.

The T-structure exhibits only one organic side group Si-R' and the three siloxane bridges can be differentiated between Si-O-Si and Si-OR groups.

Due to its silica network of four Si-O bridges, montmorillonite can be described with Q-structures. In general, the structure of MMT is assigned to Q_3 , because the fourth oxygen (out of plane) is not shared by other silicon atoms and exhibits a hydroxyl group. In case of defects in tetrahedral structure, Q_2 -structures are possible which induces hydroxyl groups into the surface of MMT.

4.2 Experimental

4.2.1 Reagents and materials

Polyamide-imide was synthesized via diisocyanate route with 1,2,4-benzenetricarboxylic acid anhydride (TMA, 97 %, obtained from Sigma-Aldrich) and 4,4'-methylene diisocyanate (MDI, 98 %, obtained from Sigma-Aldrich) in N-methyl pyrrolidone (NMP) as solvent. Methyl tallow bis-2-hydroxyethyl ammonium modified montmorillonite (Cloisite 30B) and neat sodium montmorillonite (Na-MMT) was obtained from Byk Chemie. γ -Aminopropyltriethoxysilane (APTES, 98 %) was obtained from ABCR. HDG zinc-coated steel was obtained from Voestalpine. The reagents and materials used in this study were applied without prior purification.

4.2.2 Synthesis of PAI

TMA (327.98 g, 1.71 mol) and NMP (741.50 g) were added to a 2 L four-necked glass reactor under purging nitrogen gas and heated to 60 °C. The mixture was stirred until TMA was completely dissolved. Then the mixture was cooled down to 40 °C followed by addition of excess MDI (430.08 g, 1.72 mol). The reaction temperature was increased stepwise from 40 to 65, 75, 95 and finally to 130 °C and was kept for 30 min at every step. During the reaction from 80 °C to 130 °C large amounts of CO₂ development were observed. A highly viscous dark red to brown solution of PAI was obtained.

4.2.3 Preparation of composites for determination of percolation threshold

Exfoliated nanocomposites with varying MMT concentration were prepared via solvent casting method with Na-MMT and C30B (Table 5). Organo-modified MMT were mixed with 20.00 g NMP in a vessel and stirred via magnetic stirrer for about 1 h. Subsequently the mixture was placed under a disperser followed by dropwise addition of a solution of 50.00 g polyamide-imide at rotational speed of 400-600 rpm. After complete addition, the composite was dispersed at 1200 rpm for 1 h. Thin films were prepared on zinc-coated steel and dried in an oven at 220 °C for 30 min in order to analyse dielectric behaviour in terms of breakdown strength.

Table 5: Concentrations of PAI-MMT-nanocomposites for determination of percolation threshold.

C MMT/PAI (solid)	m PAI (solution)	m MMT (solid)	C PAI (solution)
[wt-%]	[g]	[g]	[wt-%]
0.0	50.00	0	52.02
0.2	50.00	0.0520	52.02
0.4	50.00	0.1040	52.02
0.6	50.00	0.1561	52.02
0.7	50.00	0.1821	52.02
0.8	50.00	0.2081	52.02
1.0	50.00	0.2601	52.02
3.0	50.00	0.7803	52.02
5.0	50.00	1.3005	52.02

4.2.4 Synthesis of silane modified MMT

Exfoliated PAI-nanocomposites were prepared via solvent casting method from organo-modified C30B and Na-MMT. Because of loss during subsequent ultrafiltration, slight excess of MMT was mixed with 100 g NMP in a vessel. After 1 h of swelling under ultrasonication, excess APTES was added (ratio [wt-%] $\text{APTES/MMT} = 2.0$) followed by overnight reaction at room temperature. At next step APTES which has not covalently reacted with the MMT surface was washed out via ultrafiltration using 20 g NMP twice and a filter with a pore diameter of 100 nm. Samples were dried in an oven at 80 °C until constant mass. A white powder was obtained.

4.2.5 Synthesis of nanocomposites

Synthesis of silane modified exfoliated nanocomposites were prepared from solutions according to 4.2.4 via the solvent casting process. PAI_C30B was prepared following the same procedure but without addition of APTES. The parameters of all samples are summarized in Table 6.

Table 6: Composition of samples for investigation of properties.

sample	m MMT (s) [g]	m PAI (sol.) [g]	c PAI (sol.) [wt-%]	c MMT/PAI (s) [wt-%]	ratio APTES/MMT [wt-%]
PAI	-	-	52.02	-	-
PAI_C30B	0.1561	50.00	52.02	0.6	-
PAI_C30B_APTES	0.1561	50.00	52.02	0.6	2.0

4.2.6 Film preparation

For measurement of dielectric breakdown strength, thin films were coated on cleaned steel substrates and were dried in an oven at 220 °C for 30 min. Applied films were present in the range of 8 to 15 microns dried film thickness.

4.2.7 Characterization

Preparation of cross sections and imaging of particle distribution of MMT in PAI and measurements of film thickness of applied films were conducted via Zeiss Neon 40 Crossbeam and crossbeam-preparation via Canion Ga-FIB. In order to investigate basal spacing of MMT sheets X-ray diffraction measurements were performed with Bruker D5005 (Cu-K α 0.154 nm). XRD measurements were conducted in transmission geometry at angles between 2.5 and 6.0 °2 θ . FTIR spectra measured with Bruker Alpha-P (λ = 633 nm) allowed to investigate the kinetics of covalent bonding due to ring opening reaction at imide groups of PAI. Thermogravimetric analysis (TGA) of treated and untreated MMT as well as PAI-MMT composites was performed on a Mettler-Toledo TGA/SDTA 851e. Samples were heated at a rate of 10 °C/min under a nitrogen flow (20 mL/min). The grafted amount of silane was determined using following equation.

$$mequiv(Silane) = \frac{10^3 W_{200-700}}{(100 - W_{200-700}) \cdot M} \quad (35)$$

Where W is the weight loss between 200 and 700 °C corresponding to silane degradation and M (g/mol) is the molecular weight of the grafted silane molecules [135].

Elemental analysis was conducted on an Elementar Vario Micro Cube to confirm silane amount determined via TGA. Solid-state ^{29}Si magic angle spinning NMR spectra were recorded on a Bruker Avance 300 spectrometer (300 MHz) at a spinning rate of 2.4 kHz. Measurements of dielectric breakdown strength were conducted via self-crafted experimental setup which is shown in the following Figure 52.

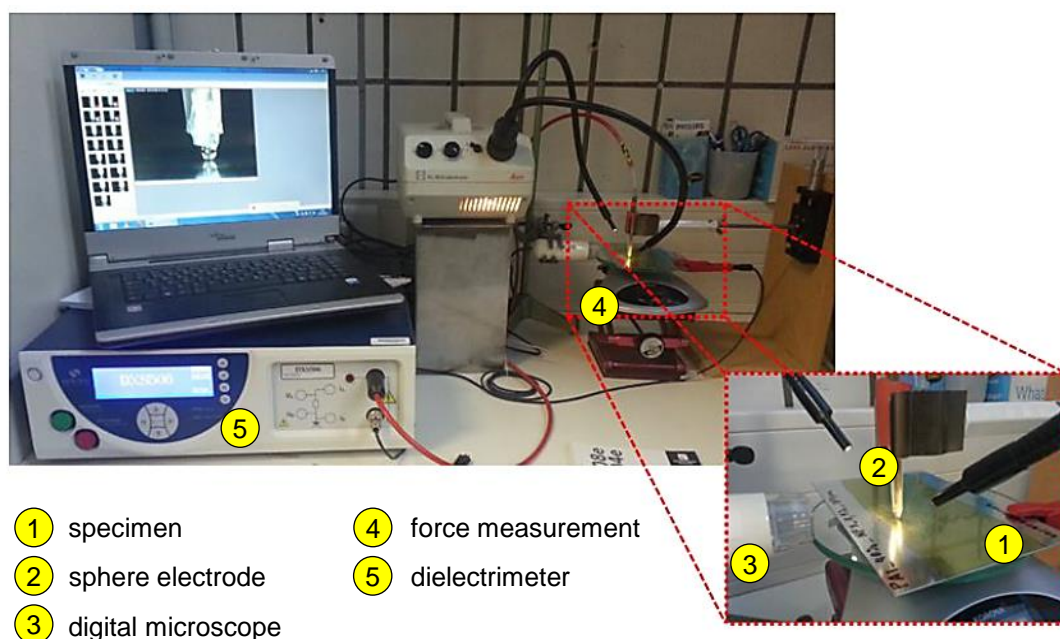


Figure 52: Experimental setup for measurements of dielectric breakdown strength.

A sphere-plate-geometry was chosen where the specimen (1) was used as counter electrode and a sphere as electrode (2). The approach of the sphere electrode was controlled by a microscope camera (3) and a balance (4) for touch down measurement. A voltage ramp with a rate of 0.1 kV/s was applied. Direct increase until breakdown was used, which corresponds to the short-time (rapid-rise) test [IEC98]. The application of voltage and detection of electrical breakdown was conducted with a Sefelec DXS 506 dielectrimer (5). The resulting dielectric breakdown strength (DBS) was calculated using following equation.

$$DBS = 0.9 \frac{V(2r + d)}{2rd} \quad (36)$$

Where V is the Voltage determined at point of dielectric breakdown, r the radius of sphere electrode (3.2 mm) and d the film thickness which was subsequently measured via SEM

at cross-sections in the area of measured points. The expected values of DBS were determined using Weibull statistical analysis.

4.3 Results and discussion

In the present work modification of MMT with APTES was used for several reasons. First of all, in terms of self-condensation and grafting kinetics, APTES is widely explored ^[136–139]. Secondly, it provides an amino function which can be used to chemically bond to PAI by ring opening reaction under formation of an amide group ^[140,141]. A reaction scheme of the desired bonding strategy between PAI and APTES-modified MMT is shown in the following figure.

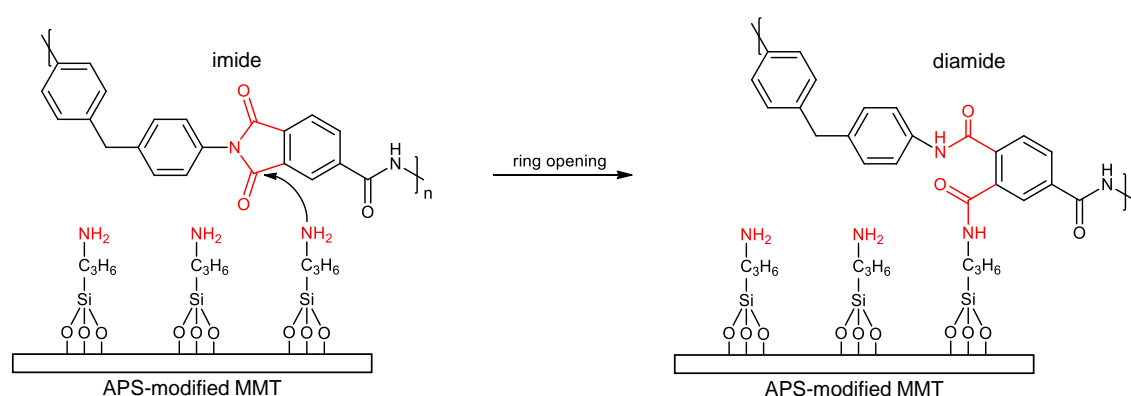


Figure 53: Reaction scheme of strategy to bond silane modified MMT covalently to PAI molecules via imide ring opening.

The following chapters focus on the quantification and qualification of successful grafting of APTES to MMT, investigations on the kinetics of the ring opening reaction.

4.3.1 Determination of dielectric percolation threshold

Initially, dielectric breakdown strength depending on the MMT content was investigated in order to determine the dielectric percolation threshold. This threshold represents the maximum concentration of MMT which can be realized without losing the dielectrical character of the resulting composite.

A scheme about the correlation of particle concentration and nearest neighbour distance is shown in Figure 54. As described in 1.6.6, the multi-core model of Tanaka shows that at the concentration where cores overlap, the electrical percolation threshold is reached resulting in a breakdown of the dielectric. The target of following experiment is the determination of threshold which is needed for subsequent formulation. Figure 55 shows the results of the dielectric breakdown strength depending on the MMT content.

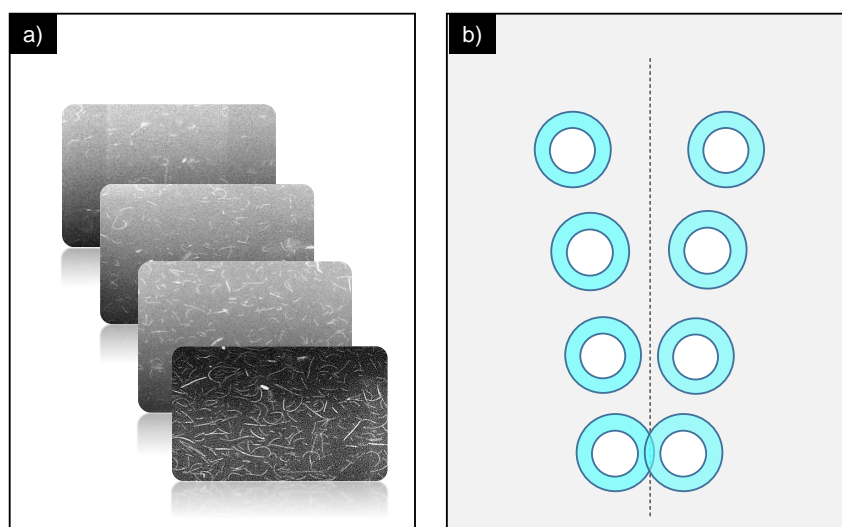


Figure 54: Scheme of overlapping regions of particles due to reaching of percolation threshold.

The initial measured strength of pure PAI was 311 kV/mm. In the first instance, an increase of DBS with increasing MMT concentration was observed. The maximum of 336 kV/mm was reached at 0.6 wt-% MMT which hence represents the electrical percolation threshold.

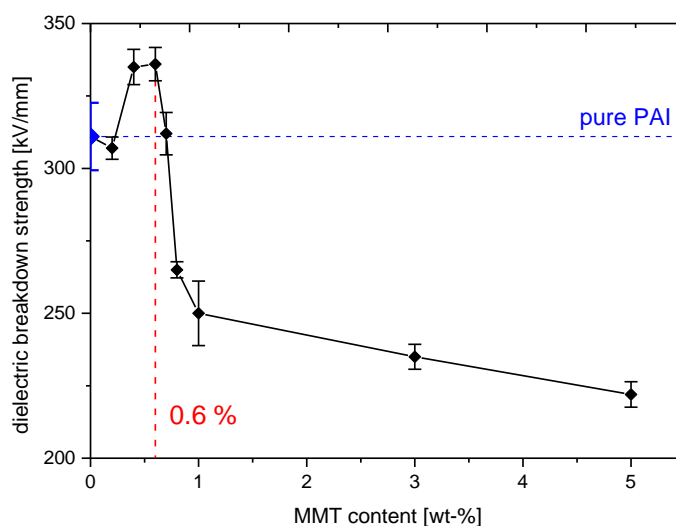


Figure 55: Determination of dielectric percolation threshold via measurement of DBS with increasing content of MMT (C30B) in PAI.

With further increasing concentration a rapid slope in dielectrical behaviour was observed. To investigate the effect of silane modified PAI-MMT-nanocomposites, subsequent formulations of composites are based on the concentration of 0.6 wt-%. This concentration was therefore determined as the electrical percolation threshold.

4.3.2 Qualification of grafting

Qualitative evidence of grafting of APTES to MMT was provided by solid-state ^{29}Si -NMR-spectroscopy. The spectra of pure and modified Na-MMT and C30B, respectively, are shown in Figure 56. For untreated samples two resonances were found at -92 ppm and a peak shoulder at -84 ppm. This corresponds to Q_3 trioxo coordinated framework silicon and Q_2 sites attributed to isolated silanol groups present at the silicate surface respectively [142]. The grafting was evidenced by the decrease of relative intensity of the Q_2 signal due to reaction of APTES with SiOH groups of clay sheets. Furthermore, appearance of a broad signal between -50 and -70 ppm was observed which can be assigned to T_2 and T_3 silicate units derived from grafting process.

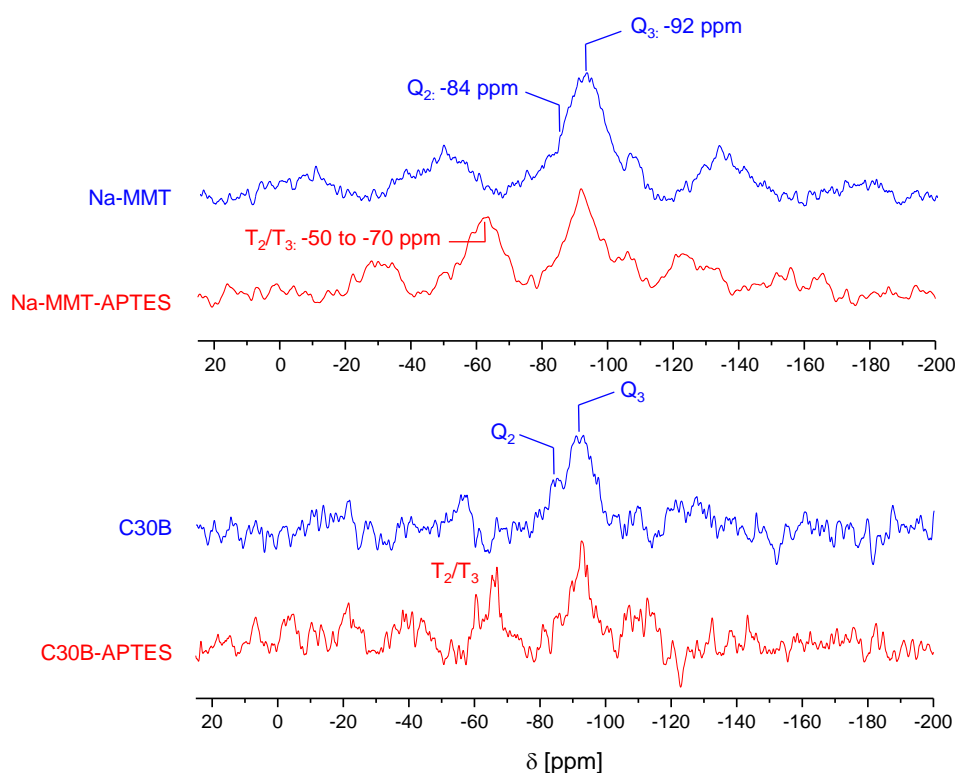


Figure 56: ^{29}Si -NMR-spectra of Na-MMT (top) and C30B (bottom) before (blue) and after silane modification (red).

The covalent bonding of PAI to MMT by means of APTES was investigated via FTIR measurements. The formation of amide was observed via decrease of antisymmetric $\text{C}=\text{O}$ vibration in imide rings located at 1780 cm^{-1} which indicated successful grafting of APTES to PAI molecules via imide ring opening reaction. The yield of this reaction over time was tracked by peak integration. The results are shown in Figure 57. Two experiments were conducted. First of all, APTES was added to PAI-solution in order to

investigate the reaction kinetics without presence of MMT. Samples at certain time intervals were taken and measured immediately via FTIR. After about 300 min of reaction time the maximum yield of about 48 % was reached. At the second experiment, MMT was silane modified according to chapter 4.2.4 with a MMT-concentration of 0.6 wt-% and added to the PAI solution under stirring.

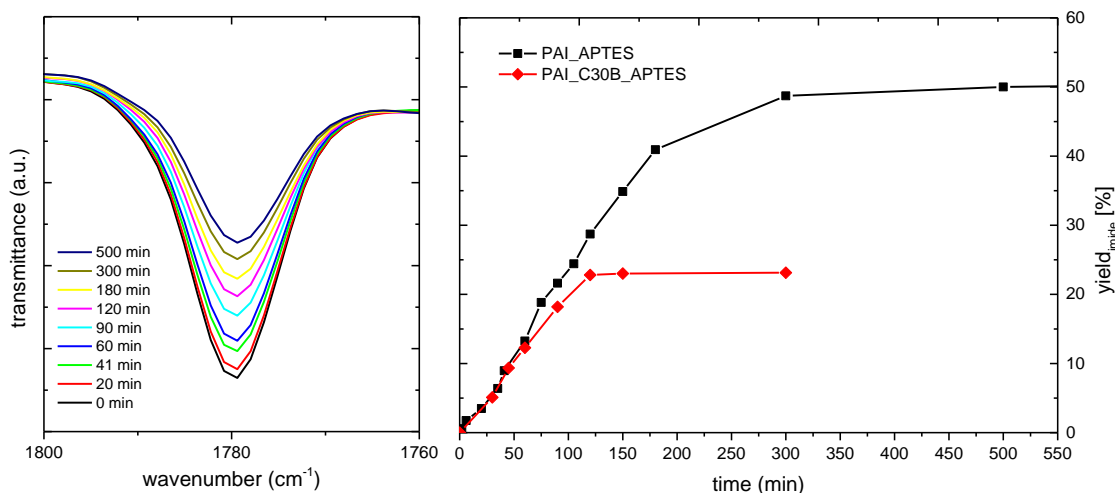


Figure 57: FTIR spectra of antisymmetric C=O vibration at 1780 cm^{-1} (left) and plot of yield over time of imide ring opening (right).

The results showed a rapid yield of reaction until 120 min at which about 23 % of imide rings were converted to amide bonds. Derived from these results, following sample preparation of PAI_C30B_APTES was conducted using the determined reaction time for maximum yield of at least 2 h.

4.3.3 Quantification of grafting

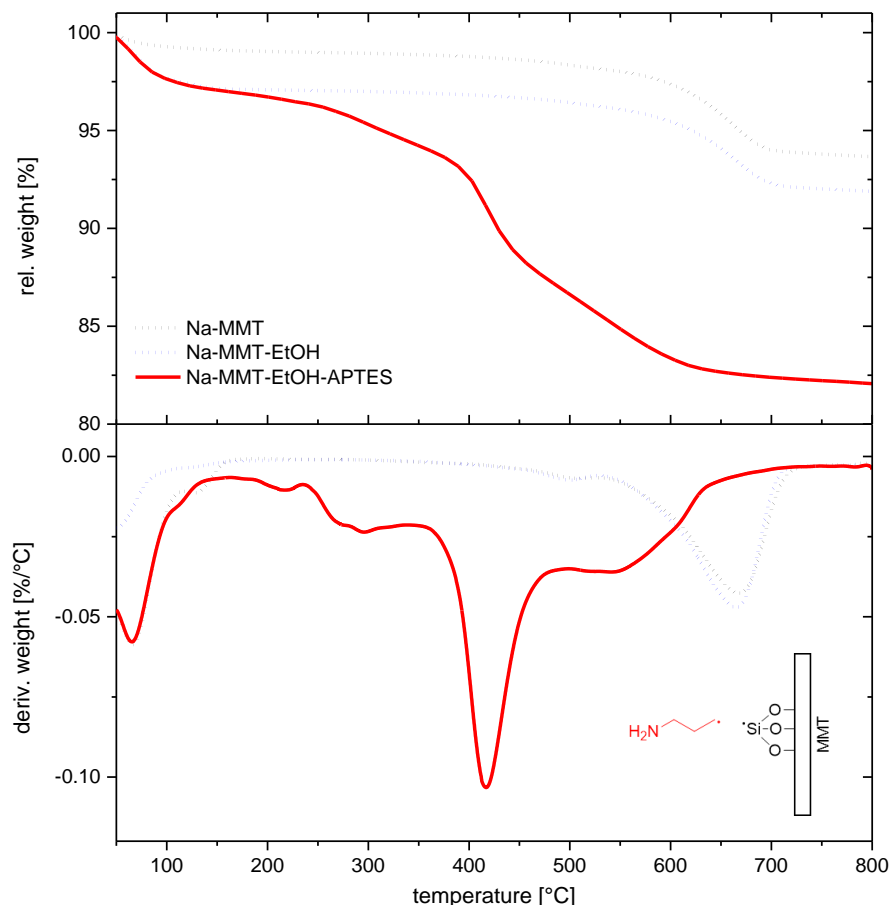
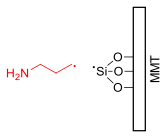
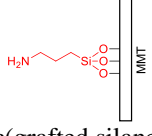


Figure 58: TGA plot (top) of Na-MMT (black) EtOH washed Na-MMT (blue) and Na-MMT after silane treatment (red). Below curves show derivative plot (DTG).

In general, thermal degradation of nanoscale organic-inorganic hybrid materials is a complex process. Initially, to qualify organic decomposition processes, the general characteristics of silane modified MMT were investigated at pristine Na-MMT. In contrast to organically modified MMT, Na-MMT doesn't exhibit the superposition originated from decomposition processes of the organic intergallery ions. First of all, this enabled to observe the decomposition and secondly to quantify the amount of bonded silane. The results are shown in Figure 58. At first measurements, the influence of the purification step via ultrafiltration described in chapter 4.2.4 was investigated. No significant difference were observed. The DTG-plot looks similar. Both samples showed an initial peak around 100 °C which is due to evaporation of remained solvent and the typical peak at 650 °C indicating the dehydroxylation of MMT. After silane modification several new overlapping peaks in range of 200-700 °C with a maximum around 415 °C

were observed. These peaks are assumed to be related to decomposition of aminopropyl-group from APTES. The disappearance of the dehydroxylation peak of MMT can be explained by loss of hydroxyl groups and indicates successful grafting reaction of APTES. Subsequently, mass loss was determined by integration of the DTG-curve between 200 °C and 700 °C. Because the mass loss determined via DTGA is only due to the aminopropyl fragment, the overall amount of grafted silane on MMT was calculated. The results were verified by elemental analysis.

Table 7: Results of Elemental and Thermogravimetric Analyses of silane modified MMT. (a) Weight loss between 200-700 °C. (b) Overall amount of grafted silane calculated from (a). (c) Determined using eq. 1. (d) Calculated from content of nitrogen. (e) Analogous to (b).

	 c(silane fragment) [wt-%]	 c(grafted silane) [wt-%]	mequiv silane [mmol/g]
thermogravimetric analysis	12.2 ^a	28.2 ^b	2.39 ^c
elemental analysis	12.0 ^d	28.6 ^e	2.36 ^c

In Table 7, the grafted amount determined by TGA analysis is in very good agreement with the silane content determined by elemental analysis. The content of aminopropyl fragments for TGA was 12.2 wt-% and for elemental analysis 12.0 wt-% as well as 28.2 wt-% and 28.6 wt-% for overall amount of grafted silane. This result implied that because of the large amount of silane could not only be present at clay edges but also on faces. It might be explained by the natural character of the MMT applied. Previous measurements of ²⁹Si-NMR-spectroscopy showed that this MMT is fairly amorphous indicating defects in its crystal lattice which would result in hydroxyl groups located in MMT's faces. Following XRD-measurements were conducted in order to verify this process which was estimated to result in enlargement of interlayer distance of MMT due to intercalation.

Thermal decomposition of the organophilic and silane modified MMT was investigated via TGA. It was compared to pristine C30B and C30B which was treated by ultrafiltration with NMP as solvent. This experiment was designed to qualify the grafting of APTES to organo-modified C30B analogously to Na-MMT. The results are shown in Figure 59. As

can be seen, C30B decomposition consists of different regions. Briefly, release of absorbed water and gaseous species occurs below 100 °C.

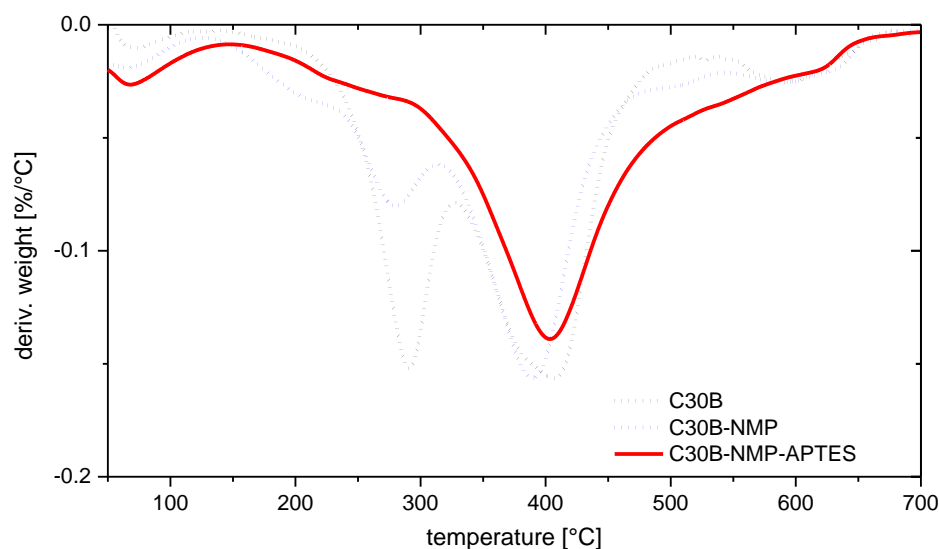


Figure 59: DTG plot of C30B (black) NMP washed C30B (blue) and C30B after silane treatment (red).

Organic intergallery molecules decompose depending on their sheet-location (intergallery or at particle surfaces) in the range from 200 to 500 °C. The first peak near 300 °C is assumed to derive from molecules which are loose physisorbed for example at clay edges. After purification (C30B_NMP), via ultrafiltration with NMP as solvent, this peak significantly decreased. Subsequent silane modification (C30B_NMP_APTES) led to further decrease of this peak indicating that during the grafting process further loose physisorbed intercalation molecules are replaced by APTES. The second peak at 400 °C derives from stronger bonded intergallery counter ions. In contrast to pristine Na-MMT this peak overlaps the estimated silane peak maximum. Only a peak broadening until 600 °C is evidence of successful silane grafting. Due to presence of multiple overlapped peaks in the range of the estimated silane decomposition, quantification analogously to Na-MMT could not be provided. Following XRD-measurements were conducted in order to verify the process of APTES grafting which was estimated to result in enlargement of interlayer distance of MMT due to intercalation.

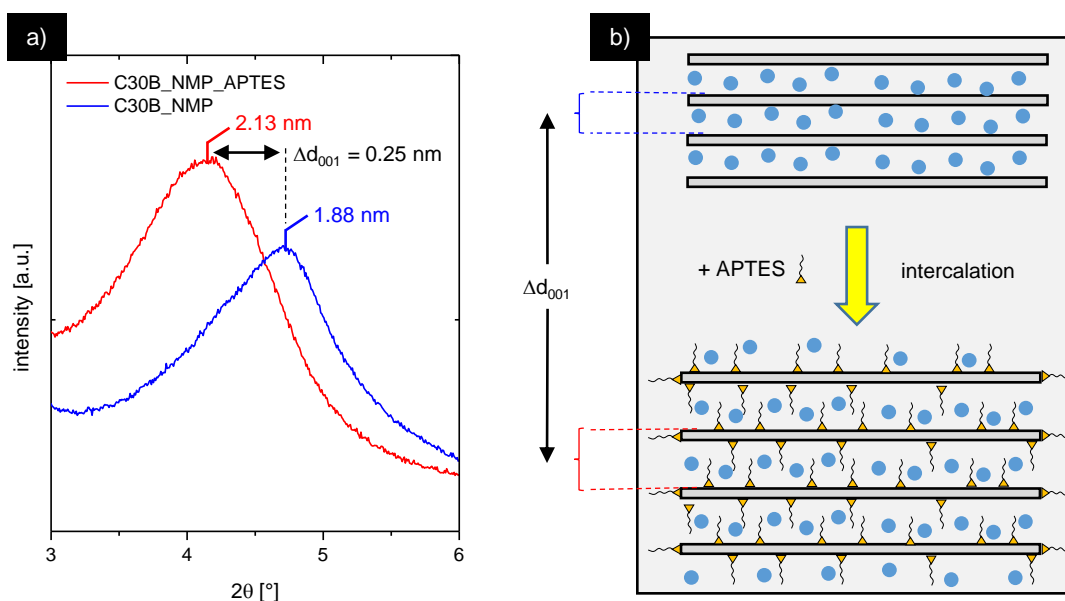


Figure 60: XRD pattern of NMP washed C30B (blue) and NMP washed C30B treated with APTES (red).

Figure 60 (a) shows XRD-patterns of APTES modified C30B which was subsequently purified via ultrafiltration in NMP in order to remove excess silane. Also, XRD-pattern of similar processed C30B are shown. Results indicate that during this process, the APTES molecules were intercalated and grafted to interlayer surface silanol groups. The basal spacing of the APTES-MMT increased from 1.89 nm to 2.13 nm which corresponds to an interlayer expansion of 0.25 nm. This implies that the APTES molecules indeed intercalate into intergalleries of MMT and therefore are able to graft into MMT's faces.

4.4 Summary

This chapter focused on modification of MMT-surfaces with APTES in order to provide a functional group which is able to graft to the polymer matrix covalently. This group was chosen to be an amine. The strategy was to enable the grafting reaction via imide ring opening reaction under formation of an amide link.

Initially, DBS-measurements on composites with varying MMT concentration were conducted in order to determine the electrical percolation threshold. This threshold was very important because it represents the maximum concentration of MMT which can be realized without losing the dielectrical character of the resulting composite. It was reached at a MMT concentration of 0.6 wt-%.

The success of grafting reaction of APTES to MMT was evidenced via ^{29}Si -NMR-measurements and the grafting reaction to the polymer matrix via imide ring opening was investigated using FTIR measurements. It could be shown that the silane modification converted about 23 % of imide rings to amide structures after synthesis with PAI. This indicates a high coverage of APTES on MMT. Results of XRD-measurements indicated that APTES molecules were intercalated and grafted to interlayer surface silanol groups.

Chapter 5: Characterization of nanocomposites

5.1 Introduction

In the previous chapter several approaches ensured successful preparation of exfoliated PAI-MMT-nanocomposites and PAI-MMT-nanocomposites with silane modified MMT which is also covalently bonded to the polymer matrix. This chapter focuses on investigations on how this modification affects properties like dielectric breakdown strength, thermomechanical and mechanical properties. It was therefore compared to the properties of pure PAI and PAI_C30B which was conventionally filled with exfoliated MMT.

5.1.1 Flow induced particle alignment

In a previous work indications for a potential alignment of MMT-particles in polyamide-imide as continuous phase were provided ^[143]. A shear gradient was applied to the composite during film preparation via bar applicator. The basic principle of alignment is illustrated in Figure 61. At the first stage, particles are present with isotropic phase behaviour. In this stage no distinct particle orientation could be observed. At the next stage, a shear gradient was applied during film preparation. Because of their lamellar character and the high aspect ratio of about 200 to 500, particles begin to rotate to the

plane of lamellar flow field until all particles are completely aligned. This is shown in the last stage of the scheme.

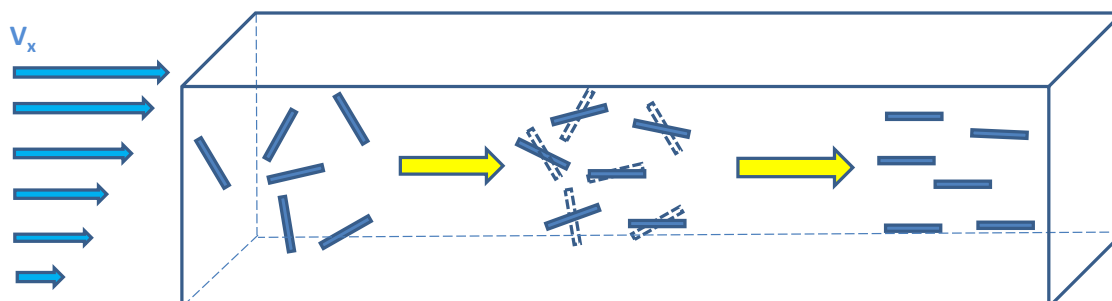


Figure 61: Scheme of flow induced particle (blue sheets) alignment during layer application. An Initial isotropic phase behavior gets aligned and builds anisotropic phases after application of a lamellar flow field ^[143].

Afterwards rheological experiments were conducted in order to verify the postulated process. The results are shown in Figure 62. Initially, the viscosity of a pure PAI solution over time was measured. It could be observed that the viscosity reached a plateau after short time. At the beginning phase of the measurement the composite of PAI and MMT showed a different behaviour. Before a distinct plateau of viscosity was reached, a phase was observed where the viscosity went beyond the following constant values. This phase could be assigned to the stage where MMT particles rotate during alignment due to the lamellar flow field. After this effect, like pure PAI solution, the same behaviour of constant viscosity occurred. This indicated complete alignment of particles. Derived from these results, orientation times as function of the shear stress applied were calculated.

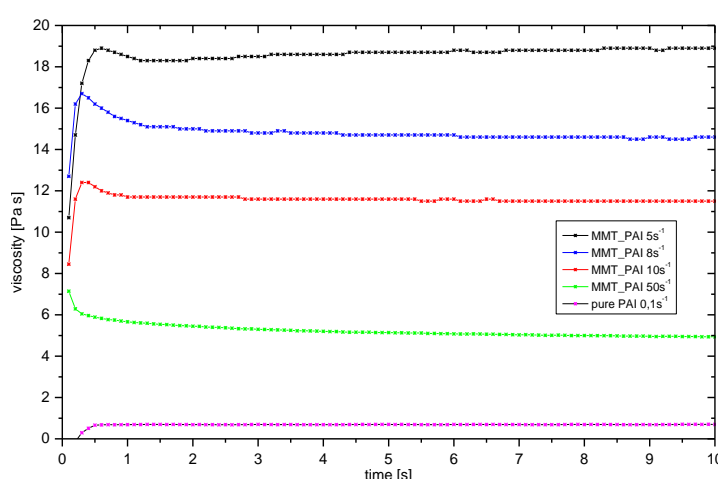


Figure 62: Rheological experiments of viscosity versus time of MMT filled PAI and pure PAI (purple) as reference with varying shear rates of 5 s^{-1} (black) , 8 s^{-1} (blue), 10 s^{-1} (red) and 50 s^{-1} (green) ^[143].

Subsequently, FIB-SEM-nanotomographies of composites were conducted to verify whether the aligned particle structure maintained during the drying process of film formation.

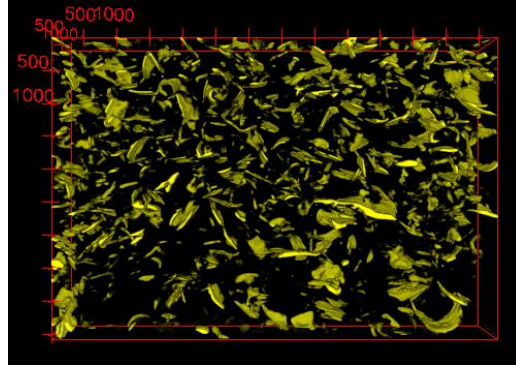


Figure 63: 3D-reconstruction of MMT particles in PAI via 3D-FIB-SEM-nanotomography [143].

An example for particle distribution investigated via FIB-SEM-nanotomography is given in Figure 63. It shows a representative 3D-reconstructed model of MMT-orientation achieved via FIB-SEM-nanotomography. Based on this data, two dimensional data could be achieved in order to investigate orientation of particles.

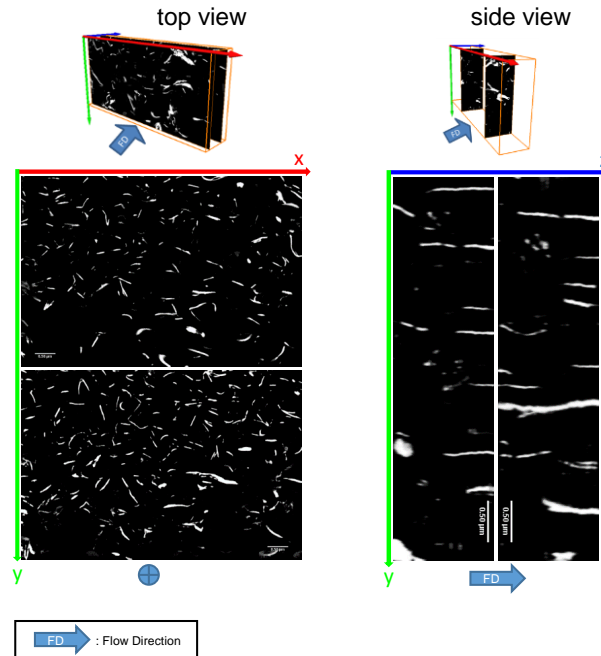


Figure 64: Analysis of particle alignment via FIB-SEM-nanotomography. The top view shows particle distribution at two cross-sections (left side). The side view was calculated from several top view images to allow investigation of particle alignment in flow direction (right side) [143].

An example of this analysis is shown in Figure 64. The SEM-images on the left side show selected images where the particle distribution in flow direction was investigated. Both images show good dispersed behaviour. The images on the right side confirmed particle alignment in flow direction of application which was observed at rheological analyses.

5.1.2 Changes in properties due to nanoparticles and silane modification

As mentioned before, the key to improved properties is to increase the compatibility of matrix polymer and nanofillers to avoid agglomerates. In terms of dielectrical properties, several publications showed the potential of layered silicate filled nanocomposites with varying polymer matrices [95,144–146]. However, no comparable results are present for polyamide-imide and montmorillonite. *Roy et al.* concluded that covalent bonding of vinylsilane functionalized SiO_2 -nanoparticles and CaCO_3 filled cross-linked polyethylene (XLPE) was one of the keys to an improved voltage endurance [102]. They pointed out, that bonding of nanofillers can be engineered to provide a way to tailor material properties in a desired direction. The coverage of surface modification is a key factor in this process.

In terms of breakdown mechanism, *Imai et al.* reported about the effect of nanoscale layered silicate on the propagation of electrical treeing phenomena [147]. They assumed that an increase in encountering frequency by nano- and micro-filler mixture prevents treeing from propagating efficiently. This resulted in an improved insulation breakdown strength. A scheme of the postulated underlying mechanism is shown in Figure 65.

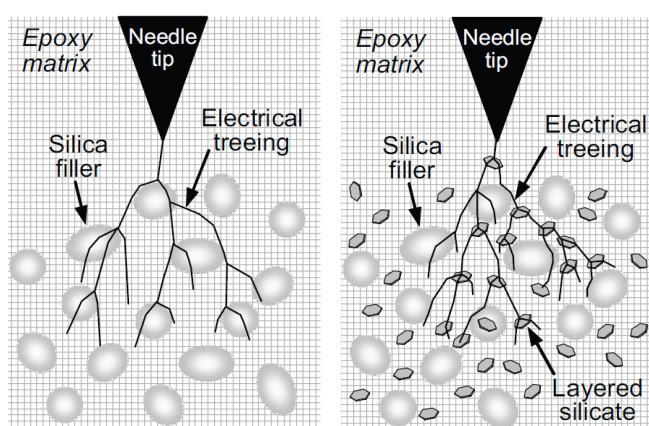


Figure 65: Estimated model for effect of the layered silicate and silica filler mixture (nano- and micro-filler mixture) [147].

5.2 Experimental

5.2.1 Film preparation

For measurement of dielectric breakdown strength, thin films were coated on cleaned steel substrates and were dried in an oven at 220 °C for 30 min. Applied films were present in the range of 8 to 15 microns dried film thickness.

In order to investigate the mechanical properties of films, samples were coated on a glass substrate, dried analogously to the preparation for shear strength measurements and mechanically removed from the glass surface. Resulting dry film exhibited thicknesses around 60 microns.

5.2.2 Characterization

Preparation of cross sections and imaging of particle distribution of MMT in PAI were conducted via Zeiss Neon 40 Crossbeam and crossbeam-preparation via Canion Ga-FIB. Energy dispersive X-ray spectroscopy (EDX) was performed with an Ultra Dry Silicon Drift X-ray detector from Thermo Scientific.

Dielectric Breakdown experiments were conducted with a Sefelec DXS 506 and a sphere/plate geometry of electrodes. A voltage ramp with a rate of 0.1 kV/s was applied. Direct increase until breakdown was used, which corresponds to the short-time (rapid-rise) test [IEC98]. The resulting dielectric breakdown strength (DBS) was calculated using following equation.

$$DBS = 0.9 \frac{V(2r + d)}{2rd} \quad (37)$$

Where V is the Voltage determined at point of dielectric breakdown, r the radius of sphere electrode (3.2 mm) and d the film thickness which was subsequently measured via SEM at cross-sections in the area of measured points. The expected value of DBS was determined using Weibull statistical analysis.

Measurements of tensile strength were conducted at thin films on a Zwick Z020 at a testing speed of 10 mm/min. Sample dimensions were derived from DIN EN ISO 527-3.

Measurements of film thickness of applied films were conducted via Zeiss Neon 40. Thermogravimetric analysis (TGA) of composites and neat PAI was performed on a Mettler-Toledo TGA/SDTA 851e. Samples were heated at a rate of 10 °C/min under a nitrogen flow (20 mL/min). For determination of glass transition temperatures differential scanning calorimetry analysis was conducted on a Netzsch DSC 214 Polyma. Samples were heated at a rate of 10 °C/min under a nitrogen flow (40 mL/min).

5.3 Results and discussion

5.3.1 Dielectric breakdown strength

Dielectric breakdown strength (DBS) measurements of PAI, PAI_C30B and PAI_C30B_APTES were conducted and evaluated using Weibull statistical analysis. The results are shown in Figure 66.

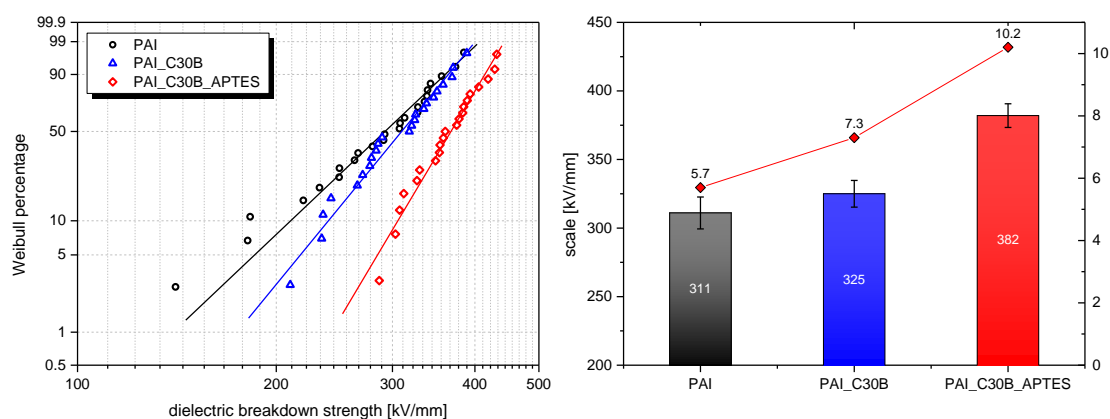


Figure 66: Left plot shows Weibull statistical analysis of DBS for pure PAI (black), PAI_C30B (blue) and PAI_C30B_APTES (red). Resulting scale and shape parameters determined from Weibull analyses are provided in the right plot.

Unfilled PAI exhibits the poorest dielectric performance with a DBS of 311 kV/mm and shape factor of 5.7. PAI filled with exfoliated MMT at the same concentration resulted in an increased DBS of 325 kV/mm and a shape factor of 7.3. The best performance and significant enhanced DBS was observed for PAI with exfoliated and covalently bonded MMT. DBS increased to 382 kV/mm and a shape factor of 10.2. This corresponds to an overall enhancement for PAI_C30B_APTES in DBS of about 22.8 % and 78.9 % in shape factor compared to pure unmodified PAI.

The reason for the enhanced DBS could be related to several possible effects. First of all, an effect of the induced large polymer-particle-interphase due to the presence of exfoliated MMT could be observed in the case of PAI_C30B. In several publications which were mentioned in the introduction it was reported, that through these interphases local conductivity regions can be created around the nanofillers. These regions reduce charge accumulation, also known as space charge, and thus help in controlling electric field distribution and dielectric breakdown strength. This local conductivity region, which

can be described as quasi-conductive region, is formed around nanoparticles that overlap partially and allow charge dissipation [100–102]. Furthermore it is common, that interphases act as charge traps [97,99]. In comparison to pure PAI the DBS increased by 4.5 %. The more significant improvement was reached via bonding of MMT to PAI via APTES. This should cause a decrease in free volume at the PAI-MMT-interphase which is also known to be relevant for the breakdown behaviour. Another effect could be related to a higher thermal resistance and is investigated in the next chapter.

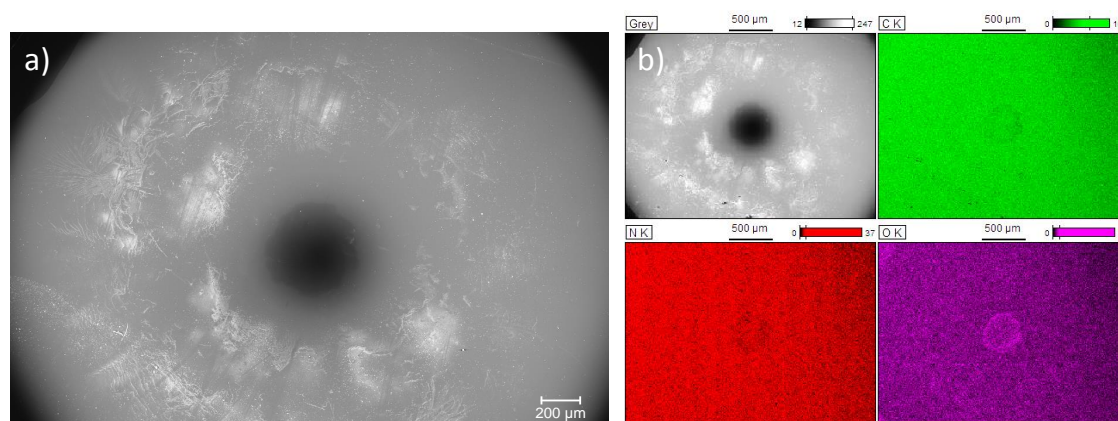


Figure 67: (a) SEM image of an area which was treated by high voltage where the sphere electrode was located. (b) Elemental mapping of carbon (green), nitrogen (red) and oxygen (purple) at treated point performed via EDX-analysis.

In order to investigate the origin of the underlying electrical breakdown mechanism, samples were treated with high constant voltage for several minutes. The voltage applied was chosen to be slightly below the dielectric breakdown strength of the material. In contrast to the DBS measurements before, at this method treatment of samples was stopped before the electrical breakdown occurred. This enabled studies of underlying mechanisms of the breakdown development.

In the first instance, PAI was chosen to investigate possible changes in chemical composition. After treatment with high voltage a distinct dark area around the electrode's contact point was observed. This point was surrounded by concentric areas of damaged material. An example is provided in Figure 67 (a). Subsequent elemental mapping via EDX-Analysis was performed. The results are shown in Figure 67 (b). In relation to the surrounding area, the dark point exhibits a significant decrease in carbon and nitrogen content, respectively, while the oxygen content is higher. This correlates with an oxidation process of PAI which could lead to a thermal breakdown behaviour. The EDX-analysis for PAI_C30B and PAI_C30B_APTES showed the same result.

Following investigations therefore focused on the microscopic picture of injury to clarify whether thermal breakdown is the only underlying mechanism. The results are shown in Figure 68. SEM images of PAI, PAI_C30B and PAI_C30B_APTES were taken at the same level of magnification.

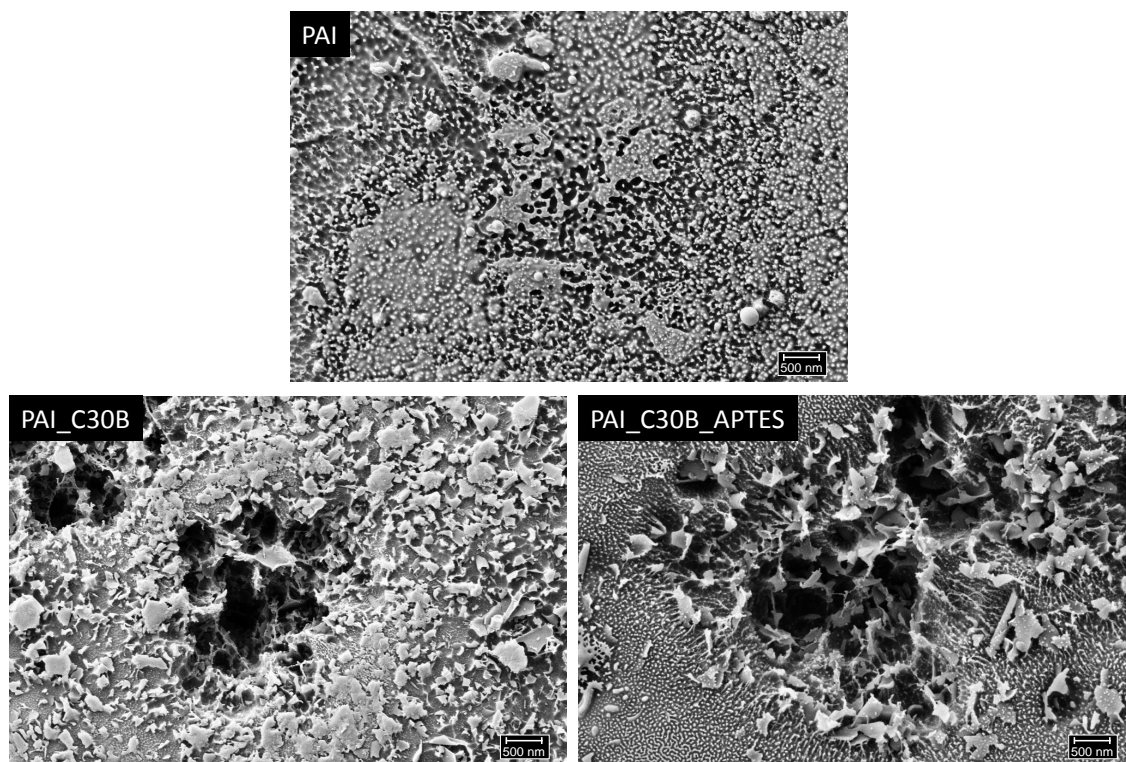


Figure 68: SEM-images of PAI, PAI_C30B and PAI_C30B_APTES after treatment with constant high voltage below DBS. Investigation of characteristics in surface injury.

In case of PAI a melting like surface behaviour was observed but no injury into the film. At PAI_C30B and PAI_C30B_APTES distinct punctual damage areas were observed. At both samples it can be assumed that nanoscaled MMT particles interact with the applied electrical field resulting in the formation of treeing-like structures.

Figure 69 shows a cross-section at one of this points. It was prepared via focused ion beam. The image was taken via SE2-detector. The inset image provides information about the MMT distribution in PAI matrix. It was obtained via FFT (Fast Fourier Transformation) bandpass filter operation applied to the original SE2-image of the cross-section. The cross-sectional image in Figure 69 (a) verifies the observations made of previous discussed top view images. The structure of injury correlates with the particle size dimension of embedded MMT which is shown in Figure 69 (b). Thus, it can be confirmed that the voltage induced propagation of injury structure interacts with single

MMT particles. The result is a nanoscaled treeing-like propagating structure through the PAI-MMT-nanocomposite. It can further be observed that it is likely that several tracks recombine. This is followed by larger microscaled injury structures which were obtained after dielectric breakdown.

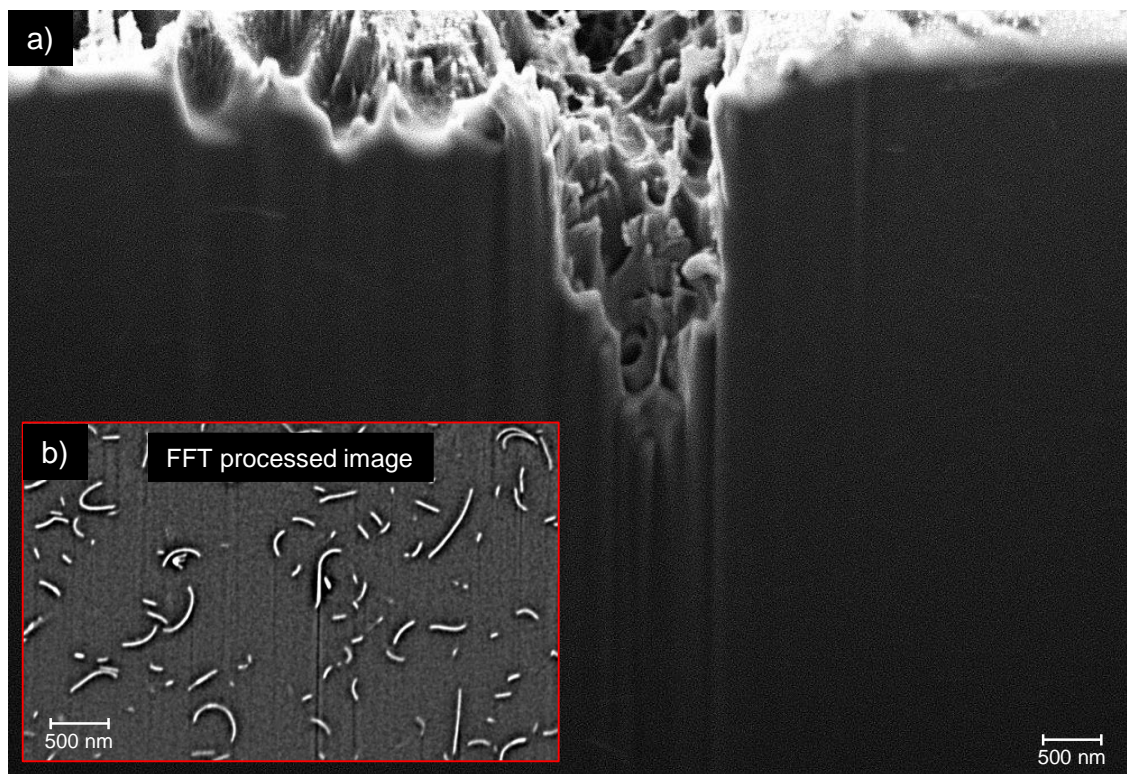


Figure 69: (a) SEM image of cross-section of point of film beginning injury derived from constant voltage treatment taken with SE2-detector. The inset image (b) was obtained from a FFT bandpass filter in order to visualize MMT particle distribution within the composite film.

Based on results, it is shown that pure PAI developed injury structures which are likely derived from the thermal breakdown mechanism. Embedding exfoliated nanoscaled MMT particles under formation of a nanocomposite resulted in a mixed breakdown process of thermal breakdown and one which can be described with the principles of treeing and tracking. To clarify the influence of MMT in the nanocomposite on its thermal strength, the following chapter focuses on investigation of resulting decomposition temperatures.

5.3.2 Thermal properties

Polyamide-imide is widely known for its outstanding thermal properties. The question of this study was, if these properties could further be improved through silane modified MMT nanocomposites. In order to clarify the influence of the silane modification on the thermal strength, TGA measurements were conducted.

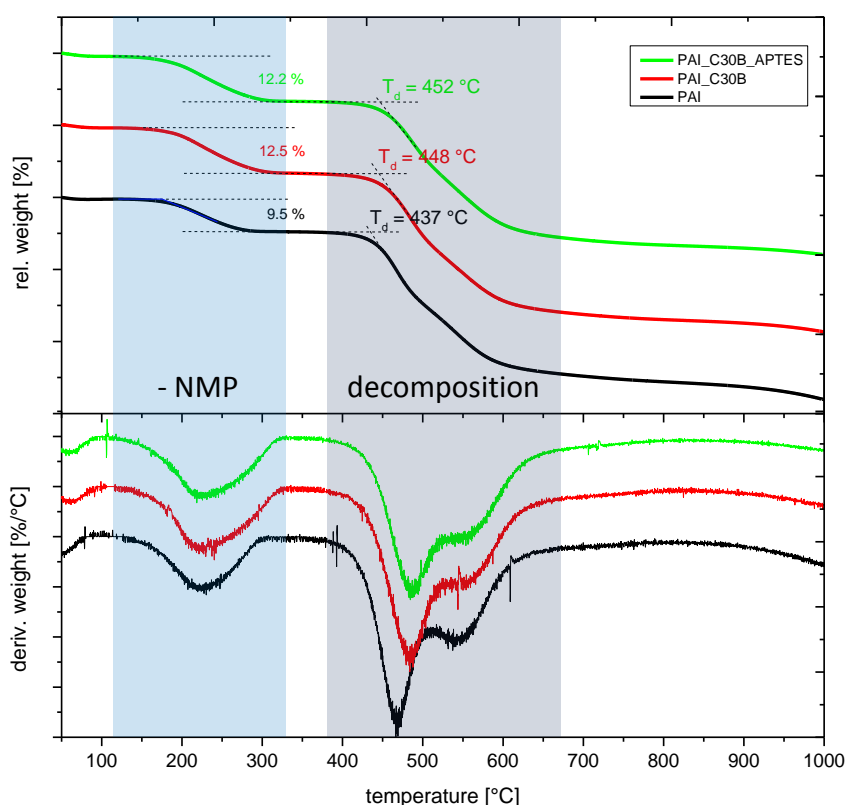


Figure 70: Decomposition temperatures of pure PAI (black), PAI_C30B (red) and PAI_C30B_APTES (green) determined via TGA.

PAI_C30B_APTES was compared to pure PAI and PAI_C30B. The results are shown in Figure 70. All samples exhibit an initial weight loss at about 200 °C which is due to NMP evaporation. The following weight loss indicates the decomposition of the system and the onset decomposition temperature was determined. Pure PAI showed a decomposition temperature of 437 °C, PAI_C30B 448 °C and PAI_C30B_APTES increased to 452 °C. This result was not estimated. As described in chapter 4, the covalent bonding via APTES was conducted through an imide ring opening reaction. As the imide group is known to be responsible for the excellent thermal properties of polyamide-imide, decomposition temperature was estimated to decrease. Results showed the opposite behaviour with an enhancement of 15°C compared to pure PAI. Because this is in the same area as

PAI_C30B the effect is assumed to originate from the induced polymer-MMT-interphases.

Besides thermal decomposition behaviour of samples, information about temperature induced phase transitions are important for subsequent applications. Measurements on same samples via differential scanning calorimetry (DSC) were conducted. This allowed investigation of physical changes like glass transition, melting points and the presence of crystallization. Figure 71 provides results of the samples PAI (black), PAI_C30B (red) and PAI_C30B_APTES (blue). Three consecutive segments of each sample were measured under constant heat rate of 10 °C/min. Initial heating curves are shown in Figure 71 (a) followed by a cooling phase in Figure 71 (b) and a second heating in Figure 71 (c).

At first heating curves in (a) the first endothermal peak observed at all samples from room temperature to 140 °C indicates evaporation of moisture. PAI_C30B_APTES exhibited a distinct glass transition at 246 °C. Following peaks for PAI and PAI_C30B are strongly superimposed. It can be assumed that this broad peak is related to advancing PAI polymer synthesis due to imidization reaction and evaporation of the solvent NMP. This assumption correlates with the results of the cooling phase (b). No corresponding exothermal process were observed and therefore an irreversible process due to chemical reaction or solvent evaporation is likely. However, in cooling phase glass transition temperatures for all samples could be determined. For PAI a T_g of 298 °C, PAI_C30B a T_g of 285 °C and for PAI_C30B_APTES a T_g of 282 °C were measured. The results of second heating in (c) agreed with prior determined values.

The glass transition temperatures were determined for PAI, PAI_C30B and PAI_C30B by 287, 289 and 281 °C, respectively. The superimposed peaks observed in (a) were not present. This implies full evaporation of NMP and absence of advancing PAI conversion.

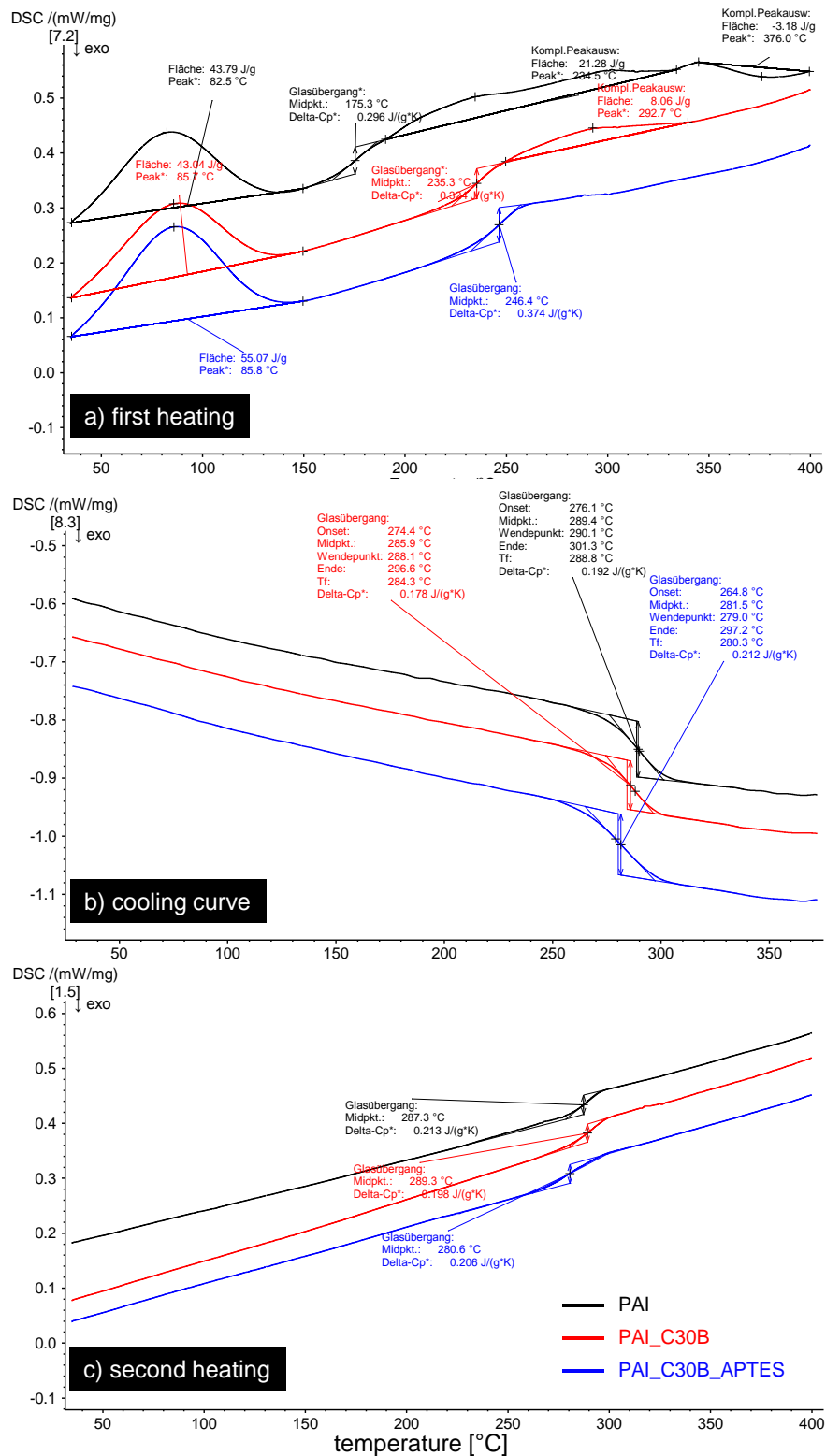


Figure 71: DSC measurements of PAI (black), PAI_C30B (red) and PAI_C30B_APTES (blue). First heating is shown in (a) followed by cooling phase (b) and second heating (c).

Because shifts of glass transition values were observed at DSC measurements, consecutive DMA cycles were exemplary conducted at PAI_C30B. The investigation focused on the influence of remaining NMP and advancing PAI conversion on thermo-mechanical properties. Consecutive DMA-cycles from 50 to 400 °C were performed and store modulus over temperature increase were measured.

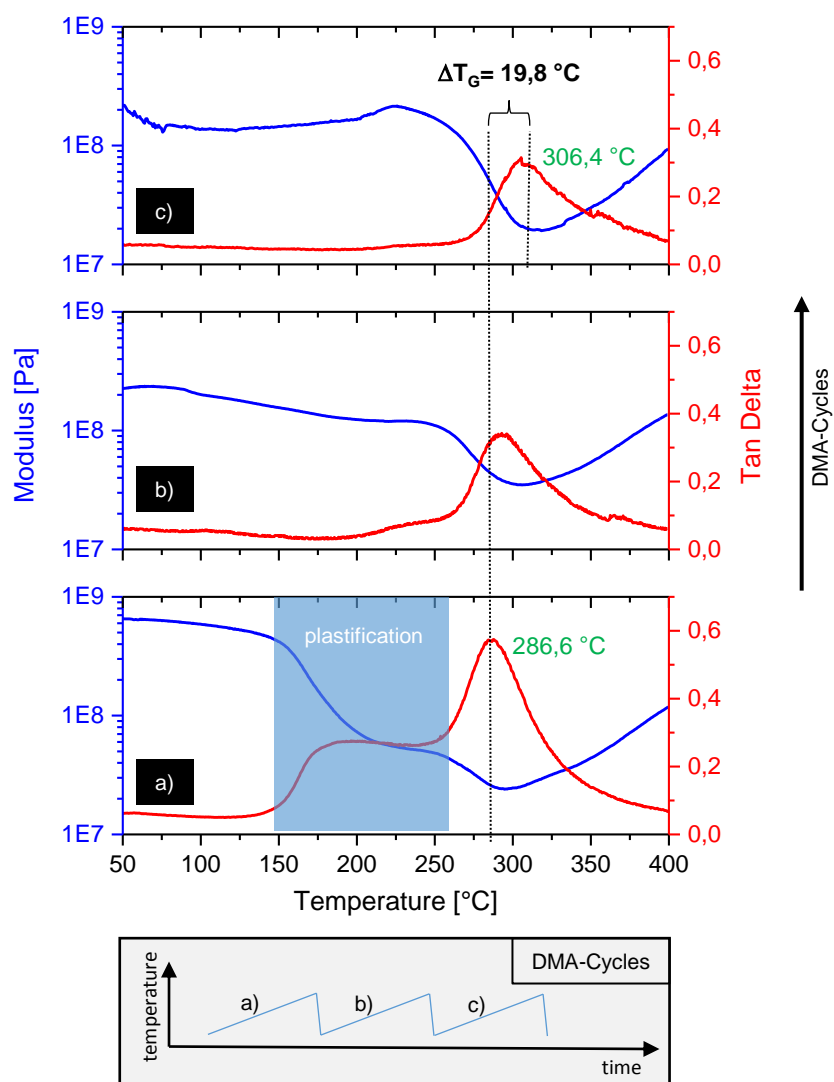


Figure 72: Plots of DMA-analysis of modulus (blue) and Tan Delta (red) over three periods of the three measurement cycles (a), (b) and (c). Inset graphic illustrates the DMA-Cycles applied in measurements. The experiment was exemplary conducted at PAI_C30B.

At first heating in Figure 72 (a) from 150 °C to about 260 °C a zone was observed, where storage modulus decreased and Tan Delta increased accordingly. From preliminary experiments of solubility it is known that this region is likely related to remaining NMP, which is able to dissolve the polymer matrix at high temperatures. Resulting plastification

is assumed to be responsible for the effect measured. Following peak in Tan Delta indicated the systems glass transition temperature.

In order to study changes of thermo-mechanical properties induced by interphase modification via silane, DMA-analyses were performed. Derived from prior results of DMA-cycles, samples were isothermally treated at 220 °C to eliminate the influence of plastification effect on determination of glass transition temperatures. As at measurements before, results were compared to PAI and PAI_C30B. Because it is known that location of glass transition temperatures strongly depend on the heat rate applied, they were chosen to be at 10 °C/min which corresponds to rates of prior DSC measurements.

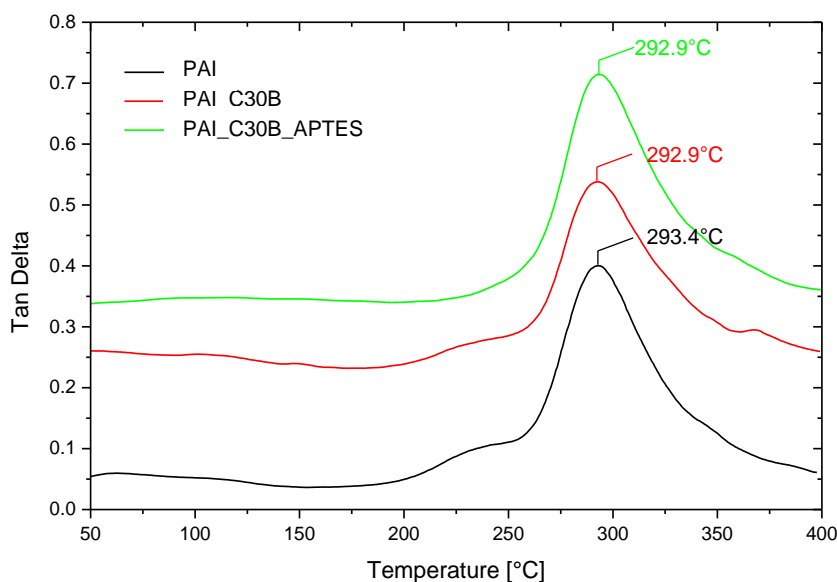


Figure 73: Glass transition temperatures of PAI (black), PAI_C30B (red) and PAI_C30B_APTES (green) determined via DMA-analysis.

The results in in Figure 73 show measurements of Tan Delta over temperature of PAI (black), PAI_C30B (red) and PAI_C30B_APTES (green). The existence of distinct peaks indicated glass transition temperatures. They were determined at respective peak maxima with 293.4 °C for PAI and 292.9 °C for PAI_C30B and PAI_C30B_APTES, respectively. These values thus correlate with prior determined values of DSC-analyses.

To conclude, determination of glass transition temperatures strongly depends on the method of measurement and applied heat rates and therefore is hard to interpret. It turned out, that sample preparation in terms of temperature treatment is crucial.

5.3.3 Mechanical properties

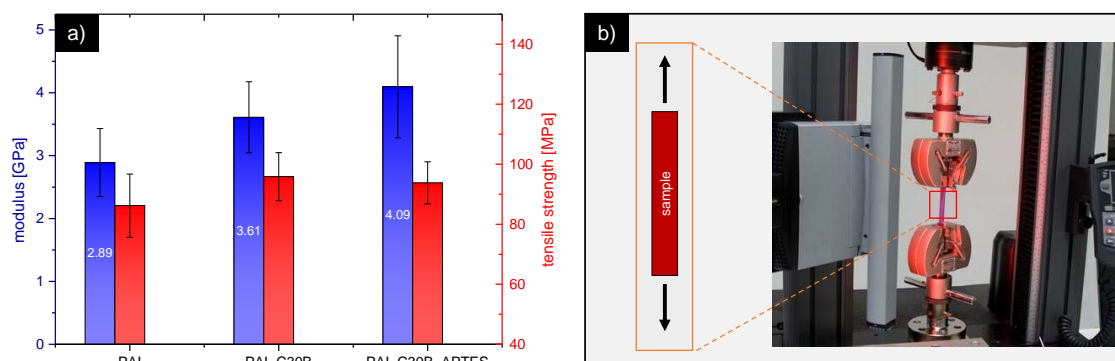


Figure 74: Comparison of PAI, PAI_C30B and PAI_C30B_APTES. (a) Modulus (left axis, blue) and tensile strength (right axis, red). (b) illustrates the experimental setup in principle of shear strength measurement.

Tensile tests were performed in order to determine the mechanical properties of PAI_C30B_APTES in comparison to PAI and PAI_C30B. The results are shown in Figure 74 (a). The tensile strength showed slightly lower values for pure PAI. Because of the measurement error, this difference is not assumed to be significant. In terms of Young's modulus results are different. With regard to PAI with a modulus of 2.89 GPa, PAI_C30B_APTES clearly exhibited an increase to 4.09 GPa. This corresponds to a relative increase of 41.5 %.

Considering the modulus of PAI_C30B (3.61 GPa) it can be assumed, that this effect is mainly related to the presence of the inorganic lamellar phase and their interface to the polymer. But through silane modification the values further increased. One explanation for this effect could be related to multiple bonding of single PAI chains to different MMT. This would lead to the formation of cross-linked polymer network induced by the modified silane surface which results in a more rigid system with an enhanced Young's modulus. A suggested morphology of this system is provided in Figure 75.

This model in conjunction with the results from FTIR-measurements (chapter 4) also explains why higher yields of PAI's imide rings to amide structures through coupling are not likely. As it can be seen at results of computational simulations (chapter 3), PAI chains exhibit a distinct helical structure which prevents imide groups which are not proper oriented to silane groups of the MMT-surface from grafting reaction.

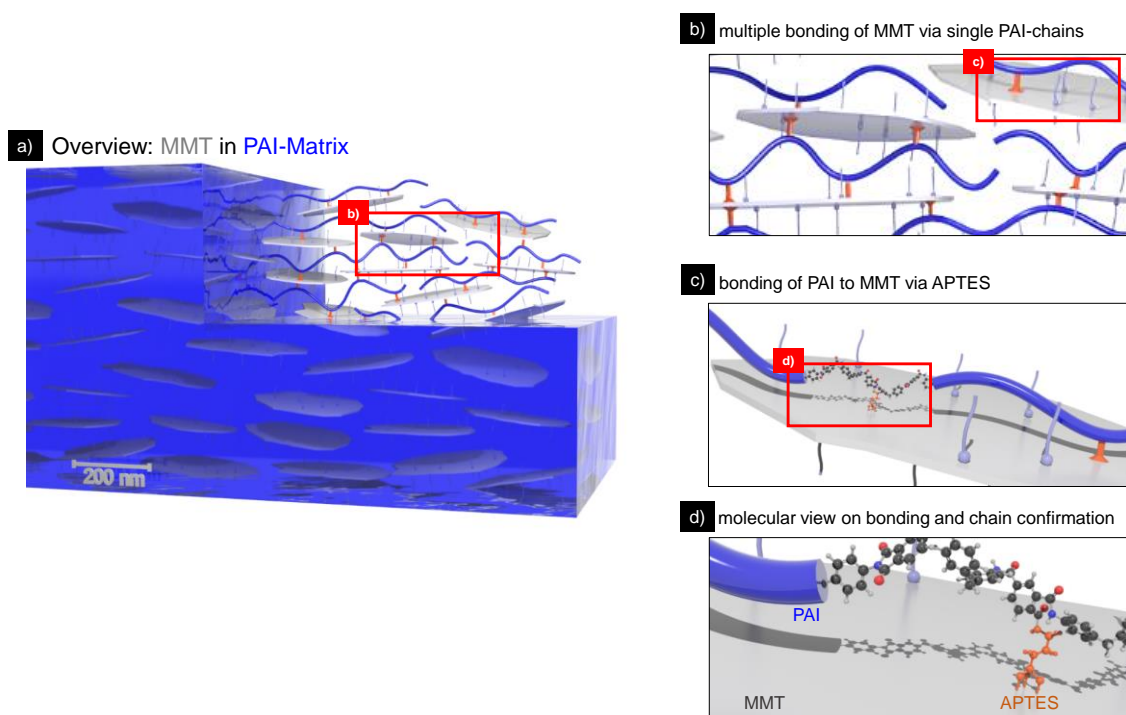


Figure 75: (a) Overview of model of suggested PAI_C30B_APTES structure of silane induced crosslinking in nanocomposites. MMT (grey sheets) is embedded in polymer matrix (blue phase) and crosslinked via APTES (orange)-modified MMT. (b) shows a magnified section where MMT is crosslinked with single PAI chains. (c) shows a detailed molecular view of polymer structure and bonding of MMT and PAI through APTES.

SEM-analysis were conducted at fracture surfaces of the samples PAI, PAI_C30B and PAI_C30B_APTES which were applied at the tensile tests. The results are summarized in Figure 76. It can be seen in Figure 76 (a) that PAI exhibited a fracture surface without any noticeable surface structure. MMT filled PAI_C30B showed in Figure 76 (b) fracture where single particles are exposed.

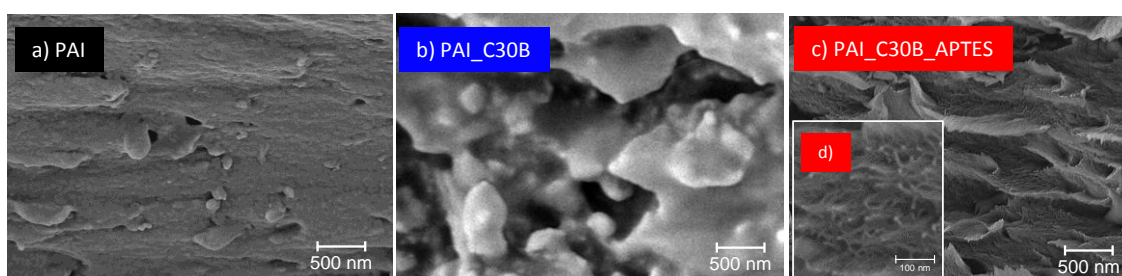


Figure 76: SEM images at cross-sections after tensile test of (a) pure PAI, (b) PAI_C30B and (c) PAI_C30B_APTES at the same level of magnification. (d) inset image shows detailed thread-like nanostructure with higher magnification.

It can be assumed, that crack formation occurred at particle-polymer interfaces. At modified PAI_C30B_ APTES in Figure 76 (c) these interphases were covalently bonded resulting in a thread-like nanostructure in the phase of PAI. In contrast to PAI_C30B, due to modification of the polymer-particle-interface no exposed particles were observed.

5.4 Summary

This chapter focused on the question, how the performance of PAI is affected in terms of mechanical, thermomechanical and dielectrical properties via covalently bonded exfoliated PAI-MMT-nanocomposites. To evaluate the effect of this modification, all experiments were carried out with pure and MMT-filled PAI (PAI_C30B) as references.

In the first part, measurements of dielectric breakdown strength were conducted. The best performance and hence significant enhanced DBS was observed for PAI with exfoliated and covalently bonded MMT (PAI_C30B_APTES). Because results of PAI_C30B were in the range of pure PAI, this effect is assumed to originate from changes in the interface of MMT through silane modification. Following experiments with constant voltage showed, that embedded MMT indeed influenced the mechanisms of material injury. Elemental analysis via EDX and investigations via SEM showed a change from a thermal breakdown mechanism at samples of PAI to an electrical breakdown due to tracking and treeing.

To investigate changes in thermal properties, DTGA studies were performed. The results showed increasing decomposition temperatures from PAI (437 °C) over PAI_C30B (448 °C) to PAI_C30B_APTES (452 °C). This was surprising, because at the bonding process between particles and polymer matrix, imide structure which are responsible for heat resistance where transformed to amide structures. This indicates changes in the polymer structure induced by covalent bonded particles resulting in improved thermal resistance. Subsequent SEM-analyses at respective fracture surfaces of the specimens from tensile tests confirmed this effect.

This assumption was confirmed by investigations of mechanical properties via tensile tests. PAI_C30B_APTES exhibited an increased modulus by 41.5 %. Hence, there is a significant improvement in comparison to PAI_C30B. This results clearly indicate that the effect is mainly not related to the filling effect with MMT, but a distinct change in the resulting morphology of the nanocomposite.

Concluding, the resulting nanocomposite PAI_C30B_APTES exhibited following properties:

- increased decomposition temperature by 15 °C
- increased modulus by 41.5 %
- enhanced dielectrical breakdown strength by 22.8 % in scale and 78.9 % in shape

Chapter 6: Application as adhesive

6.1 Introduction

The underlying idea of this chapter bases on observations at the sample preparation of stand-alone films for tensile strength measurements described in chapter 5. where during the removing process differences in adhesion properties were observed. While PAI and PAI_C30B could be separated easily from glass substrates, samples of PAI_C30B_APTES exhibited a distinct increase in adhesion.

In the following chapter the prior designed materials PAI, PAI_C30B and PAI_C30B_APTES are evaluated in terms of its potentials in applications as adhesives. This application enables mechanistically investigations of adhesion and cohesion properties due to measurements of shear strength. Because these measurements cannot be performed with glass substrates, changes in adhesion and cohesion of samples are investigated with steel substrates.

Subsequent micromechanical analyses at the surfaces of sample fractures will be conducted in order to analyse changes in the fractural morphology of nanocomposites due to silane modification with APTES.

6.2 Experimental

6.2.1 Sample preparation

For shear strength measurements, preparation of homogeneous adhesive films was realized by double layer application. First of all, cleaned steel substrates were coated with the samples and dried initially isothermal at 140 °C for 10 min in a gradient oven (Byk Gardner gradient oven 2610) followed by temperature ramp with a heating rate of 10 °C/min to 200 °C. After another isothermal condition for 10 min the films were finally treated at 220 °C for 30 min leading to completion of PAI-Synthesis resulting in dry films. Consecutively, a thin second layer was applicated and dried isothermal at 160 °C for 10 min. For shear strength measurements two specimens were pressed together and heated at 220°C for 30 min. An image of one specimen before bonding is shown in following figure.

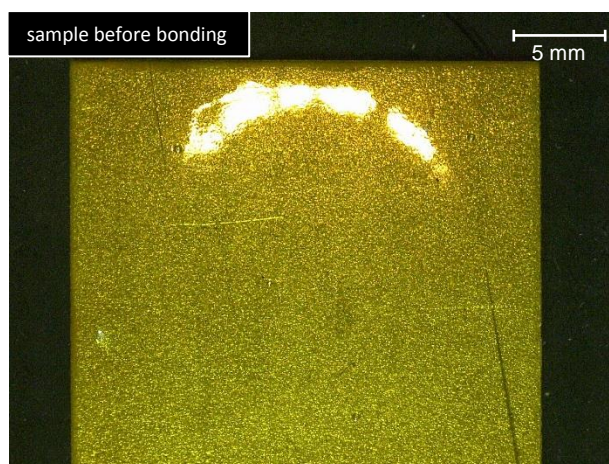


Figure 77: Optical microscope image of specimen before bonding.

6.2.2 Characterization

In order to investigate potentials in application as adhesive, shear strength measurements were performed on a Zwick Z100. Testing speed was 1 mm/min with samples of 25 mm in width, an overlap length of 16 mm, clamping length of 95 mm and distance of fine strain extensometer was 30 mm. A minimum of 10 specimens were tested for each sample. Execution of experiments were conducted according to DIN EN 1465. Obtained results are quoted as the average values with deviation from all tested samples of each composite.

6.3 Results and discussion

6.3.1 Method for sample preparation

This chapter focuses on the evaluation of the potential in applications as adhesive coating. In case of PAI, adhesive bonding of substrates could not be conventionally prepared by simple application and drying under heat. This led to formation of bubbles of carbon dioxide within the film, derived from ongoing reaction of PAI under heat and retention of NMP. This issue could be solved by prefabricated double layer application described in the characterization part of this chapter. A process scheme is provided in Figure 78.

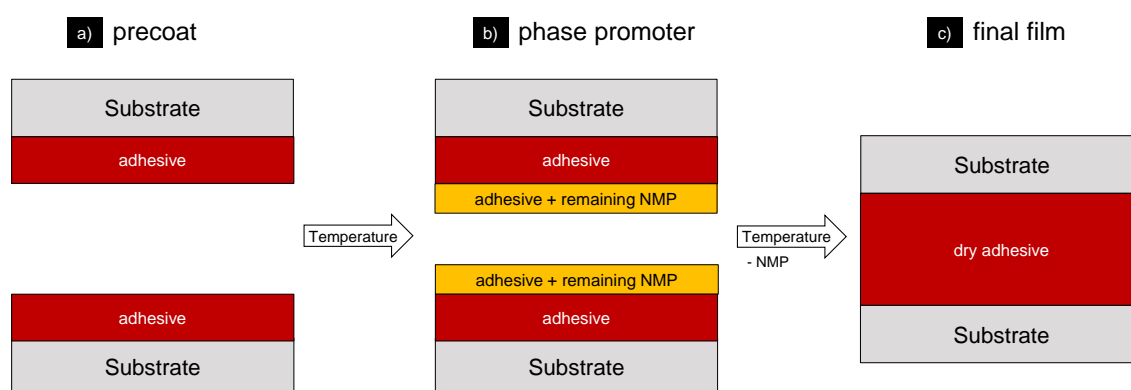


Figure 78: Scheme of sample preparation for shear strength measurements.

First layer thickness was in the range of 70 microns and was purposed to provide the base for a higher overall film thickness. Subsequently, a thinner second layer of several microns was applied and dried only at 160 °C resulting in a non-sticky top coat. But in this layer large amounts of remaining solvent NMP were present. Finally, prefabricated samples were pressed together and heated to 220 °C. At this step, the second layers act as promoter between both first layers. Due to remained NMP it dissolves the surface of the first layer and furthermore interdiffuses with the other second layer. Because of the heat treatment, PAI reaction continues resulting in the combination of both samples to a homogeneous total adhesive film.

6.3.2 Shear strength measurements

Following, shear strength measurements were conducted. The results are shown in Figure 79. In terms of relative strain at the point of failure, no significant difference between the samples could be observed.

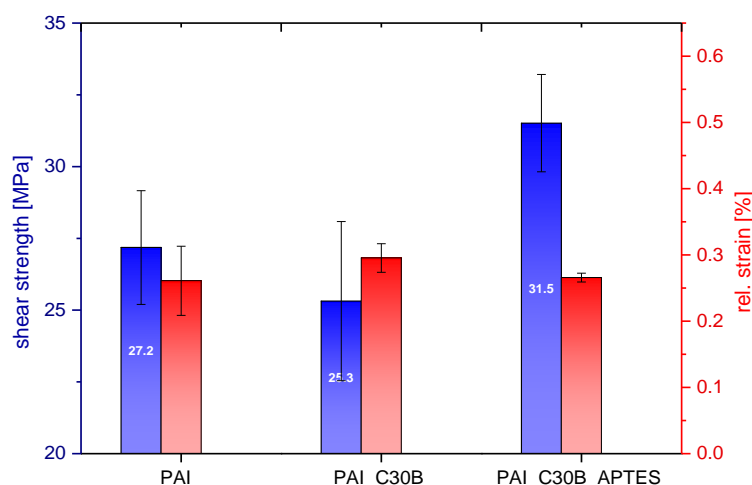


Figure 79: Shear strength (left axis, blue) and relative strain at breakdown (right axis, red) of pure PAI, PAI_C30B and PAI_C30B_APTES.

But as far as shear strength was concerned, PAI_C30B_APTES exhibited an increased strength by 15.8 % from 27.2 MPa of pure PAI to 31.5 MPa. In contrast to tensile strength measurements, PAI_C30B decreased slightly to 25.3 MPa. It can be stated, that all PAI samples showed high performance at the application as adhesive and could be categorized as structural adhesive.

6.3.3 Morphology

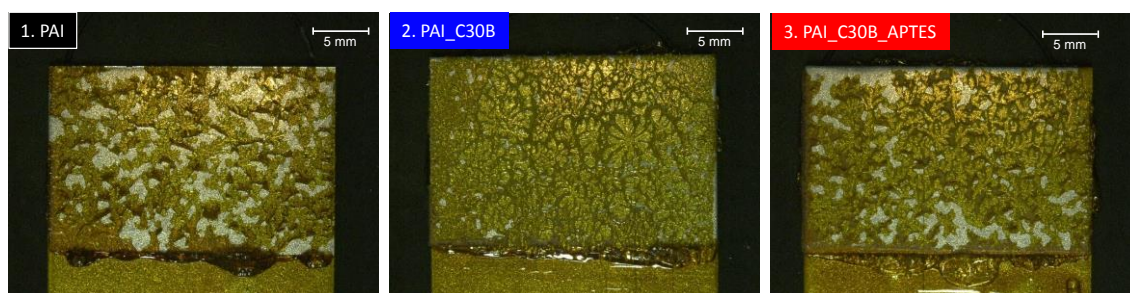


Figure 80: Overview images of PAI (black), PAI_C30B (blue) and PAI_C30B_APTES (red) after measurement of shear strength. Images were taken with an optical microscope at 10 times magnification.

In order to provide explanations for the underlying mechanisms, fracture analysis was conducted via microscope and SEM at samples of PAI (series 1, black), PAI_C30B (series 2, blue) and PAI_C30B_APTES (series 3, red). Overview images of respective samples are provided in Figure 80. In general, three kinds of failure were observed. Following scheme (Figure 81) illustrates the assignments of these failure mechanism to

the resulting observation at SEM-analysis. The two common ones are failure due to cohesive (red) and adhesive (blue) breakdown. Areas of adhesive failure were identified by the presence of positive/negative imprints of substrate's grain boundaries in the adhesive layer. The third failure results from preparation of samples. Here, both specimen parts did not form a homogeneous total layer leading to parts where original interfaces remain.

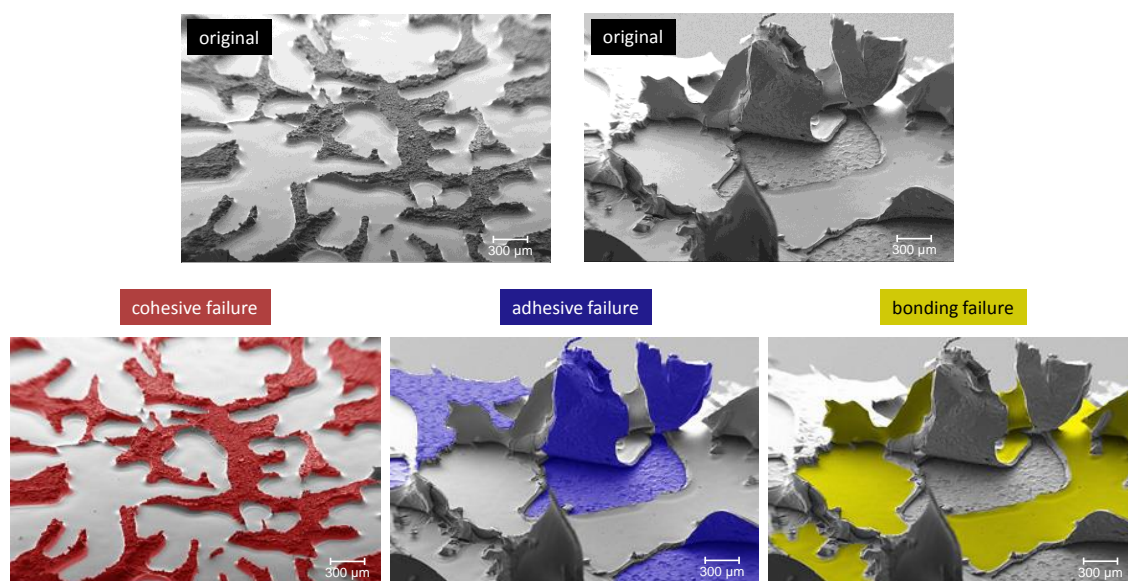


Figure 81: Illustration of possible mechanism of failure. These are cohesive failures (red), adhesive failures (blue) and failures due to bonding defects (yellow).

Detailed results of the investigation of underlying mechanism are shown in Figure 82. From top to bottom the magnification of each series was stepwise increased. At level 1, microscope images show an initial impression of the fractures after shear strength tests. PAI exhibited large and clear remaining fragments whereas the other two samples show optical changed areas which derive from stress whitening. Images of level 2 and following images were taken via SEM with increasing magnification.

At level 2 further differences were observed. PAI and PAI_C30B_APTES have a mixed fracture of adhesion and cohesion failure. In contrast, PAI_C30B showed exclusively cohesive failures. Regarding to all three systems, large areas were observed at which the adhesive layers did not form a total layer during the sample preparation. Therefore, it can be stated, that merely small areal portions were used for the bonding of substrates.

At images of level 3 and 4 the focus was set on the fraction behaviour at micro and nanoscale. PAI showed a kind of crystalline fracture with long steady fracture lines in micro scale. At nanoscale no certain details were observed. PAI_C30B and PAI_C30B_APTES exhibited a rough structure of fraction. Similar to tensile tests

analysis, single exposed MMT particles were observed at PAI_C30B, but not for PAI_C30B_APTES. This indicates, that the failure at the interface between particle and polymer could be prevented through modification via silane.

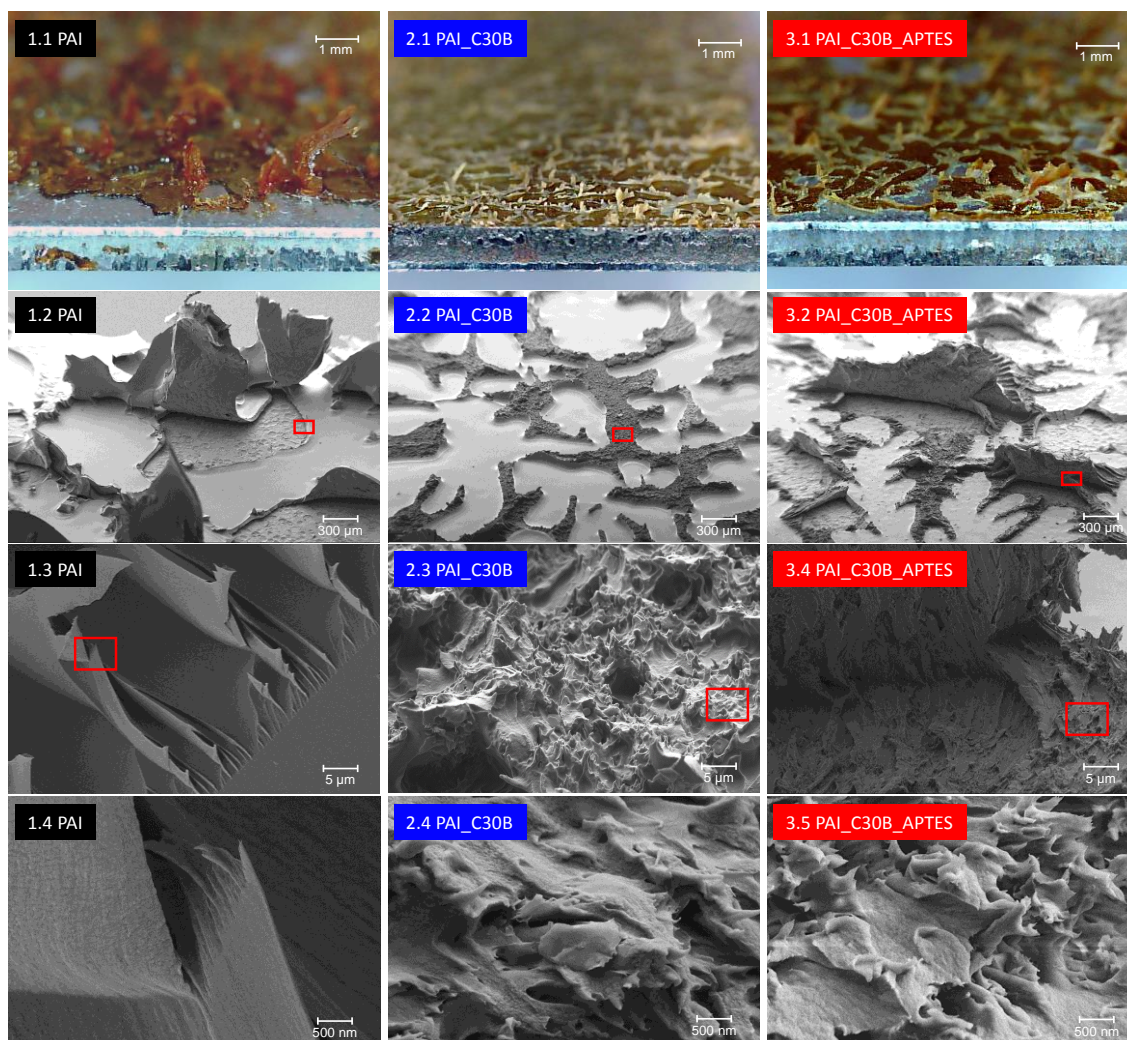


Figure 82: Analysis of fractures after shear strength test of (1) pure PAI, (2) PAI_C30B and (3) PAI_C30B_APTES with increasing level of magnification. Red rectangles indicate the position of the following image with higher magnification.

Taking the low amount of areas into account which formed a bonding layer, it is likely that the shear strength of these systems could be considerable increased with a further improved process of application.

6.4 Summary

The underlying idea of this chapter bases on observations at the sample preparation of stand-alone films for tensile strength measurements as described in chapter 5. They were conducted through application of sample materials on glass substrates, drying in an oven and mechanical removal of sample films. During the removing process differences in adhesion properties were observed. While PAI and PAI_C30B could be separated easily from glass substrates, samples of PAI_C30B_APTES exhibited a distinct increase in adhesion.

This chapter therefore focused on the evaluation of the potential in applications as adhesive coating. In case of the PAI-materials in this study, adhesive bonding of substrates could not be conventionally prepared by simple application and drying under heat. This led to formation of bubbles of carbon dioxide within the film, derived from ongoing reaction of PAI under heat and retention of NMP. This issue was solved by a new method of prefabricated double layer application.

Subsequently, shear strength measurements were conducted. As far as shear strength was concerned, PAI_C30B_APTES exhibited an increased strength by 15.8 % in relation to PAI. Measurements of PAI_C30B showed a slightly decreased shear strength. Basically it can be stated, that all PAI samples showed high performance at the application as adhesive and could be categorized as structural adhesive.

In order to provide explanations for the underlying mechanisms, fracture analyses were conducted via microscope. PAI_C30B and PAI_C30B_APTES exhibited a rough structure of fracture. Similar to tensile tests analysis, single exposed MMT particles were observed at PAI_C30B, but not for PAI_C30B_APTES. This indicates, that the failure at the interface between particle and polymer could be prevented through modification via silane.

Taking the low amount of areas into account which formed a bonding layer, it is likely that the shear strength of these systems could be considerably increased with a further improved process of application. First shear stress experiments revealed potential for applications in the field of adhesives. But preparation of samples turned out to be crucial.

Chapter 7: Profile of key properties

This chapter summarizes chosen key properties in terms of mechanical, thermal, thermomechanical and dielectrical properties of the materials investigated in this study. These were PAI only (PAI), PAI filled with exfoliated montmorillonite (PAI_C30B) and PAI_C30B_APTES where the interphases between particles and polymer matrix were covalently bonded via amino-functional trialkoxysilanes. A summary of all results is shown in the following table.

Table 8: Summary of key properties of PAI, PAI_C30B and PAI_C30B_APTES.

sample	modulus	shear strength	DBS	T _g	decomp. temp.
	[GPa]	[MPa]	[kV/mm]	[°C]	[°C]
PAI	2,89	27,2	311	293	437
PAI_C30B	3,61	25,3	325	293	448
PAI_C30B_APTES	4,09	31,5	382	293	452

It bases on the results of the characterization of nanocomposites derived from chapter 5. Further, it is supplemented with the results of chapter 6, where respective shear strengths at applications as adhesive were provided. The chosen key properties in this study are the decomposition temperature, modulus, shear strength, dielectric breakdown strength and the glass transition temperature. Highest values of respective measurements are highlighted with bold font.

Figure 83 provides an overall graphical profile of key properties. At the first part (a) an overall profile of all three materials is shown. Below, the individual profiles of properties are shown for PAI (b), PAI_C30B (c) and PAI_C30B_APTES (d).

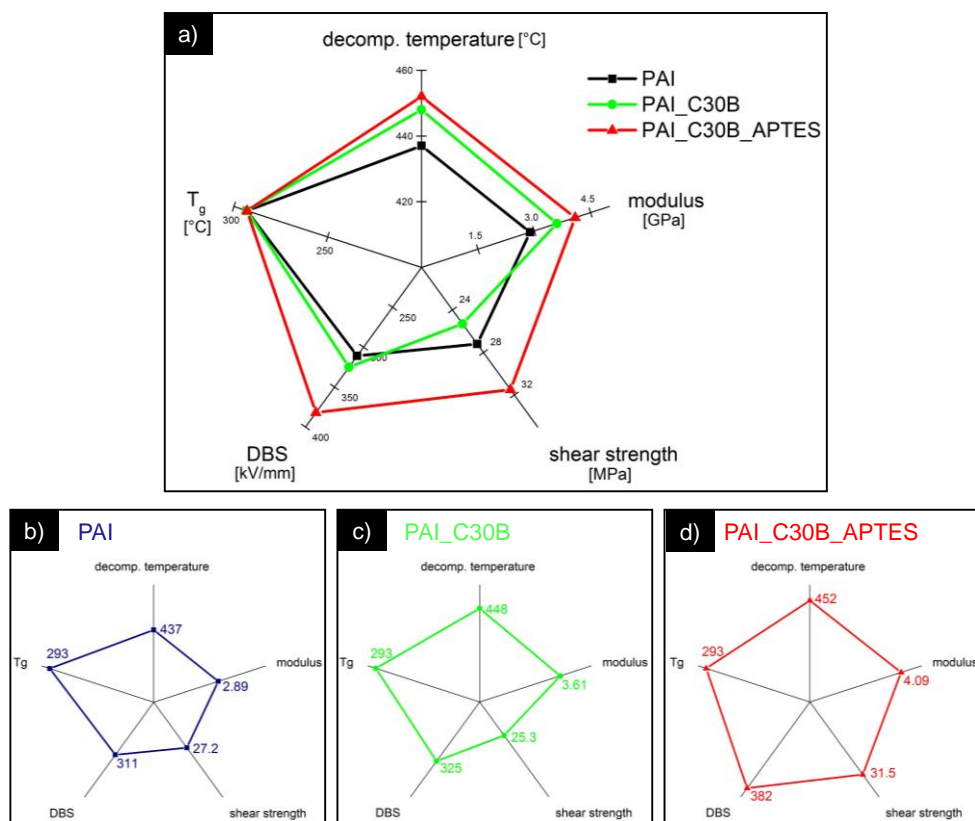


Figure 83: Summary of the key properties decomposition temperature, modulus, shear strength, dielectrical breakdown strength and glass transition temperature. (a) Comparison of PAI, PAI_C30B and PAI_C30B_APTES. Detailed view of respective samples are shown in (b), (c) and (d).

In this study PAI serves as reference for both modifications. It already showed an overall performance which can be attributed to the class of high performance polymers. At PAI_C30B the implementation of exfoliated montmorillonite resulted in improvements at modulus and decomposition temperature. In case of dielectrical behavior and glass transition temperature, no significant changes were observed. When it comes to shear strength, these particles cause a detrimental effect.

The best overall performance was achieved for PAI_C30B_APTES. In almost all key properties improvements were observed, except for glass transition temperatures. Here, both modifications of PAI showed no effect.

Chapter 8: Summary, conclusion and outlook

8.1 Summary

In the present thesis, the effect of interphase modification at nanocomposites of polyamide-imide and montmorillonite on thermal, mechanical and dielectric properties was investigated. The key parts were as followed:

- Synthesis of nanocomposites
- Modification of interphases
- Characterization of nanocomposites
- Application as adhesive

From basic micromechanical models it could be stated that the ratio of the composite modulus to the matrix modulus values tends to increase with the exfoliation of platelets. Accordingly, incomplete exfoliation has a very significant detrimental effect on the mechanical reinforcement efficiency. Based on this effect the first part, the synthesis of nanocomposites, dealt with the question how nanocomposites with completely exfoliated montmorillonite can be achieved. In literature, several methods for a variety of polymer systems were widely investigated, except for polyamide-imide. Therefore, two known methods were chosen to be adapted to realize exfoliated polyamide-imide-montmorillonite nanocomposites. These are the solvent casting method and the *in situ* polymerization. Both methods were investigated with two different types of organo-modified montmorillonite.

Solvent casting was performed by swelling MMT particles in NMP followed by dropwise addition of PAI solution and dispersing. XRD and SEM analysis showed exfoliated states until clay concentrations of 1.2 wt-% which is assumed to be the percolation threshold of this system. With further increasing concentrations, increasing amounts of intercalated MMT particles were observed.

With *in situ* polymerization, a novel approach towards exfoliated PAI-MMT-nanocomposites was developed. It was performed by swelling MMT intergalleries with PCP-blocked MDI and TMA monomers followed by polymerization to PAI within the intergalleries. Successful swelling due to the presence of monomers within the intergalleries and successful exfoliation was verified via XRD-measurements. Experiments with increasing MMT concentration showed a limit for complete exfoliation at 2.0 wt-%. Subsequent computational simulations of equilibrium geometry conducted for blocked MDI showed good correlation to enlargement of MMT's intergallery spacing which supported the thesis of successful swelling. Following SEM analyses at cross-sections indicated in the first instance poor particle distribution but high degree of exfoliation. Subsequent dispersing of the sample enabled homogenous distributions of particles within the polymer matrix. FTIR measurements proved successful formation of characteristic amide and imide structures during *in situ* polymerization.

In comparison to *in situ* polymerization the solvent casting method turned out to be simpler, faster and economically more feasible. A distinct influence of the different organo-modified particles used in this work on the processes of *in situ* polymerization was not found. Because of these results, subsequent preparation of nanocomposites was based on PAI-MMT-nanocomposite derived from Cloisite 30B which are synthesized via the solvent casting method.

The second part of this study focused on the modification of MMT-surfaces with APTES in order to provide a functional group which is able to graft MMT covalently to the polymer matrix. This group was chosen to be an amine. The strategy was to enable the grafting reaction via imide ring opening reaction under formation of an amide link. Initially, DBS-measurements on composites with varying MMT concentration were conducted in order to determine the electrical percolation threshold. This threshold represents the maximum concentration of MMT which can be realized without losing the dielectrical character of the resulting composite. It was reached at a MMT concentration of 0.6 wt-%. The success of grafting reaction of APTES to MMT was evidenced via ^{29}Si -NMR-measurements. The grafting reaction to the polymer matrix via imide ring opening was investigated using FTIR measurements. It could be shown that the silane modification converted about 23 % of imide rings to amide structures after synthesis with PAI. This indicates a high coverage of APTES on MMT. Results of XRD-measurements

indicated that APTES molecules were intercalated and grafted to interlayer surface silanol groups.

The third part, characterization of nanocomposites, dealt with the question, how the performance of PAI is affected in terms of mechanical, thermomechanical and dielectrical properties via covalently bonded exfoliated PAI-MMT-nanocomposites. To evaluate the effect of this modification, all experiments were carried out with pure and MMT-filled PAI (PAI_C30B) as references at MMT concentrations of 0.6 wt-%.

Measurements of dielectric breakdown strength were conducted. The best performance and hence significant enhanced DBS was observed for PAI with exfoliated and covalently bonded MMT (PAI_C30B_APTES). Because results of PAI_C30B were in the range of pure PAI, this effect is assumed to originate from changes in the interface of MMT through silane modification. Following experiments with constant voltage showed, that embedded MMT indeed influenced the mechanisms of material injury. Elemental analysis via EDX and investigations via SEM showed a change from a thermal breakdown mechanism at samples of PAI to an electrical breakdown due to tracking and treeing.

To investigate changes in thermal properties, DTGA studies were performed. The results showed increasing decomposition temperatures from PAI (437 °C) over PAI_C30B (448 °C) to PAI_C30B_APTES (452 °C). This was surprising, because at the bonding process between particles and polymer matrix imide structures, which are responsible for heat resistance, were transformed to amide structures. It indicates changes in the polymer structure induced by covalent bonded particles resulting in improved thermal resistance. Subsequent SEM-analyses at respective fracture surfaces of the specimens from tensile tests confirmed this effect. This assumption was supported by investigations of mechanical properties via tensile tests. PAI_C30B_APTES exhibited an increased modulus by 41.5 %. Hence, there is a significant improvement in comparison to PAI_C30B. These results clearly indicate that the effect is not mainly related to the filling effect with MMT, but a distinct change in the morphology of the nanocomposite.

The underlying idea of the last part, application as adhesive, bases on observations at the sample preparation of stand-alone films for tensile strength measurements described in chapter 5. They were conducted through application of sample materials on glass substrates, drying in an oven and mechanical removing of sample films. During the removing process differences in adhesion properties were observed. While PAI and PAI_C30B could be separated easily from glass substrates, samples of PAI_C30B_APTES exhibited a distinct increase in adhesion. This chapter therefore focused on the evaluation of the potential in applications as adhesive coating. In case of the PAI-materials in this study, adhesive bonding of substrates could not be

conventionally prepared by simple application and drying under heat. This led to formation of bubbles of carbon dioxide within the film, derived from ongoing reaction of PAI under heat and retention of NMP. This issue was solved by a new method of prefabricated double layer application.

Subsequently, shear strength measurements were conducted. As far as shear strength is concerned, PAI_C30B_APTES exhibited an increased strength by 15.8 % in relation to PAI. Measurements of PAI_C30B showed a slightly decreased shear strength. Basically it can be stated that all PAI samples showed high performance at the application as adhesive and could be categorized as structural adhesive.

In order to provide explanations for the underlying mechanisms, fracture analyses were conducted via microscope. PAI_C30B and PAI_C30B_APTES exhibited a rough structure of fracture. Similar to tensile tests analysis, single exposed MMT particles were observed at PAI_C30B, but not for PAI_C30B_APTES. This indicates, that the failure at the interface between particle and polymer could be prevented through modification via silane.

8.2 Conclusion and Outlook

In this study, the effects of internal interphase modification in nanocomposites of montmorillonite and polyamide-imide on thermal, mechanical and dielectrical properties were investigated. Two strategies of synthesis for exfoliated states of particles provided a profound base for the sample preparation in subsequent characterization. The internal modification of interphases in these nanocomposites was conducted via covalent bonding with an amino functional silane.

To conclude, with regard to PAI as reference the resulting nanocomposite with modified internal interphases PAI_C30B_APTES exhibited following changes in properties:

- increased decomposition temperature by 15 °C
- increased modulus by 41.5 %
- enhanced dielectrical breakdown strength by 22.8 % in scale and 78.9 % in shape
- shear strength which enables applications as structural adhesive

With regard to the application as adhesive, taking the low amount of areas into account which formed a bonding layer, it is likely that the shear strength of these systems can be considerably increased with a further improved process of application. First shear stress experiments revealed potential for applications in the field of adhesives. But preparation of samples turned out to be crucial.

Therefore, further work on optimization of sample preparation and clarification of underlying mechanisms has to be conducted. Another parameter for further improvements would be the optimization of the silane modification on surfaces of MMT. The approach of this study was a complete coverage of surfaces with silanes. It can be assumed that changes at this parameter enable new properties.

List of publications

1. Strube OI, Briesenick D, Heckel T, Brikmann J, Hüsgen B, *Fortschrittsberichte der Materialforschung und Werkstofftechnik / Bulletin of Materials Research and Engineering*, ISBN 978-3-8440-3403-5, Shaker-Verlag, Maastricht / Herzogenrath, p. 9-17 (2015).
2. Heckel T, Brikmann J, Hüsgen B, Strube OI, Briesenick D, Silikonwerkzeuge für Vakuumgießprozesse - Untersuchung der Alterungsmechanismen und Erhöhung der Lebensdauer, *Vortrag auf dem 1. Niedersächsischen Symposium Materialtechnik*, Clausthal-Zellerfeld (2015).
3. Briesenick D, Bremser W; Modification of internal interphases of PAI-MMT-nanocomposites: Dielectrical and mechanical properties. *Prog. Org. Coatings* 2015 (submitted in 2014, currently under review)
4. Briesenick D, Bremser W; Synthesis of polyamide-imide-montmorillonite-nanocomposites via new approach of in situ polymerization and solvent casting. *Prog. Org. Coatings* **82**, 26–32 (2015).
5. Strube OI, Briesenick D, Brikmann J, Hüsgen B. Examination of the Aging Effects of Silicone Molds During Vacuum Casting Processes via Scanning Electron Microscopy. *Polym Plast Technol Eng* **54**, 494–8, (2014).
6. Briesenick D, Bremser W; Exfoliated PAI-MMT-Nanocomposites; Synthesis, Properties and Application. *Coatings Science International* (2014) (poster presentation)
7. Briesenick D, Bremser W; Synthese, Charakterisierung und technische Anwendungen von PAI-MMT-Nanokompositen. *GDCH Lacktagung* (2013) (oral presentation)
8. Briesenick D, Bremser W; High Voltage Insulation via PAI-MMT-Nanocomposites. *Coatings Science International* (2013) (poster presentation)
9. Briesenick D; *Method for measuring the cloudiness of paints on test tables*. Patent WO/2011/048147

References

1. Long, Y. & Shanks, R. PP-elastomer-filler hybrids. I. Processing, microstructure, and mechanical properties. *J. Appl. Polym. Sci.* **61**, 1877–1885 (1996).
2. Bartczak, Z., Argon, A., Cohen, R. & Weinberg, M. Toughness mechanism in semi-crystalline polymer blends - I. HDPE toughened with rubber. *Polymer (Guildf)*. **40**, 2331–2346 (1999).
3. Misra, R., Nerikar, P., Bertrand, K. & Murphy, D. Some aspects of surface deformation and fracture of 5–20% calcium carbonate-reinforced polyethylene composites. *Mater. Sci. Eng. A* **384**, 284–298 (2004).
4. Unal, H., Mimaroglu, A. & Alkan, M. Mechanical properties and morphology of nylon-6 hybrid composites. *Polym. Int.* **53**, 56–60 (2004).
5. Takahara, A., Tateshi, M. & Tisato, K. Effect of glass fiber-matrix polymer interaction on fatigue characteristics of short glass fiber-reinforced poly(butylene terephthalate) based on dynamic viscoelastic measurement during the fatigue process. *J. Polym. Sci. Part B Polym. Phys.* **32**, 839–849 (1994).
6. DiBenedetto, A. Tailoring of interfaces in glass fiber reinforced polymer composites: a review. *Mater. Sci. Eng. A* **302**, 74–82 (2001).
7. Alexandre, M. & Dubois, P. Polymer-layered silicate nanocomposites: preparation, properties and uses of a new class of materials. *Mater. Sci. Eng. R Reports* **28**, 1–63 (2000).
8. Yano, K., Usuki, A. & Okada, A. Synthesis and properties of polyimide–clay hybrid. *J. Polym. Sci. Part A Polym. Chem.* **31**, 2493–2498 (1993).
9. Vaia, R., Ishii, H. & Giannelis, E. Synthesis and properties of two-dimensional nanostructures by direct intercalation of polymer melts in layered silicates. *Chem. Mater.* **5**, 1694–1696 (1993).
10. Giannelis, E. Polymer layered silicate nanocomposites. *Adv. Mater.* **8**, 29–35 (1996).
11. Giannelis, E., Krishnamoorti, R. & Manias, E. Polymer-silicate nanocomposites: model systems for confined polymers and polymer brushes. *Adv. Polym. Sci.* **138**, 107–147 (1999).

12. LeBaron, P. Polymer-layered silicate nanocomposites: an overview. *Appl. Clay Sci.* **15**, 11–29 (1999).
13. Vaia, R. Polymer/layered silicate nanocomposites as high performance ablative materials. *Appl. Clay Sci.* **15**, 67–92 (1999).
14. Biswas, M. & Sinha Ray, S. Recent progress in synthesis and evaluation of polymer–montmorillonite nanocomposites. *Adv. Polym. Sci.* **155**, 167–221 (2001).
15. Giannelis, E. P. Polymer-layered silicate nanocomposites: Synthesis, properties and applications. *Appl. Organomet. Chem.* **12**, 675–680 (1998).
16. Xu, R., Manias, E., Snyder, A. J. & Runt, J. New Biomedical Poly(urethane urea)–Layered Silicate Nanocomposites. *Macromolecules* **34**, 337–339 (2001).
17. Bharadwaj, R. Modeling the barrier properties of polymer-layered silicate nanocomposites. *Macromolecules* **34**, 9189–9192 (2001).
18. Messersmith, P. & Giannelis, E. Synthesis and barrier properties of poly(ϵ -caprolactone)-layered silicate nanocomposites. *J. Polym. Sci. Part A Polym. Chem.* **33**, 1047–1057 (1995).
19. Kojima, Y. & Usuki, A. Mechanical properties of nylon 6-clay hybrid. *J. Mater. Res.* **8**, 1185–1189 (1993).
20. Gilman, J. & Kashiwagi, T. Flammability studies of polymer layered silicate nanocomposites. *Mater. Process Engineering* 1053–1066 (1998).
21. Gilman, J. & Kashiwagi, T. Flammability studies of polymer layered silicate nanocomposites: polyolefin, epoxy, and vinyl ester resins. in *Chemistry and Technology of Polymer Additives* **14**, 249–265 (1999).
22. Bourbigot, S. & Bras, M. Le. PA-6 clay nanocomposite hybrid as char forming agent in intumescent formulations. *Fire Mater.* **24**, 201–208 (2000).
23. Sinha Ray, S. & Okamoto, M. Polymer/layered silicate nanocomposites: a review from preparation to processing. *Prog. Polym. Sci.* **28**, 1539–1641 (2003).
24. Brown, G. & Brindley, G. Crystal structures of clay minerals and their X-ray identification. *Mineral. Soc. London* 504 (1980).
25. Moore, D. & Reynolds, R. *X-ray Diffraction and the Identification and Analysis of Clay Minerals*. (Oxford University Press, 1997).
26. Olphen, H. Van & Hsu, P. An introduction to clay colloid chemistry. *Soil Sci.* **126**, 59 (1978).
27. Osman, M., Ploetze, M. & Skrabal, P. Structure and properties of alkylammonium monolayers self-assembled on montmorillonite platelets. *J. Phys. Chem. B* **108**, 2580–2588 (2004).

-
28. Fischer, H. Polymer nanocomposites: from fundamental research to specific applications. *Mater. Sci. Eng. C* **23**, 763–772 (2003).
 29. Wang, H., Zeng, C. & Elkovitch, M. Processing and properties of polymeric nanocomposites. *Polym. Eng. Sci.* **41**, 2036–2046 (2001).
 30. Kotek, J., Kelnar, I., Studenovský, M. & Baldrian, J. Chlorosulfonated polypropylene: preparation and its application as a coupling agent in polypropylene–clay nanocomposites. *Polymer (Guildf)*. **46**, 4876–4881 (2005).
 31. Pramoda, K. & Liu, T. Effect of moisture on the dynamic mechanical relaxation of polyamide-6/clay nanocomposites. *J. Polym. Sci. Part B Polym. Phys.* **42**, 1823–1830 (2004).
 32. Tjong, S. C. Structural and mechanical properties of polymer nanocomposites. *Mater. Sci. Eng. R Reports* **53**, 73–197 (2006).
 33. Theng, B. *Formation and properties of clay-polymer complexes*. (Elsevier B.V., 2012).
 34. Vaia, R. & Giannelis, E. Polymer Melt Intercalation in Organically-Modified Layered Silicates: Model Predictions and Experiment. *Macromolecules* **30**, 8000–8009 (1997).
 35. Morgan, A. B. & Gilman, J. W. Characterization of polymer-layered silicate (clay) nanocomposites by transmission electron microscopy and X-ray diffraction: A comparative study. *J. Appl. Polym. Sci.* **87**, 1329–1338 (2003).
 36. Eckel, D. F., Balogh, M. P., Fasulo, P. D. & Rodgers, W. R. Assessing organo-clay dispersion in polymer nanocomposites. *J. Appl. Polym. Sci.* **93**, 1110–1117 (2004).
 37. Vaia, R. A., Jandt, K. D., Kramer, E. J. & Giannelis, E. P. Microstructural Evolution of Melt Intercalated Polymer–Organically Modified Layered Silicates Nanocomposites. *Chem. Mater.* **8**, 2628–2635 (1996).
 38. Tanaka, T. Dielectric nanocomposites with insulating properties. *IEEE Trans. Dielectr. Electr. Insul.* **12**, 914–928 (2005).
 39. Kim, G.-M. & Michler, G. . Micromechanical deformation processes in toughened and particle filled semicrystalline polymers: Part 2. model representation for micromechanical deformation processes. *Polymer (Guildf)*. **39**, 5699–5703 (1998).
 40. Kim, G.-M. & Michler, G. . Micromechanical deformation processes in toughened and particle-filled semicrystalline polymers: Part 1. Characterization of deformation processes in dependence on phase morphology. *Polymer (Guildf)*. **39**, 5689–5697 (1998).

41. Zuiderduin, W., Westzaan, C., Huetink, J. & Gaymans, R. Toughening of polypropylene with calcium carbonate particles. *Polymer (Guildf)*. **44**, 261–275 (2003).
42. Bartczak, Z., Argon, A., Cohen, R. & Weinberg, M. Toughness mechanism in semi-crystalline polymer blends: II. High-density polyethylene toughened with calcium carbonate filler particles. *Polymer (Guildf)*. **40**, 2347–2365 (1999).
43. Lazzeri, A., Thio, Y. & Cohen, R. Volume strain measurements on CaCO₃/polypropylene particulate composites: The effect of particle size. *J. Appl. Polym. Sci. Appl. Polym. Sci.* **91**, 925–935 (2004).
44. Ragosta, G., Abbate, M., Musto, P., Scarinzi, G. & Mascia, L. Epoxy-silica particulate nanocomposites: chemical interactions, reinforcement and fracture toughness. *Polymer (Guildf)*. **46**, 10506–10516 (2005).
45. Fornes, T. & Paul, D. Modeling properties of nylon 6/clay nanocomposites using composite theories. *Polymer (Guildf)*. **44**, 4993–5013 (2003).
46. Zeng, Q., Yu, A. & Lu, G. Multiscale modeling and simulation of polymer nanocomposites. *Prog. Polym. Sci.* **33**, 191–269 (2008).
47. Dabrowski, F. & Bourbigot, S. Kinetic modelling of the thermal degradation: of polyamide-6 nanocomposite. *Eur. Polym. J.* **36**, 273–284 (2000).
48. Vaia, R. & Giannelis, E. Lattice model of polymer melt intercalation in organically-modified layered silicates. *Macromolecules* **30**, 7990–7999 (1997).
49. Lee, J. & Baljon, A. Simulation of polymer melt intercalation in layered nanocomposites. *J. Chem. Phys.* **109**, 10321 (1998).
50. Balazs, A., Singh, C. & Zhulina, E. Modeling the interactions between polymers and clay surfaces through self-consistent field theory. *Macromolecules* **31**, 8370–8381 (1998).
51. Ginzburg, V. & Balazs, A. Calculating phase diagrams of polymer-platelet mixtures using density functional theory: implications for polymer/clay composites. *Macromolecules* (1999).
52. Baljon, A., Lee, J. & Loring, R. Molecular view of polymer flow into a strongly attractive slit. *J. Chem. Phys.* **111**, 9068 (1999).
53. Ginzburg, V., Singh, C. & Balazs, A. Theoretical phase diagrams of polymer/clay composites: the role of grafted organic modifiers. *Macromolecules* **33**, 1089–1099 (2000).
54. Kuznetsov, D. & Balazs, A. Scaling theory for end-functionalized polymers confined between two surfaces: Predictions for fabricating polymer/clay nanocomposites. *J. Chem. Phys.* **112**, 4365 (2000).

-
55. Lee, J. & Baljon, A. Molecular dynamics study of the intercalation of diblock copolymers into layered silicates. *J. Chem. Phys.* **112**, 9112 (2000).
 56. Singh, C. & Balazs, A. Effect of polymer architecture on the miscibility of polymer/clay mixtures. *Polym. Int.* **49**, 469–471 (2000).
 57. Manias, E., Chen, H. & Krishnamoorti, R. Intercalation Kinetics of Long Polymers in 2 nm Confinements. *Macromolecules* **33**, 7955–7966 (2000).
 58. Ginzburg, V. & Balazs, A. Calculating Phase Diagrams for Nanocomposites: The Effect of Adding End-Functionalized Chains to Polymer/Clay Mixtures. *Adv. Mater.* **12**, 1805–1809 (2000).
 59. Affdl, J. & Kardos, J. The Halpin-Tsai equations: A review. *Polym. Eng. Sci.* **16**, 344–352 (1976).
 60. Halpin, J. Stiffness and expansion estimates for oriented short fiber composites. *J. Compos. Mater.* **3**, 732–734 (1969).
 61. Hermans, J. The elastic properties of fiber oriented materials when the fibers are aligned. *K. Inst. van Wet.* **65**, 1–9 (1967).
 62. Hill, R. Theory of mechanical properties of fibre-strengthened materials: I. Elastic behaviour. *J. Mech. Phys. Solids* **12**, 199–212 (1964).
 63. Yung, K., Wang, J. & Yue, T. Modeling Young's modulus of polymer-layered silicate nanocomposites using a modified Halpin—Tsai micromechanical model. *J. Reinf. Plast. Compos.* **25**, 847–861 (2006).
 64. Eshelby, J. D. The Determination of the Elastic Field of an Ellipsoidal Inclusion, and Related Problems. *Proceedings of the Royal Society A: Mathematical, Physical and Engineering Sciences* **241**, 376–396 (1957).
 65. Mori, T. & Tanaka, K. Average stress in matrix and average elastic energy of materials with misfitting inclusions. *Acta Metall.* **21**, 571–574 (1973).
 66. Benveniste, Y. A new approach to the application of Mori-Tanaka's theory in composite materials. *Mech. Mater.* **6**, 147–157 (1987).
 67. Tandon, G. P. & Weng, G. J. The effect of aspect ratio of inclusions on the elastic properties of unidirectionally aligned composites. *Polym. Compos.* **5**, 327–333 (1984).
 68. Manevitch, O. L. & Rutledge, G. C. Elastic Properties of a Single Lamella of Montmorillonite by Molecular Dynamics Simulation. *J. Phys. Chem. B* **108**, 1428–1435 (2004).
 69. Brune, D. A. & Bicerano, J. Micromechanics of nanocomposites: comparison of tensile and compressive elastic moduli, and prediction of effects of incomplete

- exfoliation and imperfect alignment on modulus. *Polymer (Guildf)*. **43**, 369–387 (2002).
70. Murray, T. J. Poly (amide-imides): Wire enamels with excellent thermal and chemical properties. *Macromol. Mater. Eng.* **293**, 350–360 (2008).
 71. Ressel, J. Oberflächenstrukturierung und Reibungseigenschaften von Polyamidimid-Polydimethylsiloxan-Copolymeren und Polydimethylsiloxan-Mikrogelen in Polyamidimid Beschichtungen. (University Paderborn, 2013).
 72. Stephens, J. Preparation of solid polymers from aromatic primary diamine and acyl halide of trimellitic anhydride. *US Pat.* 4,048,144 (1977).
 73. Nemours, P. De. United States Patent 3179360. (1965).
 74. Endrey, A. L. & Nostnand, V. United States Patent 3179631. **1387**, (1962).
 75. Endrey, A. L. United States Patent 3179633. 3–8 (1965).
 76. Koyania, T. NOVEL POLYIMIDAMIDE RESIN. *US Pat.* 3,541,038 (1970).
 77. Gheradi, P. *et al.* *Polymers for electrical insulation*. (Süddeutsche Verlag onpact GmbH, 2008).
 78. Lechner, M. D., Gehrke, K. & Nordmeier, E. H. *Makromolekulare Chemie*. (Springer Berlin Heidelberg, 2014).
 79. Dieckmann, W. & Breest, F. Notiz über das Verhalten von Carbonsäuren gegen Phenylisocyanat. *Berichte der Dtsch. Chem. Gesellschaft* **39**, 3052–3055 (1906).
 80. Naegeli, C. & Tyabji, A. Über den Umsatz aromatischer Isocyansäure-ester mit organischen Säuren. I. Theorie und Anwendung der Reaktion für die präparative Darstellung von Säure-anhydriden. *Helv. Chim. Acta* **17**, 931–957 (1934).
 81. Ghatge, N. & Dandge, D. Polyimide copolymers by condensation of one dianhydride and two diisocyanates. *Die Angew. makromolekulare Chemie* **66**, 66–73 (1978).
 82. Carleton, P. S., Farrissey, W. J. & Rose, J. S. The formation of polyimides from anhydrides and isocyanates. *J. Appl. Polym. Sci.* **16**, 2983–2989 (1972).
 83. Sintès-Zydowicz, N., Pham, Q. T. & Michaud, P. Low-molecular-weight poly(imide-amide)s obtained by copolycondensation of 4,4'-methylenedi(phenyl isocyanate), trimellitic acid anhydride and benzoic acid in N-methyl-2-pyrrolidone, 1. The microstructure studied by ¹H and ¹³C NMR. *Die Makromol. Chemie* **194**, 2295–2307 (1993).
 84. Anton, A., Lienert, K.-W. & Hegemann, G. Wire Enamels – An Application for High Performance Polymers Unknown to Chemists. *Macromol. Mater. Eng.* **293**, 331–339 (2008).

-
85. Felberg, J., Han, J. & Yokelson, H. Amide-imide resin having phthalic anhydride moieties. *US Pat. 5,187,254* (1993).
86. Campa, J. de la. Aliphatic-aromatic polyamide-imides from diisocyanates, 2. Study of the influence of the reaction conditions on polymer structure. *Die Makromol. Chemie* **578**, 571–578 (1982).
87. Nieto, J. Aliphatic-aromatic polyamide-imides from diisocyanates, 1. ¹H and ¹³C NMR study of polymer structure. *Die Makromol. Chemie* **569**, 557–569 (1982).
88. Sintès-Zydowicz, N. Low-molecular-weight poly (imide-amide) s obtained by copolycondensation of 4, 4' methylenedi (phenyl isocyanate), trimellitic acid anhydride and benzoic acid in. *Die Makromol. Chemie* **2307**, 2295–2307 (1993).
89. Grieco, P. A., Clark, D. S. & Withers, G. P. Direct conversion of carboxylic acids into amides. *J. Org. Chem.* **44**, 2945–2947 (1979).
90. Wadhwa, C. L. *High voltage engineering*. (New Age International, 2007).
91. <http://capturedlightning.com/>. Figure of Lichtenberg Figure. (2015).
92. Lewis, T. J. Nanometric dielectrics. *IEEE Trans. Dielectr. Electr. Insul.* **1**, 812–825 (1994).
93. Nelson, J. K., Fothergill, J. C., Dissado, L. A. & Peasgood, W. Towards an understanding of nanometric dielectrics. *Annu. Rep. Conf. Electr. Insul. Dielectr. Phenom.* 295–298 (2002).
94. Imai, T., Hirano, Y., Hirai, H., Kojima, S. & Shimizu, T. Preparation and properties of epoxy-organically modified layered silicate nanocomposites. in *Conference Record of the the 2002 IEEE International Symposium on Electrical Insulation (Cat. No.02CH37316)* 379–383 (2002).
95. Tanaka, T., Montanari, G. C. & Mülhaupt, R. Polymer nanocomposites as dielectrics and electrical insulation- perspectives for processing technologies, material characterization and future applications. in *IEEE Transactions on Dielectrics and Electrical Insulation* **11**, 763–784 (2004).
96. Smith, R., Liang, C., Landry, M., Nelson, J. & Schadler, L. The mechanisms leading to the useful electrical properties of polymer nanodielectrics. *IEEE Trans. Dielectr. Electr. Insul.* **15**, 187–196 (2008).
97. Roy, M. *et al.* Polymer nanocomposite dielectrics - the role of the interface. *IEEE Trans. Dielectr. Electr. Insul.* **12**, 629–643 (2005).
98. Nelson, J. K. & Hu, Y. Nanocomposite dielectrics—properties and implications. *J. Phys. D. Appl. Phys.* **38**, 213–222 (2005).

99. Nelson, J. K. The Promise of Dielectric Nanocomposites. in *Conference Record of the 2006 IEEE International Symposium on Electrical Insulation* 452–457 (IEEE, 2006).
100. Fothergill, J. C., Nelson, J. K. & Fu, M. Dielectric properties of epoxy nanocomposites containing TiO₂, Al₂O₃ and ZnO fillers. in *The 17th Annual Meeting of the IEEE Lasers and Electro-Optics Society, 2004. LEOS 2004*. 406–409 (IEEE, 2004).
101. Nelson, J. K. & Fothergill, J. C. Internal charge behaviour of nanocomposites. *Nanotechnology* **15**, 586–595 (2004).
102. Roy, M., Nelson, J. K., MacCrone, R. K. & Schadler, L. S. Candidate mechanisms controlling the electrical characteristics of silica/XLPE nanodielectrics. *J. Mater. Sci.* **42**, 3789–3799 (2007).
103. Li, J., Zhang, L. & Ducharme, S. Electric energy density of dielectric nanocomposites. *Appl. Phys. Lett.* **90**, 132901 (2007).
104. Kozako, M. *et al.* Surface change of polyamide nanocomposite caused by partial discharges. in *2003 Annual Report Conference on Electrical Insulation and Dielectric Phenomena* 75–78 (2003).
105. Kozako, M., Fuse, N., Ohki, Y., Okamoto, T. & Tanaka, T. Surface degradation of polyamide nanocomposites caused by partial discharges using IEC (b) electrodes. *IEEE Trans. Dielectr. Electr. Insul.* **11**, 833–839 (2004).
106. Kozako, M. *et al.* Difference in surface degradation due to partial discharges between polyamide nanocomposite and microcomposite [electrical insulation applications]. in *The 17th Annual Meeting of the IEEE Lasers and Electro-Optics Society, 2004. LEOS 2004*. 398–401 (2004).
107. Kozako, M. *et al.* Surface roughness change of epoxy/TiO₂ nanocomposites due to partial discharges. *Proc. 2005 Int. Symp. Electr. Insul. Mater. 2005. (ISEIM 2005)*. **3**, 661–664 (2005).
108. Bamji, S. Dielectric properties of polypropylene containing nano-particles. in *Annual Report Conference on Electrical Insulation and Dielectric Phenomena* 166–170 (2005).
109. Nelson, J. K. Overview of nanodielectrics: Insulating materials of the future. in *2007 Electrical Insulation Conference and Electrical Manufacturing Expo, EEIC 2007* 229–235 (2007).
110. Tanaka, T., Kozako, M., Fuse, N. & Ohki, Y. Proposal of a multi-core model for polymer nanocomposite dielectrics. *IEEE Trans. Dielectr. Electr. Insul.* **12**, 669–681 (2005).

-
111. Tanaka, T. Interpretation of Several Key Phenomena Peculiar to Nano Dielectrics in terms of a Multi-core Model. in *2006 IEEE Conference on Electrical Insulation and Dielectric Phenomena* 298–301 (IEEE, 2006).
 112. Plueddemann, E. P. Adhesion Through Silane Coupling Agents. *J. Adhes.* **2**, 184–201 (1970).
 113. Plueddemann, E. *Silane coupling agents*. (Plenum Press, 1982).
 114. Weaver, K., Stoffer, J. & Day, D. Interfacial bonding and optical transmission for transparent fiberglass/poly (methyl methacrylate) composites. *Polym. Compos.* **16**, 161–169 (1995).
 115. Ishida, H. & Koenig, J. L. Fourier transform infrared spectroscopic study of the silane coupling agent/porous silica interface. *J. Colloid Interface Sci.* **64**, 555–564 (1978).
 116. Culler, S., Ishida, H. & Koenig, J. Structure of silane coupling agents adsorbed on silicon powder. *J. Colloid Interface Sci.* **106**, 334–346 (1985).
 117. Rodriguez, M. A., Liso, M. J., Rubio, F., Rubio, J. & Oteo, J. L. Study of the reaction of γ -methacryloxypropyltrimethoxysilane (γ -MPS) with slate surfaces. *J. Mater. Sci.* **34**, 3867–3873 (1999).
 118. Sathyanarayana, M. & Yaseen, M. Role of promoters in improving adhesions of organic coatings to a substrate. *Prog. Org. Coatings* **26**, 275–313 (1995).
 119. Ishida, H. & Koenig, J. Vibrational Assignments of Organosilanetriols. I. Vinylsilanetriol and Vinylsilanetriol-d 3 in Aqueous Solutions. *Appl. Spectrosc.* **32**, 462–469 (1978).
 120. Nishiyama, N., Horie, K. & Asakura, T. Adsorption behavior of a silane coupling agent onto a colloidal silica surface studied by ^{29}Si NMR spectroscopy. *J. Colloid Interface Sci.* **129**, 113–119 (1989).
 121. Daniels, M. & Francis, L. Silane Adsorption Behavior, Microstructure, and Properties of Glycidoxypentyltrimethoxysilane-Modified Colloidal Silica Coatings. *J. Colloid Interface Sci.* **205**, 191–200 (1998).
 122. Vrancken, K. C., De Coster, L., Van Der Voort, P., Grobet, P. J. & Vansant, E. F. The Role of Silanols in the Modification of Silica Gel with Aminosilanes. *J. Colloid Interface Sci.* **170**, 71–77 (1995).
 123. Kang, H.-J., Meesiri, W. & Blum, F. D. Nuclear magnetic resonance studies of the hydrolysis and molecular motion of aminopropylsilane. *Mater. Sci. Eng. A* **126**, 265–270 (1990).
 124. Crandall, J. K. & Morel-Fourrier, C. Siloxanes from the hydrolysis of isopropyltrimethoxysilane. *J. Organomet. Chem.* **489**, 5–13 (1995).

125. Beari, F. *et al.* Organofunctional alkoxysilanes in dilute aqueous solution: New accounts on the dynamic structural mutability. *J. Organomet. Chem.* **625**, 208–216 (2001).
126. Blum, F. & Meesiri, W. Hydrolysis, adsorption, and dynamics of silane coupling agents on silica surfaces. *J. Adhes. Sci. Technol.* **5**, 479–496 (1991).
127. Osterholtz, F. D. & Pohl, E. R. Kinetics of the hydrolysis and condensation of organofunctional alkoxysilanes: a review. *J. Adhes. Sci. Technol.* **6**, 127–149 (1992).
128. Daniels, M., Sefcik, J., Francis, L. & McCormick, A. Reactions of a Trifunctional Silane Coupling Agent in the Presence of Colloidal Silica Sols in Polar Media. *J. Colloid Interface Sci.* **219**, 351–356 (1999).
129. Ho, K. & Chen, L. Kinetic studies of polyamide-imide synthesis. *J. Polym. Sci. Part A Polym. Chem.* **35**, 1703–1710 (1997).
130. Aranda, P. & Ruiz-Hitzky, E. Poly(ethylene oxide)-silicate intercalation materials. *Chem. Mater.* **4**, 1395–1403 (1992).
131. Ranade, A., D'Souza, N. & Gnade, B. Exfoliated and intercalated polyamide-imide nanocomposites with montmorillonite. *Polymer (Guildf)*. **43**, 3759–3766 (2002).
132. Jr, Z. W., Jones, F., Pappas, S. & Wicks, D. *Organic coatings: science and technology*. (John Wiley & Sons, 2007).
133. Chen, L. W. & Ho, K. S. Synthesis of polyamide-imide by blocked-methylene diisocyanates. *J. Polym. Sci. Part A Polym. Chem.* **35**, 1711–1717 (1997).
134. Glaser, R. & Wilkes, G. Structure property behavior of polydimethylsiloxane and poly (tetramethylene oxide) modified TEOS based sol-gel materials. *Polym. Bull.* **19**, 51–57 (1988).
135. Letoffe, J.-M., Putaux, J.-L., David, L. & Bourgeat-Lami, E. Aqueous Dispersions of Silane-Functionalized Laponite Clay Platelets. A First Step toward the Elaboration of Water-Based Polymer/Clay Nanocomposites. *Langmuir* **20**, 1564–1571 (2004).
136. Brochier Salon, M. C., Bayle, P. A., Abdelmouleh, M., Boufi, S. & Belgacem, M. N. Kinetics of hydrolysis and self condensation reactions of silanes by NMR spectroscopy. *Colloids Surfaces A Physicochem. Eng. Asp.* **312**, 83–91 (2008).
137. Salon, M.-C. B., Abdelmouleh, M., Boufi, S., Belgacem, M. N. & Gandini, A. Silane adsorption onto cellulose fibers: hydrolysis and condensation reactions. *J. Colloid Interface Sci.* **289**, 249–61 (2005).

-
138. Shen, W., He, H. P., Zhu, J., Yuan, P. & Frost, R. L. Grafting of montmorillonite with different functional silanes via two different reaction systems. *J. Colloid Interface Sci.* **313**, 268–273 (2007).
 139. Park, K. & Kwon, O. Interlamellar Silylation of Montmorillonite with 3-Aminopropyltriethoxysilane. *Bull. Korean Chem. Soc.* **25**, 965–968 (2004).
 140. Powell, C. E., Duthie, X. J., Kentish, S. E., Qiao, G. G. & Stevens, G. W. Reversible diamine cross-linking of polyimide membranes. *J. Memb. Sci.* **291**, 199–209 (2007).
 141. Xie, Z. *et al.* Synthesis and characterization of hybrid organic–inorganic materials based on sulphonated polyamideimide and silica. *J. Polym. Res.* **18**, 965–973 (2010).
 142. Mandair, A.-P. S., Michael, P. J. & McWhinnie, W. R. ²⁹Si MASNMR investigations of the thermochemistry of laponite and hectorite. *Polyhedron* **9**, 517–525 (1990).
 143. Briesenick, D. 3D-Nanotomographie zur Untersuchung orientierter Schichtsilikat-Polyamidimid-Nanokomposite. (Universität Paderborn, 2011).
 144. Park, J., Kwon, S. & Lee, J. Effect of Organically Modified Layered Silicate on Thermal , Mechanical , and Electrical Properties of Epoxy- Based Nanocomposites. *Bull. Korean Chem. Soc.* **12**, 135–139 (2011).
 145. Park, J. Long-term AC Electrical Treeing Behaviors of Epoxy / Layered Silicate Nanocomposites Prepared by a 3-Roll Mill. *Bull. Korean Chem. Soc.* **13**, 85–88 (2012).
 146. Takala, M. Electrical Insulation Materials towards Nanodielectrics. (Tampere University of Technology, 2010).
 147. Imai, T. *et al.* Effects of nano- and micro-filler mixture on electrical insulation properties of epoxy based composites. *IEEE Trans. Dielectr. Electr. Insul.* **13**, 319–326 (2006).